Chem Soc Rev

REVIEW ARTICLE

Published on 29 November 2021
Licence and permissions

Check for updates

Cite this: *Chem. Soc. Rev.*, 2021, **50**, 13692

Developing sustainable, high-performance perovskites in photocatalysis: design strategies and applications†

Haoxin Mai,[a] Dehong Chen, *[a] Yasuhiro Tachibana, [b] Hajime Suzuki, [c] Ryu Abe [c] and Rachel A. Caruso *[a]

Solar energy is attractive because it is free, renewable, abundant and sustainable. Photocatalysis is one of the feasible routes to utilize solar energy for the degradation of pollutants and the production of fuel. Perovskites and their derivatives have received substantial attention in both photocatalytic wastewater treatment and energy production because of their highly tailorable structural and physicochemical properties. This review illustrates the basic principles of photocatalytic reactions and the application of these principles to the design of robust and sustainable perovskite photocatalysts. It details the structures of the perovskites and the physics and chemistry behind photocatalytic reactions and describes the advantages and limitations of popular strategies for the design of photoactive perovskites. This is followed by examples of how these strategies are applied to enhance the photocatalytic efficiency of oxide, halide and oxyhalide perovskites, with a focus on materials with potential for practical application, that is, not containing scarce or toxic elements. It is expected that this overview of the development of photocatalysts and deeper understanding of photocatalytic principles will accelerate the exploitation of efficient perovskite photocatalysts and bring about effective solutions to the energy and environmental crisis.

Received 31st August 2021

DOI: 10.1039/d1cs00684c

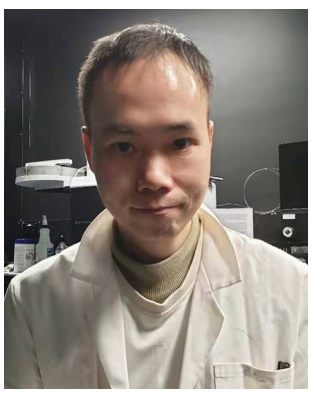
rsc.li/chem-soc-rev

[a] *Applied Chemistry and Environmental Science, School of Science, STEM College, RMIT University, GPO Box 2476, Melbourne, Victoria 3001, Australia. E-mail: dehong.chen@rmit.edu.au, rachel.caruso@rmit.edu.au*

[b] *School of Engineering, STEM College, RMIT University, Bundoora, Victoria 3083, Australia*

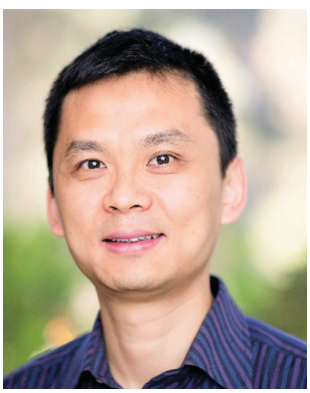
[c] *Department of Energy and Hydrocarbon Chemistry, Graduate School of Engineering, Kyoto University, Katsura, Nishikyo-ku, Kyoto 615-8510, Japan*

† Electronic supplementary information (ESI) available: Notes on principles of photocatalytic water splitting and pollutant degradation, tables summarizing titanate, ferrite, niobate and other oxide perovskite and halide perovskite photocatalyst properties (CB, VB, bandgap and H_2/O_2 evolution rates or pollutant investigated). See DOI: 10.1039/d1cs00684c



Haoxin Mai

Haoxin Mai received his MSc degree in Information Technology and Computer Science from the University of Technology Sydney, and PhD degree in Materials Chemistry from the Research School of Chemistry at the Australian National University in 2019. He has worked at the Royal Melbourne Institute of Technology (RMIT) University as a research assistant from 2019. His research interests include perovskite photocatalysis and photoluminescence, ferroelectric thin films, controllable synthesis of inorganic colloid nanocrystals and machine learning.



Dehong Chen

Dehong Chen is a research fellow in the Applied Chemistry & Environmental Science discipline at RMIT University, Australia. He received his PhD degree in chemistry from Fudan University in 2006. Before joining RMIT University, he conducted research work at the University of Melbourne and the Australian National University. He currently has interests in design and synthesis of diverse functional materials for a range of applications including clean energy utilization, energy storage, environmental remediation and sensors.

This journal is © The Royal Society of Chemistry 2021

1. Introduction

Our ever increasing need for energy and its associated environmental pollution are two pressing problems we face with an increasing population and industrialization in the 21st century.[1] It is estimated that by the end of this century, the worldwide energy demand is going to exhaust the non-renewable energy sources (coal, oil and gas) on which we rely heavily.[1–3] In addition, the greenhouse gases produced by burning these traditional energy sources, as well as the SO_x and NO_x produced from the impurities in the fossil fuels, are significant contributors to the current environmental problems.[4,5] Therefore, considerable research is being conducted to determine renewable energy sources to circumvent an energy crisis, while maintaining an inhabitable planet. Among the alternative energy sources, solar energy is most attractive because the sun provides free, renewable, abundant and sustainable energy.[1–3,5–7] Since the energy from sunlight that reaches the earth's surface is 10 000 times more than what we currently consume, it is expected that solar energy could satisfy a large portion of the requirements for worldwide energy consumption in the future.[8] One feasible way to utilize solar energy is to convert it into chemical energy. Taking advantage of photocatalysis, where light is used to instigate or improve chemical reactions, hydrogen can be extracted from water as a clean fuel, or CO_2 can be reduced to generate chemical fuel.[1,5,7,9–15] In addition to producing fuel from sunlight, photocatalytic reactions can be used in water purification for pollutant degradation, bacteria destruction and heavy-metal ion reduction.[12,16] Thus this approach can be used to assist where there is a shortage of clean water or in areas where water pollution due to industry spread, population growth and long-term droughts is an issue. Photocatalysis is also a promising alternative to promote green organic synthesis.[17,18] Therefore, it is important to continue to develop photocatalysts working towards high efficiency, stability and low cost for a sustainable future.



Yasuhiro Tachibana

Yasuhiro Tachibana is a Professor at RMIT University. He received his BEng and MEng from Osaka University in 1992 and 1995, and his PhD in chemistry at Imperial College London in 2000. His research interests include developing photoactive nanomaterials and solar energy conversion devices such as dye or semiconductor quantum dot sensitized solar cells, perovskite solar cells and photocatalysis for water splitting and CO_2 reduction by employing time-resolved laser spectroscopies.



Hajime Suzuki

Hajime Suzuki received his BS (2013), MS (2015), and PhD (2018) degrees from Kyoto University. He then worked as a postdoctoral fellow (2018–2019) at Osaka University. He is currently an assistant professor at Kyoto University. His current research focuses on the development of novel photocatalysts and cocatalysts for water splitting.



Ryu Abe

Ryu Abe received his BS (1996), MS (1998) and PhD (2001) degrees from Tokyo Institute of Technology. He then worked as a postdoctoral fellow (2001–2002) and as a researcher (2002–2005) at the National Institute of Advanced Industrial Science and Technology (AIST), Japan. In 2005, his academic career as an associate professor began at the Catalysis Research Center, Hokkaido University. He was then promoted to a Professor at Graduate School of Engineering, Kyoto University, in 2012. His research mainly focuses on the development of new visible-light-responsive photocatalysts and reaction systems for water splitting.



Rachel A. Caruso

Rachel Caruso is a materials chemist and has expertise in advanced porous materials. She has led teams of scientists at the Max Planck Institute of Colloids and Interfaces, The University of Melbourne, the Commonwealth Scientific and Industrial Research Organisation and RMIT University. Her research interests include materials such as porous oxides, perovskites and carbon materials for energy and environmental applications. She is currently the Director of the Advanced Materials Enabling Capability Platform at RMIT University.

Pioneering work on photocatalysts was carried out in the 1930s: Baur and Rebmann used UV light to demonstrate photo assisted water splitting for AgCl/TlCl in water, but the field did not progress until the discovery of the photocatalytic properties of TiO_2 in 1972.[19] Many efforts have been devoted to modulating the bandgap and the structure of the TiO_2-based photocatalysts to improve their photoactivity for water splitting and pollutant degradation.[16,20,21] Besides, since photocatalysts comprising abundant elements and exhibiting good catalytic performance are expected to be cheaper and more suitable for application, a range of efficient photocatalytic materials have been discovered, such as Ta_3N_5,[22,23] $Y_2Ti_2O_5S_2$,[24] $BiVO_4$,[25] $AgPO_4$,[26] Ag/AgCl,[27] quantum dots,[28] and metal-free catalysts including carbon nitride,[11,29,30] boron carbide,[31] P-doped graphene,[32] phosphorus[33] and organic polymer.[34–36] To further enhance the photocatalytic efficiency and to enable practical application, heterostructures have been used to adjust the redox ability of the catalysts and modify the path of charge transport,[37–39] while Z-scheme systems can spatially separate the generated H_2 and O_2 in the water splitting reaction.[40,41] Despite many photocatalysts being developed and studied, most are still far from industrial application due to their low conversion efficiency.[42] Considering the ever increasing need for clean energy and environmental remediation, effective photocatalysts that possess well-aligned band structure for the reaction of interest, large surface area, high crystallinity and can be produced and applied large-scale, are still highly sought after.

Perovskites and their derivatives have received substantial attention as photocatalytic materials for both wastewater treatment and water electrolysis because of their highly tailorable structural and physicochemical properties.[5,9,43] Perovskite refers to the family of materials having the same type of structure as $CaTiO_3$. It has a cubic structure with a general chemical formula ABX_3, in which A and B are two cations with different sizes (A is usually larger than B) and X is an anion connecting cations A and B. Owing to the flexibility of this crystal structure, most of the metal elements in the periodic table can reside at the A or B sites, resulting in a large number of perovskite materials. In addition to the cubic structure, some perovskites exhibit distorted structures that relate to the ratio of the radii of cation A and B, such as orthorhombic, tetragonal, hexagonal and monoclinic perovskites.[43] Such structural distortion can induce variation in the physical, electrical and photocatalytic properties, by which the photocatalytic activities can be tuned by ion substitution. Moreover, introducing metal ions with appropriate radius and valence in A and B sites generates perovskite derivatives such as double perovskites,[43] and layered perovskites form when the ABX_3 units repeat infinitely in-plane producing perovskite slabs, but extension of the ABX_3 units in the third dimension is interrupted by metal ion or metal oxide layers.[9] These layered perovskites (comprised of alternate layers of 2D perovskite slabs and metal ions or metal oxides) have anisotropic charge transfer properties and spatially separated valence band (VB) and conduction band (CB), both of which significantly impact on their photocatalytic performance. Because of this structure, the optical, electrical and catalytic properties of these perovskite derivatives can be significantly varied by ion substitution or intercalation of functional compounds. To date, hundreds of perovskite-based photocatalysts have been reported with some achieving high photocatalytic efficiency.[44] Therefore, perovskite-based photocatalytic materials show promise for practical use.

In this review, an overview of the recent progress (from 2017 to 2021) in perovskites for application in photocatalytic reactions, such as water splitting and water degradation, is provided. There are some excellent reviews regarding perovskite photocatalysts,[5,9,45–47] however few of them distinguish the earth-abundant nontoxic perovskites from the perovskites containing rare or toxic elements that would be difficult to scale up and apply.[48] Aiming at providing a practical guideline for the construction of low cost, sustainable and high efficiency photocatalysts, this review will not discuss perovskites consisting of the rarest elements (Fig. 1),[49] toxic elements (such as Pb, Cd and Hg), or the elements of which the annual production is less than 5000 tons.[50] A comprehensive description and comparison of the strategies for constructing perovskite-based photocatalysts and development of the synthesis, application and mechanism of these photocatalysts, including oxide, halide and oxyhalide, in recent years are still lacking. Given the substantial literature contributions in the last few years, it is important to review the progress in this quickly developing area. Therefore, the goal of this review is to summarize recent progress (last five years) on the earth-abundant, nontoxic, perovskite-based photocatalysts. This will provide the reader with a strong understanding of the design strategies by discussing their advantages, limitations and applications, and give a perspective for future investigation of earth abundant, nontoxic perovskite materials for photocatalytic energy conversion and environmental clean-up. This review consists of five sections. This section has briefly introduced photocatalysis and perovskites.

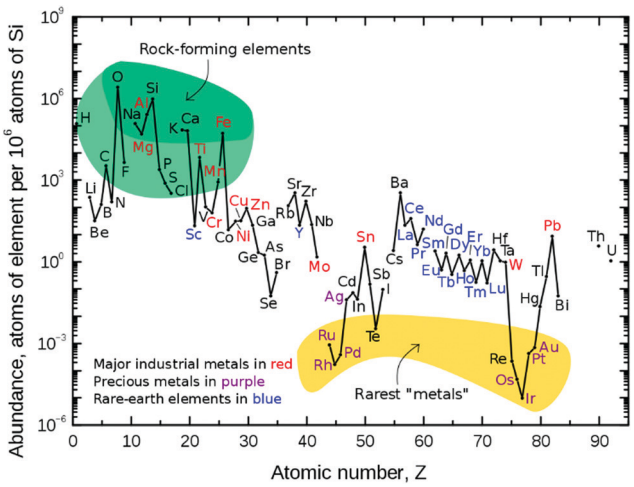


Fig. 1 Abundance of the elements on earth given in atom fraction as a function of the atomic number. The rare earth elements are indicated in blue. Reproduced with permission.[49] Copyright 2005, U.S. Geological Survey.

 This journal is © The Royal Society of Chemistry 2021

In the next section, the structure of perovskites and their derivatives are classified and described. In addition to reviewing the well-known theories, new theories proposed through data-driven method are described. Section 3 gives a brief introduction to the principles of the photocatalytic reactions and elaborates on current strategies for enhancing the photocatalytic activities and stability of the perovskite materials. In Section 4, progress in the field of photocatalysis is exemplified by a variety of earth-abundant, nontoxic perovskite oxides, halides and oxyhalides, in which the effects of varied strategies on photoactivity are emphasized. Here the focus will be on how the design of the perovskite structure can alter the band structure and charge transfer properties and illustrate the relationship between photoactivity and the structure and components of the photocatalysts. It is worth mentioning that studies involving the utilization of dopants or co-catalysts that contain toxic or rare elements may be cited as demonstrations of certain design strategies, but we will suggest environmentally friendly substitutes, if possible, to ensure the sustainability and the commercial feasibility of the materials. In the last section, summaries are given and perspectives for current challenges and future developments in the design of perovskite photocatalysts composed of earth-abundant, nontoxic elements are proposed.

2. Structure of perovskites

2.1. Crystal structure and tolerance factor

In the typical perovskite structure, the B cation is 6-fold coordinated and the A cation is 12-fold cuboctahedral coordinated with the X anions.[43] Large ions, normally alkali, alkaline earth, rare earth ions or organic cations, situate at the A-site, while small ions, such as transition metal ions, would be found at the B-site.

To estimate the stability of a perovskite structure, a tolerance factor (t) is introduced:[51]

$$t = (r_A + r_B)\Big/\sqrt{2}(r_B + r_X) \quad (1)$$

where r_A, r_B and r_X are the ionic radii of the A cation, B cation and X anion, respectively. In most of the cases, t is not equal to 1, resulting in structure distortion and accordingly, orthorhombic or rhombohedral structures may form.[43] Generally, it is believed that perovskite will be stable when $0.75 < t < 1$, but there are also reports revealing that perovskite structures may not be stable even when t is in the range of 0.8–0.9.[52] It therefore indicates that the stability of the perovskite structure cannot be predicted based on one index. The octahedral factor (μ), has been used to estimate the perovskite stability as well:[53]

$$\mu = r_B/r_X \quad (2)$$

The ability to form perovskites from different cations and anions can therefore be determined from the t–μ mapping, where the perovskite would be stabilized for a t-value ranging between 0.813 and 1.107, and the μ-value ranging from 0.442 and 0.895.[53,54]

Since the tolerance factor and the octahedral factor are geometrical descriptors but ignore the contributions of the other chemical properties, such as the coordinating numbers of the constituent ions, a perovskite in which the interatomic distances fulfil both the t and μ-values may not be chemically stable. New structural factors with higher accuracy have been developed by material informatics approaches. Based on a dataset of 185 experimentally labelled ABX_3 compounds, Pilanlia *et al.* constructed a machine learning model to classify the perovskites from non-perovskites, but this model could not provide a new structural factor to assess the stability of perovskites.[55] Lu *et al.* used a gradient boosting classification algorithm to analyse 132 features of 1109 compounds and summarized a revised tolerance factor workable for mixed X-site perovskites.[56] Bartel *et al.* disclosed a new tolerance factor, τ, which incorporates both the geometric factors and chemical nature, through a data-driven approach:[57]

$$\tau = r_X/r_B - n_A\left(n_A - \frac{r_A/r_B}{\ln(r_A/r_B)}\right) \quad (3)$$

where n_A is the oxidation state of A, r_A must be larger than r_B by definition and $\tau < 4.18$ indicates a stable perovskite structure. This data-driven descriptor showed much better performance in the prediction of the stability of the single and double perovskites compared with the t–μ mapping. More importantly, due to the low complexity of this one-dimension tolerance factor, thousands of undiscovered perovskites were selected out from the arbitrary combination of the A, B and X elements, and their stabilities were confirmed by the density functional theory (DFT) calculation.[57] Due to the highly predictive accuracy and fast speed of screening, the material informatic methods have become important strategies for the discovery of new perovskite photocatalysts.[55,57,58]

2.2. Cation and anion defects in perovskites

Considering the constraints of the tolerance factors, a wide range of elements can be placed into the ABX_3 perovskite structure. Other than distorting the cubic structure, both cation and anion defects would be generated under ion substitution to ensure the electroneutrality of the compounds. Also, intrinsic defects will form under cation-poor or cation-rich conditions.[43]

Regarding the cation defects, the formation of A-site vacancies is frequent as the large A cation distributed in the stable BX_6 array can be partially removed. When the A-site cation is substituted by cations (noted as A′) with higher valence, the A-site vacancies will form as acceptors, giving compounds with a stoichiometry of $A_{1-x-\delta}A'_xBX_3$.[59] Alternatively, when the A-site cation is replaced with the lower valence cations, X vacancies (donor) will be introduced giving compounds of stoichiometry of $A_{1-x}A'_xBX_{3-\delta}$. Besides ion substitution, A-site vacancies can also form in B-rich perovskites.[60] In contrast to the A-site vacancies, B-site vacancies in perovskites are not thermodynamically favoured in most cases. This is because the B-site cations are of small size and large charge, and the

corner-shared BX_6 octahedra form a firm network. Instead of B-site vacancies, B-site substitution tends to induce X vacancies or interstitials.[9,43]

The anion defects in perovskites are generated to fulfil the charge balance in the ion substitution. A general formula $A_nB_nX_{3n-1}$ is used to describe the X-deficient perovskite, in which the stacking manner is dependent on the intrinsic properties of the perovskite such as size, electronic configurations and coordination numbers of A and B cations. In addition to compensating for the excess charges present due to the cation substitution, anion defects are also generated from anion substitution.[61] Note that both the cation and anion defects may change the crystal structures and band structures of perovskites, and thus have significant effects on their photocatalytic activities. Moreover, such defects can induce a defect-dipole, which can then give rise to local electric fields, promoting carrier transport and charge separation, and accordingly affect photoactivities.[62]

Intrinsic defects derived from the cation-poor or cation-rich conditions have significant effects on their photoelectronic properties. For example, in $CsSnI_3$ the intrinsic acceptor defects (Sn and Cs vacancies) forming under Sn-poor conditions will become electron–hole recombination centres, while the intrinsic donor defects, Sn(I) forming under Sn-rich conditions, can trap photogenerated electrons, leading to photocatalysis deterioration.[63] In $SrTiO_3$ crystals, Sr vacancies can cause antisite Ti defects and subsequently local dipole moments would form due to small off-centre displacement of the Ti ions.[64] Although normally no special properties stemming from such local dipole moment can be found in the bulk materials because all the intrinsic defect regions are isolated, abnormal electrical properties, such as considerable polarization, are observed when the size of the material is similar to the intrinsic defect regions (a few nanometres).[65] This research therefore strongly inspires the application of ultra-small particles in photocatalysis, as the intrinsic defects may play an important role in the photocatalytic activities.

2.3. Perovskite derivatives

2.3.1 Double perovskites. When the single perovskite structure is modified by two types of B ions with suitable size and charge, double perovskite structures, with the general formula $A_2BB'X_6$, will form.[43] The crystal structure of the double perovskite is determined by the arrangement of the B and B′ ions (Fig. 2).[66,67] A disordered double perovskite forms when the B and B′ ions are randomly distributed in the B sublattice (*e.g.*, Ca_2FeMoO_6,[68] Fig. 2a). In most of the cases, an ordered rock salt structure is adopted, where the unit cell can be viewed as an alternating arrangement of the BX_6 and $B'X_6$ octahedra in all three dimensions (*e.g.*, $Cs_2AgBiBr_6$,[69] Fig. 2b). Two other ordered double perovskite structures are also observed: when the BX_6 and $B'X_6$ octahedra only alternate in one direction producing double perovskites with layered order (*e.g.*, La_2CuSnO_6,[70] Fig. 2c), and in rare cases where the A-sites are occupied by different ions, columnar order may take place, in which the BX_6 and $B'X_6$ octahedra alternate in two directions

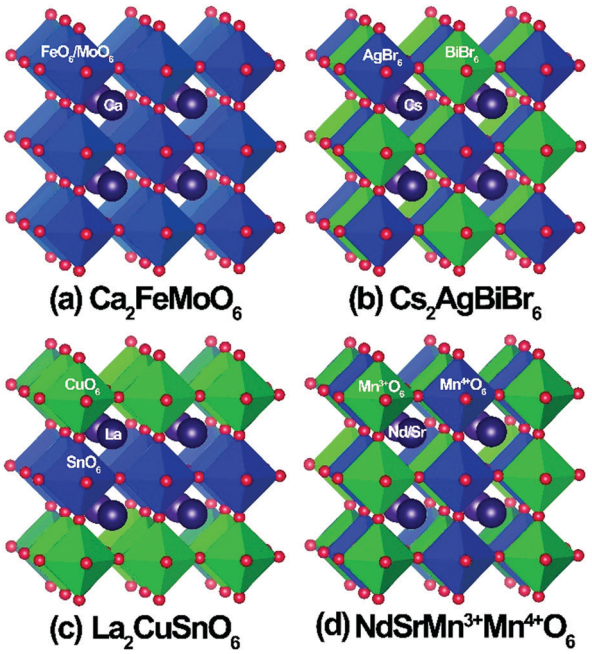


Fig. 2 Crystal structures of examples of $A_2BB'X_6$ perovskites with different B-site cation orderings: (a) random, (b) rock-salt, (c) layered and (d) columnar order. The purple spheres represent A-site element, the red spheres represent X-site element, and the green and blue octahedra represent BX_6 and $B'X_6$ octahedra respectively in (b), (c) and (d).

(*e.g.*, $NdSrMn^{3+}Mn^{4+}O_6$, Fig. 2d).[67] In these ordered structures, the X anions will move slightly toward the more charged cation to avoid the electronic instabilities when the charge of B and B′ is different.[43]

The formation of double perovskites can bring advantages for the design of photocatalysts. First, a greater selection of elements can be lodged into double perovskites.[71] Second, the intricate structures of double perovskites allow the existence of some unusual electronic structures. For example, the alternate octahedral of BX_6 and $B'X_6$ may lead to two symmetries for A-site cations and variation of the bandgap and band energy.[72] Third, in photocatalytic reactions, which are frequently carried out under a highly reducing/oxidizing atmosphere or strong acidic/basic solutions, the stability of double perovskites is higher than the single perovskites.[69,73] Moreover, perovskite properties, such as band alignment, electronic transfer and polarization, are mainly governed by the B-site cations, and thus a plethora of interesting and useful materials can be designed by manipulation of cation order, structure distortion and changing the combination of different elements in the B-site.[45,74]

To design double perovskites with various cation orders, the entropy and enthalpy in the system must be considered simultaneously. Generally, a random arrangement would be favoured in regard to entropy, but the electrostatic repulsion between the B-site cations may force one B-site cation to be situated away from the other. Currently, it is widely accepted that the difference in the B and B′ cation oxidation states, $\Delta Q = |Q_{B'} - Q_B|$, is the main factor influencing the cation order.[71]

 This journal is © The Royal Society of Chemistry 2021

An ordered arrangement is preferred when $\Delta Q > 2$, while a random arrangement is dominant when $\Delta Q < 1$.[66,67] Apart from ΔQ, the ionic radii difference, Δr, is also a common noted factor affecting the cation order. When the difference in the ionic radii of the B and B′ cations is larger, the probability of the compound exhibiting an ordered arrangement increases, in that the increase of the lattice strain in a random $A_2BB'X_6$ structure surpasses the increase of the entropy.[75] Based on these two factors, double perovskites with appropriate cation order can be designed by selecting suitable elements.

2.3.2 Layered perovskites. Layered perovskites, consisting of two-dimensional (2D) perovskite slabs with alternating cations or cationic structural units, have received tremendous attention due to their photocatalytic activity, ionic conductivity, inductivity, magnetic and optic properties.[9,76,77] According to the layered orientation relative to the principal axis of the cubic perovskite, layered perovskite structures can be classified as {100}, {110} and {111} type. Most of the layered perovskites are of the {100} type, which includes the Aurivillius series (AL), the Ruddlesden–Popper series (RP) and the Dion–Jacobson series (DJ) (Fig. 3).

The general formula of AL perovskites is $\left(A_2'X_2\right)(A_{n-1}B_nX_{3n+1})$ (A′ is Bi^{3+} in most cases), which can be described as the intergrowth of pseudo-perovskite blocks: the $A_{n-1}B_nX_{3n+1}$ slabs and the $A_2'X_2$ layers (Fig. 3a). AL perovskites feature visible light absorption on account of the hybridization between the p orbitals of the X ions and the outermost s orbitals provided by the A′ ions (Bi^{3+}) negatively shifting the VB, and the internal field derived from the distorted structure of perovskite layers that boosts the charge separation.[9]

RP perovskites have interleaving perovskite ABX_3 slabs and rock salt A′X layers (Fig. 3b). The general formula is $A_2'(A_{n-1}B_nX_{3n+1})$. The high performance of the photoelectronic devices based on RP hybrid organic–inorganic perovskites has attracted tremendous attention for their promising application in photovoltaics, photoluminescence and photocatalysis.[78–80]

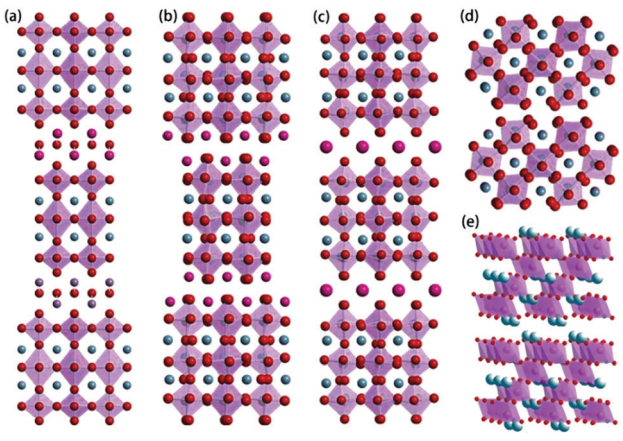


Fig. 3 Crystal structures of layered perovskite compounds (red spheres: X-site element; purple octahedra: BX_6; dark green and pink spheres: A-site element): (a) Aurivillius, (b) Ruddlesden–Popper, (c) Dion–Jacobson, (d) {110} type and (e) {111} type.

Much effort has focused on the materials photoactivity due to the characteristics of anisotropic charge transfer and cation exchange, which can provide more active sites for the reduction half reaction.[81] In addition, the ultrathin 2D nanostructure with large surface area can be readily obtained by an exfoliation process, intercalating bulky cations to form the rock salt layer.[82] Exposure of the A′X terminated surface gives a low barrier for electrocatalytic water dissociation.[82]

DJ perovskites have attracted less attention as photocatalysts. These compounds can be described by the general formula $A'(A_{n-1}B_nX_{3n+1})$. DJ perovskites have a layer of A′ metal ions as the intermediate spacing layer (Fig. 3c), and thus cation exchange and exfoliation occur more readily.[83]

The general composition of the {110} type perovskites is $A_nB_nX_{3n+2}$, and it has an interlayer parallel to the (110) planes of the cubic perovskite structure (Fig. 3d).[84] The general composition of {111} type oxide perovskites is $A_5B_4O_{15}$ or $ALa_4Ti_4O_{15}$, where A is Ca, Sr and Ba while B is Nb or Ta. The structure is considered a cubic perovskite cut parallel to the (111) planes (Fig. 3e).[85] Compared to the oxides, {111} type halide perovskites such as $Cs_4CuSb_2Cl_{12}$, exhibit narrow bandgaps and excellent photoelectronic properties, making them of interest in photocatalytic applications.[86] Moreover, choosing appropriate cations to improve the structural anisotropy is also an effective strategy to increase the photoactivity of these materials.

3. Current strategies for the design of perovskite-based photocatalysts

3.1. Fundamentals of photocatalysis

Photocatalysis uses light to initiate chemical processes, such as water splitting, reduction of CO_2, degradation of pollutants, bacterial disinfection and organic synthesis. Normally, photocatalysis takes place in the presence of a photocatalyst, which absorbs light and generates electron–hole pairs. Due to the many different reactions that can be conducted, there are a wide range of photocatalyst designs and compositions (Fig. 4).

3.1.1 Factors that affect the efficiency of photocatalysts. To design an effective photocatalyst, it is important to understand the fundamentals of photocatalytic processes and identify the critical factors affecting the photocatalyst efficiency (see Notes S1 and S2 in ESI†). In brief, reducing the bandgap of the photocatalysts to absorb more incident light and adjusting the energy levels of the VB and CB to maximize reduction and oxidation ability are two key approaches to enhance the photocatalytic activity. In addition, the bulk and surface charge recombination must be minimized. High crystallinity and low defect concentrations can eliminate the recombination centres, while shortening the charge diffusion distance *via* reducing the particle size is beneficial for less charge recombination. The separation of anode and cathode reactions is another effective strategy to prevent surface recombination, especially in water splitting, but it is not effective in photocatalytic degradation due to the small diffusion coefficient of the superoxide radicals.

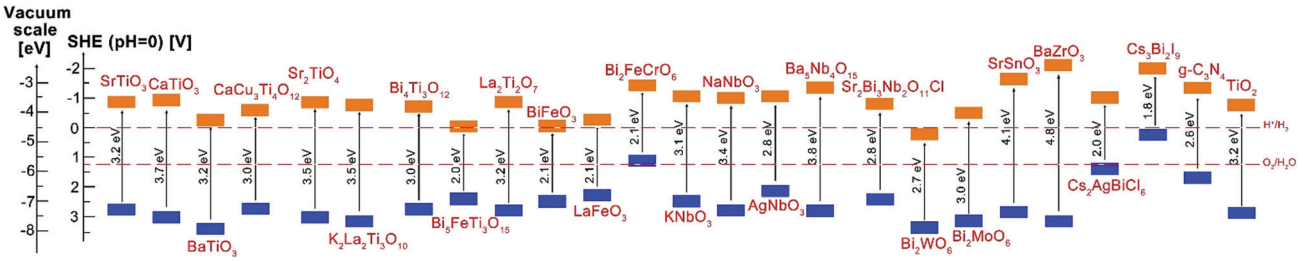


Fig. 4 Absolute and relative (respect to standard hydrogen electrode (SHE), pH = 0) energy levels of valence and conduction bands of some perovskite-based photocatalysts and other representative photocatalysts.

To expose more active sites, large surface area and the prevalence of active facets are required. Scavengers may also be employed to drive the reactions.

3.1.2 Evaluation of photocatalysts. There are three metrics that can be used to evaluate the performance of a photocatalyst: photocatalytic activity, selectivity and stability.

To evaluate the efficiency of a photocatalytic reaction, the amount of product generated within a certain time can be monitored. For example, in photocatalytic water splitting, the H_2 evolution rate and O_2 evolution rate with the unit μmol h^{-1} or μmol h^{-1} $g_{catalyst}{}^{-1}$ are two of the most widely adopted metrics. However, gas evolution rates are also affected by many factors such as light source, wavelength of incident light, shape and volume of the reactor. These factors complicate the comparison of the results among different research groups. Apparent quantum yield (AQY) is thus employed as another important metric to evaluate the efficiency of the photocatalytic reactions. AQY is defined by eqn (4):[87]

$$\mathrm{AQY} = \frac{\text{Number of reacted electrons}}{\text{Number of incident photons}} \times 100\% \quad (4)$$

In water splitting, as the generation of one H_2 molecule and one O_2 molecule requires two and four electrons, respectively, eqn (4) can be rewritten as:

$$\mathrm{AQY} = \frac{2 \times \text{Number of evolved } H_2 \text{ molecules}}{\text{Number of incident photons}} \times 100\% \quad (5)$$

$$\mathrm{AQY} = \frac{4 \times \text{Number of evolved } O_2 \text{ molecules}}{\text{Number of incident photons}} \times 100\% \quad (6)$$

In addition, solar-to-hydrogen conversion efficiency (STH) is useful for H_2 evolution reactions under solar light:[15]

$$\mathrm{STH} = \frac{\text{Output energy of evolved } H_2}{\text{Energy of incident solar light}} \times 100\% \quad (7)$$

Both AQY and STH can be used to compare the results regardless of different photocatalytic reactor setups.

In some cases, multiple photocatalytic reactions occur under similar conditions. For example, photocatalytic CO_2 reduction competes with H_2 evolution, resulting in the formation of CO, CH_4 and H_2. Therefore, selectivity (S) is used to evaluate the ability of a photocatalyst to yield a particular product, and an efficient photocatalyst should have good selectivity to the target product. Assuming there are n competing products generated, the selectivity of a photocatalyst towards the jth product (S_j) is given by eqn (8):[88]

$$S_j = \frac{n_j \times N_j}{\sum_{i=1}^{n} n_i \times N_i} \times 100\% \quad (8)$$

where n_i and n_j are the numbers of electrons involved in forming the ith and the jth products respectively, and N_i and N_j are the evolution rates of the ith and the jth products, respectively.

Besides high photocatalytic activity and selectivity, efficient photocatalysts should have good stability during photocatalytic reactions. To determine the stability of photocatalysts, long-time experiments or repeated experiments are conducted. Although most oxide perovskites exhibit good stability, many halide perovskites are inclined to decompose in the presence of oxygen or moisture and under illumination.[89] Therefore, the development of stable halide perovskites for photocatalytic applications is a major challenge for photocatalysis research.

3.2. Strategies for designing highly active photocatalytic perovskites

The key factors to improve the efficiency of photocatalytic reactions are to suppress the electron–hole recombination and tailor the bandgap to ensure sufficient solar energy is absorbed while retaining the required energy levels for oxidization and reduction of the redox reactions. Numerous strategies have been proposed for the design of efficient perovskite photocatalysts, which will be summarized below.

3.2.1 Band structure engineering. To achieve visible light-driven photocatalytic reactions, the bandgap of the photocatalysts must be <3 eV with the CB energy level being more negative than the potential of the reduction half reaction, and the VB energy level being more positive than the potential of the oxidation half reaction. In the ABX_3 perovskites, the VB consists of the outermost A s + B d + X p hybrid orbitals, and the CB is formed by the unoccupied B d orbitals.[5] Hence, doping of foreign elements into perovskites can alter the band structure in two ways: (1) the formation of new intermediate levels between the CB and VB, and (2) adjusting the position of the CB and VB through hybridizing the orbitals of the dopant and the host elements. Based on the elemental contributions to the CB and VB of perovskites, B-site substitution would be the most effective method to modulate the bandgap energy. When the

 This journal is © The Royal Society of Chemistry 2021

B cation is partially substituted by dopants of lower valence (M), new donor levels at a lower potential than the valence band maximum (VBM) will form due to the generation of the $M_B^{'}$ defects, thereby reducing the apparent bandgap.[90] Other than B-site substitution, A-site doping can also modify the bandgap of perovskites and promote the carrier mobility, in that the difference in size of the A-site ions can induce deformation of the BX_6 octahedra, thus affecting the bandgap and other photoelectronic properties.[91,92] Nevertheless, since X vacancies may form to balance the charge induced by the substitutional defects, more recombination centres will emerge when increasing the dopant amount.[5] Moreover, undesirable ions with high oxidation state may also form during the synthesis, which will then become recombination centres for the photogenerated electrons and holes.[93] To suppress these undesired species, a co-doped ion of higher valence is introduced. The appearance of co-doped ions with high oxidation state contributes to the charge balance and thus prevents the formation of X defects and the change of the valence of doped ions.[94,95] In particular, co-doping of the A-site and B-site is widely applied.[91,96,97] Despite the high activity and stability of the A-site and B-site co-doped photocatalysts, the homogeneity of the dopant and the co-dopant ions is essential for effective charge compensation, and thus preparation methods for the homogeneous co-doped perovskites must be explored carefully.

In addition to the A/B site doping, X-site doping is also considered an effective approach to modulate the band structure of perovskites. As the VB of perovskites is mainly determined by the p orbitals of the X element, substitution of the X anion alters the energy level of the VB.[5] Generally, when the electronegativity of the dopant X′ is higher than that of the X anion, the energy level of the VB increases, promoting the oxidizing power and increasing the bandgap. A negative shift of the VB is observed when the electronegativity of X′ is lower than that of the X anion, which results in a smaller bandgap.[98] Hence anion dopants can be selected to vary the energy levels to suit the requirements of the specific reaction.[9,15] For photocatalytic water splitting and most pollutant degradation reactions, due to the intensive oxidizing power of the oxide perovskites, anions with lower electronegativity, such as halides, N^{3-} and S^{2-}, will be chosen as the dopant ions to reduce the bandgap.[99–103] It should be noted that a reduced bandgap does not guarantee the high photoactivity of the mixed-anion perovskites, because a small bandgap from a negative shift of the VB may correlate to insufficient overpotential for the redox reactions at the surface to occur.

3.2.2 Tuning size and morphology. To improve photocatalytic activity, suppressing electron–hole recombination and concurrently increasing the surface-active sites are key factors for the design of photocatalysts. The size and morphology of the particle are varied by doping foreign elements into the photocatalyst.[5] In perovskites, A-site doping has significant effects on size and morphology.[104,105] The decrease of the particle size influences the photocatalytic activity, in that bulk recombination is decreased when the diffusion distance of the charge to the surface is shortened, and the increased surface area increases active site and reactant contact. It should be pointed out, however, that the benefit of doping has limits as too many foreign ions in the structure may generate more recombination centres, thus decreasing the photocatalytic activity.

The method of preparation affects the perovskite nanostructure.[5] Various methods have been used to synthesise perovskites with controllable morphologies and sizes. The most common methods include solid state reaction, molten salt synthesis, sol–gel chemistry and hydrothermal methods. Among them, the hydrothermal method is promoted to improve the homogeneity and reproducibility of the products and to gain better nanostructure control. A wealth of parameters can be tuned to vary the growth of the nanocrystals. Additives, such as chelating agents or surfactants that can either be adsorbed on the surface of the nuclei or self-assemble, restrict the aggregation of the nuclei, initiate growth into a specific morphology, and facilitate the assembly of various components thereby contributing to the formation of heterostructures.[37,46,106] Hard templates, such as layered titanates, nanospheres, nanofibers and viruses, can manipulate size and morphology of the perovskite.[107–109]

Colloidal synthesis is important for the synthesis of high-quality halide perovskite nanoparticles. This includes two common methods, hot injection and ligand assisted reprecipitation (LARP). Hot injection has been used for halide nanoparticle synthesis for more than ten years.[110,111] This approach is based on rapid injection of one reactant into a hot solution containing the rest of the reactants, ligands and high boiling point solvent, protected by inert gases or nitrogen. In the LARP method, the halide precursor is dissolved into a polar solvent (*e.g.*, dimethylformamide (DMF), dimethylsulfoxide (DMSO)) which is added into a non-polar solvent (*e.g.*, toluene, hexane) in the presence of ligands.[111] Halide nanoparticles with controllable size (with narrow size distribution) and morphology can be obtained by these methods, but the influence of the ligands on the photoactivities of the particles are still unclear.

3.2.3 Type II heterojunction and Z-scheme system. To enhance the photocatalytic performance, two semiconductors can be combined to form heterojunctions, allowing the electron–hole pairs to be separated spatially over the two semiconductors.[112] The heterojunctions of interest, which vary according to the electron–hole transfer mechanism, are the type II and Z-scheme heterojunctions.[40,41,113,114]

A type II heterojunction has the bandgaps of the semiconductors at the junction overlapping but offset, forming a staggered gap. Therefore, the difference in energy between the CBs would drive the photoexcited electrons from one semiconductor to another while the difference in energy between the VBs would force the holes to migrate in the opposite direction (Fig. 5a). Thus, the reduction and oxidation reactions occur at different semiconductors. A suitable band structure of the two semiconductors has both the CB and the VB of semiconductor "A" more negative than semiconductor "B" (*vs.* SHE), and the work function of semiconductor "A" should be larger. The free electrons will move from semiconductor "B" to semiconductor "A" until their Fermi levels are equilibrated, thereby resulting in the downward bending of the CB of

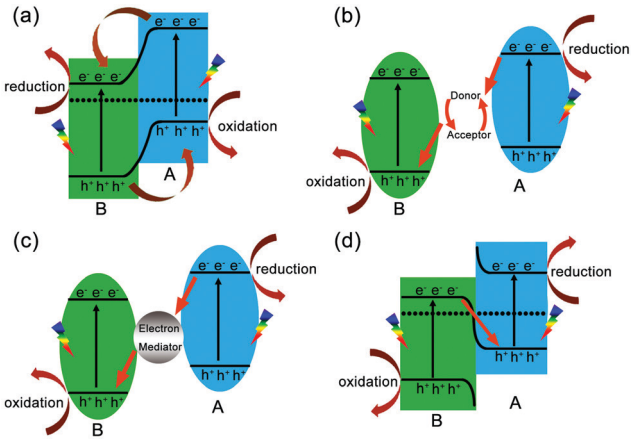


Fig. 5 Schematic of the (a) type-II heterojunction, (b) Z-scheme system with shuttle redox mediators, (c) Z-scheme system with solid state electron mediators and (d) direct Z-scheme system. The dotted lines denote the Fermi level of the components.

semiconductor "A" that can drive the photogenerated electrons from the CB of semiconductor "A" to the CB of semiconductor "B".[113,115] In most cases, narrow bandgap semiconductors with suitable band structure are used to construct type II heterojunction, as they can also serve as the light sensitizer for better light harvesting.[116]

Also important for successful construction of type II heterojunctions is the connection between the two components, which is determined by the effective interfaces.[11] The effective interfaces can be increased through surface modification. Surfaces with opposite charges, or a 2D–2D face contact would lead to the formation of stable heterojunctions.[117–121] Nevertheless, several problems in the type II heterojunction structure obstruct its further application.[40,113,114] The construction of type II heterojunctions reduces the reducing and oxidizing power of the combined semiconductor photocatalysts. Electron migration to a potentially electron-rich component (or holes migration to a hole-rich component) may slow charge movement across the heterojunction due to the electrostatic repulsion. Thus, the efficiency of the photocatalytic reactions may not be maximized in the type II heterojunction system.

The Z-scheme photocatalytic system is promoted to provide stronger redox ability and better charge separation. In a typical Z-scheme system, the photogenerated electrons in semiconductor B, which has higher oxidizing power but more positive CB, recombine with the holes in semiconductor "A", which has higher reducing power but more negative VB (Fig. 5b–d).[40,113,114] Therefore, the photogenerated electrons in semiconductor "A" with higher reducing power, as well as the photogenerated holes in the semiconductor "B" with higher oxidizing power, are preserved. Moreover, the charge migration in the Z-scheme system is physically more favourable than that in the type II heterojunction system due to the electrostatic attraction between the electrons and the holes. Z-scheme photocatalysts can be classified into three types depending on the mediators involved in the system: Z-scheme with shuttle redox mediators (1st generation), Z-scheme with solid state electron mediators (2nd generation) and direct Z-scheme photocatalysts (3rd generation), shown schematically in Fig. 5b–d.[40]

The 1st generation Z-scheme system consists of two independent semiconductors with the shuttle redox mediators that provide electron acceptor/donor pairs and act as the electron transport in the Z-scheme water splitting reactions (Fig. 5b).[40,41,113,114] Fe^{3+}/Fe^{2+}, IO_3^-/I^- and VO_2^+/VO^{2+} are shuttle redox mediators widely used in this Z-scheme system.[122–124] Although the reported apparent quantum efficiency of the 1st generation Z-scheme system is progressing, several problems have been found in this system.[40] The introduction of redox couples adds intricacies to the system. The low diffusion rate of these ions and the back reactions, such as $Fe^{2+} \rightarrow Fe^{3+}$ or $I^- \rightarrow IO_3^-$, which compete with the reactants for reduction and oxidation reactions, respectively, will consequently reduce the photocatalytic efficiency. This Z-scheme system requires liquid phase reaction and thus its application in the solid and gas phases is limited. The 1st generation Z-scheme system cannot be used for photocatalytic pollutant degradation.

Tada *et al.* proposed the concept of 2nd generation Z-scheme system, which is composed of two different semiconductors and a solid state electron mediator instead of the shuttle redox mediators (Fig. 5c).[125] The ohmic contact between the semiconductors and the mediator allow for rapid recombination between the photogenerated electrons on Semiconductor B and the photogenerated holes on Semiconductor A. Noble metals or reduced graphene oxide (r-GO) are excellent solid state electron mediators for this system.[126,127] Utilization of high conductivity solid state materials as electron mediators inhibits backward reactions. However, the light absorption ability of these materials may compete for light harvesting with the semiconductors, consequently decreasing the photocatalytic efficiency.[40]

The mediator-free Z-scheme was proposed by Yu *et al.*[128] In this system, the electrons and holes can directly transfer between two photocatalysts without the assistance of electron mediators (Fig. 5d). The direct Z-scheme system inherits almost all the advantages in the previous two generation systems, including the effective charge separation and optimized redox ability,[40] and no light-shielding effects as solid state mediators are removed. In designing the direct Z-scheme system, the band structure of the components must be considered carefully. Distinct from the type II heterojunction, in order to construct an effective direct Z-scheme system, the work function of semiconductor "A" must be smaller than that of semiconductor "B" (Fig. 5d).[113] In this scenario, after their contact, free electrons will move from Semiconductor "A" to Semiconductor "B" to flatten the Fermi level, and thus the CB of semiconductor "B" bends downward, and the CB of Semiconductor "A" bends upward. As a result, the transfer of the photogenerated electrons from the CB of Semiconductor "A" to the CB of Semiconductor "B" is forbidden. Instead, the photogenerated electrons at the CB of Semiconductor "B" can readily move to the VB of Semiconductor "A" and recombine with the photogenerated holes therein. As a consequence, electrons with

 This journal is © The Royal Society of Chemistry 2021

higher reducing power and holes with higher oxidizing power are preserved.[129–133] Despite the high efficiency of charge transfer in theory, relaxation and charge recombination at the interface may impede the charge transport,[114] and the formation of a homojunction may be an approach to address these issues.[134,135]

3.2.4 Extending light absorption. The breadth of light absorption and the ability to perform both half reactions need to be considered for photocatalysts. The optimal bandgap for harvesting sunlight is around 1.4 eV, whereas the bandgap for most of the efficient photocatalysts is much wider to ensure sufficient redox potential for the required reaction, and thus the light absorption of these photocatalysts is poor. One feasible way to overcome this dilemma without altering the band structure of the photocatalyst is to introduce a light sensitizer to the system, from which photoelectrons will be generated and injected into the CB of the photocatalyst.

Dye sensitization is a popular strategy to more effectively utilize solar light.[136] In these dye-sensitized photocatalysts, dye molecules are adsorbed on the semiconductor with the required redox potential. When the photocatalytic reaction system is exposed to light, electrons of dye molecules move to occupy the lowest unoccupied molecular orbital (LUMO), then are injected into the CB of the semiconductor to participate in the reduction half reaction (Fig. 6a). Nevertheless, the introduction of the dye molecules and the electron donors increases the complexity of the system, and more back reactions or undesired reactions may take place. Several prerequisites must be satisfied to construct a successful dye-sensitized photocatalyst. First, the dye molecules should have an absorption spectrum widely overlapping with solar radiation and a high molar extinction coefficient. Second, the LUMO of the dye molecules must be more negative than the CB of the semiconductor, while the highest occupied molecular orbital, HOMO, must be more positive than the redox potential of the sacrificial regents. Third, the dye molecules should have long term stability under illumination. Fourth, the dye used for solar energy transfer should be economical. Metal organic dyes such as Ru- or Pt-complexes and metal-free organic dyes such as xanthene-based dyes are frequently used as the light sensitizer.

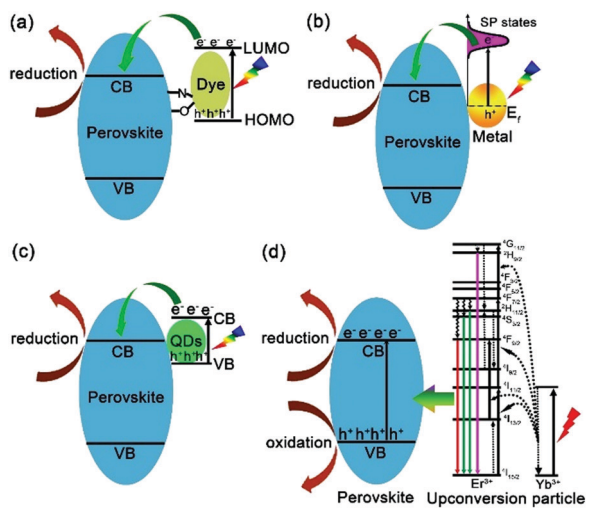


Fig. 6 Schematic of the energy or electron transfer from different sensitizers to perovskite photocatalysts: (a) dye molecules, (b) plasmonic metal (E_f denotes the Fermi level of the metal particle), (c) quantum dots (QDs) and (d) upconversion particles.

Plasmonic nanostructures are another effective component for charge injection. Surface plasmon resonance (SPR) is the collective oscillation of valence electrons at the surface induced by the resonant photon.[137] When the frequency of the photon matches the natural frequency of the oscillation of the surface electrons, the surface electrons will be pushed to the excited state (surface plasmon states) through the SPR process. As the energy of the SPR excited electrons is between −1.0 eV and −4.0 eV on the vacuum scale, while the CB of most photocatalysts is between 0 V and −1.0 V *vs.* SHE (∼−3.5 eV – −4.5 eV on the vacuum scale), the transfer of the excited electrons from the plasmonic particles to the CB of the photocatalysts is allowed. Thus, the energetic electrons are injected into the photocatalyst and play a role in the reduction half reactions (Fig. 6b). Noble metals are plasmonic metal candidates.[138,139] Because of the excellent mobility of the charge carriers, the high absorption cross-section and good stability under illumination, these metallic nanoparticles represent more reliable sensitizers than dye molecules. Moreover, as the resonant wavelength and the SPR intensity are size and shape dependent, there is a probability that the entire solar spectrum can be utilized by careful design of the nanostructures of the plasmonic metal sensitizers.[137] Note that as noble metals are expensive, we suggest that copper,[140] bismuth[141] and some semiconductors with high free carrier concentrations, such as titanium nitride, which shows better SPR than noble metals in certain applications,[142] can be used sustainably as plasmonic candidates.

Quantum dots (QDs) can also be used as light sensitizers for charge injection due to their high absorption coefficient in visible light and the tuneable bandgap that is able to match the whole solar spectrum.[100,143] The energy level of the CB of the QDs can also be tuned by varying their sizes, therefore other than light absorption, the introduction of the QDs may improve the charge separation as well (Fig. 6c).[100] The toxicity of some QDs (containing Pb^{2+}, Cd^{2+} and As^{3-}), however, are still environmental concerns.

Upconversion nanoparticles have been exploited in the context of light harvesting, especially infrared light harvesting, in photocatalysis.[144,145] Upconversion is an anti-Stokes optical process converting a few low energy photons into one high energy photon (Fig. 6d).[146,147] When in contact with the photocatalyst, provided that the energy of the excited ion overlaps the bandgap of the photocatalyst, the upconverted energy will transfer from the upconversion particles to the photocatalyst (Fig. 6d).[148] Therefore, more of the solar spectrum is utilized. Luminescent lanthanide (Ln^{3+})-doped rare-earth fluorides and oxides, such as $NaYF_4$:Yb,Er, are the most well-known upconversion materials used in photocatalytic systems.[147] Nonetheless, the use of upconversion nanoparticles as light sensitizers

is limited. High excitation intensity, such as concentrated sunlight or laser, has to be employed in these systems due to the low efficiency of the upconversion process.[149] The narrow absorption wavelength and the upconverted energy restricted to visible-infrared regions are also obstacles for further application of upconverters.

3.3. Strategies for improving the stability of photocatalytic perovskites

Most of the oxide perovskites are stable during photocatalytic reactions. However, due to the ionic bond structure, many halide perovskites are sensitive to humidity, oxygen, temperature and illumination, hampering their photocatalytic applications.[150] When a halide perovskite ABX_3 is exposed to polar solvent, such as H_2O or DMSO, the solvent molecules can be adsorbed on the surface of ABX_3, and form a monohydrate structure by reacting with the BX_6 octahedra:[151]

$$ABX_3 + H_2O \rightarrow ABX_3{\cdot}H_2O \quad (9)$$

The monohydrate structure will then quickly decompose through hydrolysation:[89,150–152]

$$ABX_3{\cdot}H_2O \rightarrow BX_2 + AX + H_2O \quad (10)$$

If A is methylammonium (MA) or formamidine (FA), the AX can be further hydrolysed, *e.g.*:[152]

$$CH_3NH_3X \rightarrow CH_3NH_2 + HX \quad (11)$$

In addition, the X ions and the CH_3NH_3–X hydrogen bonds will become unstable under illumination because of the charge transfer from halide (VB) to metal (CB), leading to rapid material breakdown.[153] The oxidation half reactions also have negative effects on the perovskite structure. Some X ions (*e.g.*, iodine) and B ions (*e.g.*, Sn^{2+}) may be oxidized, allowing oxygen to enter into the crystal lattice, resulting in variation of properties or even decomposition.[154,155]

To address these issues, and to produce stable halide perovskites as photocatalysts, a number of strategies have been adopted. First, the replacement of the MA or FA with Cs or Rb ions in the A-site, forming an all-inorganic chemical structure, can significantly increase the stability of the halide perovskites.[156] Second, as the polar solvent molecules are the major factors causing structure degradation, carrying out the photocatalytic reactions in non-polar solvents or saturated halo acid solutions is an alternative way to minimize the probability of material breakdown.[157–159] Third, replacing the low-valent B ions with stable ions (*e.g.*, Bi^{3+}, Sb^{3+}), or introducing anions with higher electronegativity in X-site (*e.g.*, Cl^-, O^{2-}) can enhance the tolerance of illumination and the oxidizer generated during photocatalytic reactions.[160–162] Fourth, the formation of heterojunctions, which can prevent the oxidation reactions from occurring on the halide perovskites, benefits the stability of halide perovskites and suppresses electron–hole recombination.[163–166] Lastly, forming a core–shell structure that encapsulates the halide perovskites within a stable shell protects halide perovskites from contacting polar molecules and oxidizer.[167–170]

4. Application of earth-abundant nontoxic perovskites in photocatalysis

4.1. Titanates

Titanium is one of the most abundant metal elements in the earth's crust. Due to its abundance, stability and environmentally friendly characteristics, there has been a large family of titanate perovskites produced, and most of them exhibit excellent structure-dependent photocatalytic activities. Therefore, titanate perovskites and their derivatives have been extensively applied in the areas of photocatalytic water splitting and pollutant degradation (Table S1, ESI†). In this subsection, as a simple and representative perovskite, strontium titanate, $SrTiO_3$ and its development as a photocatalyst illustrate how the above strategies are applied to improve photocatalytic performance. The recent findings and advances of other titanate perovskites and derivatives in photocatalytic applications will also be discussed.

4.1.1 $SrTiO_3$. $SrTiO_3$ (STO), is a typical perovskite with a basic framework of Ti–O polyhedron as TiO_2. As an n-type semiconductor, its CB minimum (CBM) is more negative than TiO_2 and thus it presents a stronger reducing ability than TiO_2.[97] Therefore, STO has attracted significant interest for photocatalysis and has been recognized as a representative photocatalyst for a few decades. Photocatalytic H_2 production was observed on a single crystal STO in a solution with high hydroxide concentration.[171] By reducing the diffusion distance of the charge carriers and increasing the surface area, the photocatalytic activities of STO improved.[108] However, Townsend *et al.* reported that 30 nm STO particles were about 35% less active than the bulk sample, and 6 nm particles have only 10% of the activity.[172] They suggested that the key factor resulting in the decrease of activity was the quantum size effect in the nanoparticles, which extended the bandgap and reduced the light absorption, meanwhile the water oxidation overpotential was increased with reduction in particle size.

The morphology of the STO nanoparticles also have significant impact on their photocatalytic activity. Yu *et al.* synthesised the three-dimensionally ordered macroporous STO photocatalyst *via* sol–gel methods with polymer colloidal crystal templates. The highest hydrogen evolution rate was 3599 μmol g^{-1} h^{-1} for the optimized sample.[173] The high photocatalytic activity of this nanostructure was attributed to the exact overlap between the stop band of the macroporous STO and the bandgap of STO, by which the slow photon effect was triggered and light absorption was increased.

More precise control of the morphologies enabled the STO nanoparticles to expose specific facets, and hence spatial charge separation would be encouraged due to the different location of the oxidation and reduction active sites. Wang *et al.* reported the synthesis of STO nanoparticles enclosed with {023} facets and {001} facets through a solvothermal method, showing high H_2 and O_2 evolution rate.[174] This was ascribed to the spatial separation of photoreduction and photooxidation active sites on different facets. Li *et al.* further confirmed the locations of the active sites for reduction and oxidation by facet-selective

 This journal is © The Royal Society of Chemistry 2021

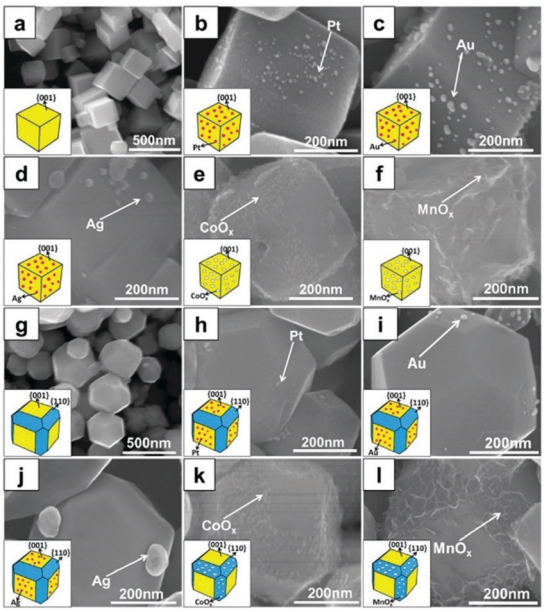


Fig. 7 The SEM images of the (a–f) 6-facet and (g–l) 18-facet $SrTiO_3$ nanocrystals with photo-deposition of noble metals or metal oxides. Reprinted with permission.[175] Copyright 2016, Royal Society of Chemistry.

photo-deposition of metals and oxides. They concluded that reduction reactions preferred to take place on the {001} facets and oxidation reactions tend to occur on the {110} facets provided that the nanoparticles were enclosed by both of these facets, but the distribution of the active sites of the reduction and oxidation would be even had the nanoparticles exposed only the {001} facets (Fig. 7).[175] Therefore, the AQY in photocatalytic water splitting of the 18-facet STO nanoparticles (composed of {001} and {110} facets) was five times more than that of the 6-facet STO nanoparticles (composed of {001} facet).

STO has been doped to achieve visible light activity with a number of simple B-site doping options attempted, such as Cr, Ni, Al, Fe and Mn.[90,95,176–180] To prevent formation of recombination centres with the introduction of lower valence dopants, B-site co-doping (such as Cr/Ta,[94] Cr/Sb,[181] and Ni/Nb,[95]) and A/B-site co-doping (such as La/Cr,[96,97] Ag/Nb,[91] La/Rh,[44] and La/Ni[182]) were explored. Ye *et al.* reduced the bandgap of STO to 2.1 eV by co-doping La^{3+} and Cr^{3+}, and the AQY of H_2 evolution reached 25.6% in aqueous CH_3OH solution containing 5 M NaOH under visible light.[96] Takata *et al.* achieved an AQY of 96% of the UV region, using Al-doped STO photocatalysts (Fig. 8).[183] X-site doping with N or F has also been intensively studied for adjusting the bandgap and the VBM,[9,15] while the A/B-site and X-site co-doping with La/N and Cr/N were utilized to compensate the charge induced by the anion defects.[184,185] In addition to the introduction of foreign elements, self-doped or electron-doped $SrTiO_{3-x}$ samples were prepared by co-precipitation then calcination at 1200 °C in an Ar atmosphere.[186] An optimum concentration of oxygen vacancies can improve the charge separation of the carriers and visible light absorption, resulting in enhanced photoactivity.[187,188]

The formation of heterojunctions with co-catalysts is essential for the improved performance of the photocatalytic reactions. The Ni@NiO_x core–shell structure is a highly efficient co-catalyst on STO, whose efficiency is comparable with that of noble metal co-catalysts (*e.g.*, Pt, Rh),[189–191] and thus we suggest that Ni@NiO_x can be a potential substitute for noble metal co-catalysts. Type II heterojunctions were achieved by combining Cr-doped STO with Ag_3PO_4 which can spatially separate the electrons and holes.[192] Wei *et al.* developed a STO-TiO_2 heterogeneous hollow multi-shelled structure, in which the AQY is 8.5% (Fig. 9).[193] The large surface area, the charge separation induced by the hollow structure, and the hierarchical shells enabling multiple reflections of the incident light increasing light harvesting were attribute to the high photocatalytic performance.[193] Coupling STO with carbon QDs exhibited enhanced photocatalytic performance on Rhodamine B (RhB) degradation, ascribed to the visible light absorption and the electron extraction of the carbon QDs.[194]

Z-scheme systems have been constructed to simultaneously optimize redox ability and spatial charge separation for the STO-based photocatalysts.[129,179,195] Chen *et al.* used the Ta/Cr co-doped STO as a H_2 evolution photocatalyst, WO_3 as the O_2-evolution photocatalyst, and IO_3^-/I^- as the shuttle redox mediator to build a 1st generation Z-scheme system. The H_2

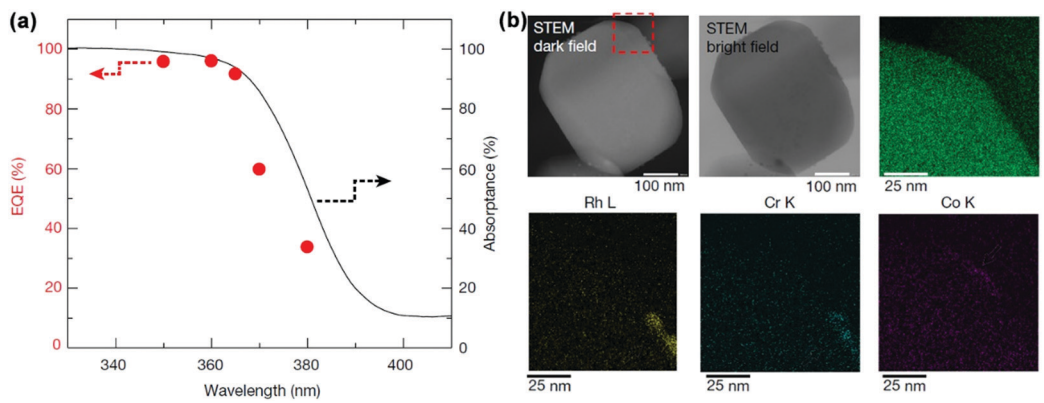


Fig. 8 (a) Reflectance spectrum of STO:Al (black solid line) and wavelength *vs.* water splitting AQY on Al-doped STO photocatalyst (red spots). (b) STEM and EDS mappings of the Al-doped STO photocatalyst. EDS data were obtained from the area in the red dashed box. Reproduced with permission.[183] Copyright 2020, Nature Publishing Group.

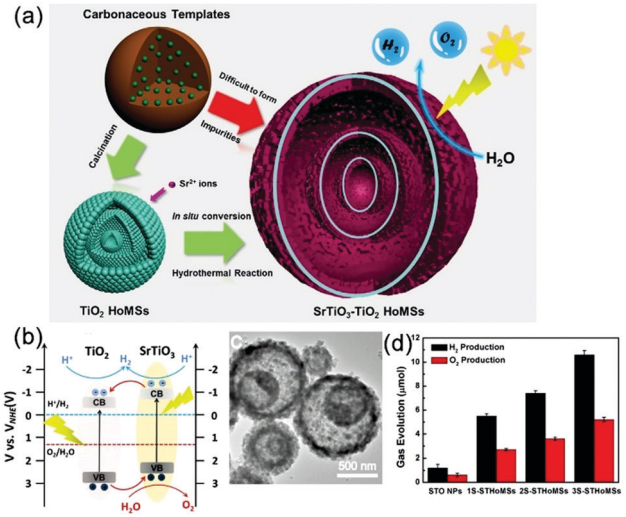


Fig. 9 (a) Schematic of the hydrothermal synthesis of STO@TiO_2 hollow multi-shelled structures (HoMSs); (b) The band structure and (c) the TEM image for STO@TiO_2 HoMSs. (d) Photocatalytic water splitting performance of single-shelled (1S), double shelled (2S) and triple shelled (3S) STO@TiO_2 HoMSs. Reproduced with permission.[193] Copyright 2019, Wiley-VCH Verlag GmbH & Co. KGaA, Weinheim.

evolution rate achieved was 122.6 μmol h^{-1}.[195] An all solid state Z-scheme heterojunction, Ag_3PO_4@MWCNT@Cr:STO with excellent visible light photocatalytic activity was synthesised, in which the MWCNT served as a solid state electron mediator, the holes were found in Ag_3PO_4 and superoxide radicals formed on Cr:STO, indicating superior charge separation.[179] Loading plasmonic metallic nanoparticles on the surface of STO can further improve photoreduction due to charge injection from the nanoparticles to the CB of STO *via* SPR.[196,197]

4.1.2 Other $ATiO_3$. Other titanates including $CaTiO_3$ and $BaTiO_3$ have been reported as UV and visible light photocatalysts. $CaTiO_3$ due to its low cost, facile synthesis and high chemical stability, is considered as a promising photocatalyst, especially in moist environments.[198] Compared with STO, $CaTiO_3$ possesses a more negative CBM (−0.94 V *vs.* SHE) and more positive VBM (+2.76 V *vs.* SHE), and thus it is extensively applied for water splitting and pollutant removal.[199] To extend the light absorption, size/morphology control and doping (Cu, Zn, Pr, Ag/La, La/Cr, Na/Er, *etc.*) were reported.[198–203] Noble metal particles have been loaded on titanates for visible light harvesting *via* SPR.[204,205] A Z-scheme heterojunction was obtained for AgCl/Ag/$CaTiO_3$ and under UV light irradiation excellent enhancement of photocatalytic hydrogen production was achieved.[126] These results indicate that AgCl/Ag/$CaTiO_3$ can serve as a photocatalyst for both water splitting and pollutant degradation under different incident light.

$BaTiO_3$ is another attractive titanate in photocatalysis due to its relatively smaller bandgap and piezoelectric properties.[206,207] To enhance the optical properties and increase photocatalytic activity, doping is commonly applied and Fe, Ce or Cr-doped $BaTiO_3$ have been studied in detail.[208–210] Heterojunctions combining $BaTiO_3$ with other functional semiconductors have been investigated to boost the light absorption and suppress the electron–hole recombination. $CuBi_2O_4$, due to its narrow bandgap and more negative CBM (−0.63 V *vs.* SHE), was coupled with $BaTiO_3$ and $BiFeO_3$ to form a double Z-scheme.[211] The $CuBi_2O_4$ served as the light sensitizer absorbing visible light and capturing electrons from the CB of $BaTiO_3$ and $BiFeO_3$, enhancing charge separation and reduction ability. By taking advantage of the ferroelectric polarization of $BaTiO_3$, the charge separation efficiency can be increased further.[212–214] Intriguingly, Xu *et al.* synthesised an $Au_x/BaTiO_3$ photocatalyst, in which the formation of $OH^•$ was promoted by the piezoelectric field originating from $BaTiO_3$ and the SPR-induced enhancement of carrier separation, resulting in a strong oxidizing ability for pollutants.[215]

4.1.3 Ti-based double perovskites. The Ti-based double perovskites are beginning to demonstrate their superior photocatalytic performance and the flexibility of structure–property adjustment. La_2FeTiO_6 showed superior visible light photocatalytic reactions for the degradation of *p*-chlorophenol to that of the $LaFeO_3$.[216] The high surface area, small particle size, narrow bandgap and the high concentration of oxygen vacancies of La_2FeTiO_6 were deemed to be the reasons for this improved photocatalytic performance. Hailili *et al.* selected $CaCu_3Ti_4O_{12}$ as a model to study the effects derived from defects due to the abundant oxygen vacancies and metal ion defects (Cu^+ and Ti^{3+}) on the surface.[217] Further investigations along with the DFT calculation indicated that both the bandgap and the potential of the CB and VB are distinct in the {001} and {111} facets of $CaCu_3Ti_4O_{12}$, while the formation of oxygen vacancies was preferred on the {001} facets and the formation of metal defects was on the {111} facets.[218] For these reasons, the electrons in the CB of the {001} facets would move to the CB of the {111} facets through a type II heterojunction mechanism, and thus electron–hole pairs could be separated effectively. More importantly, defect-dipoles would form with increasing defect concentration, and such defect-dipoles effected the charge separation by creating an internal field on the surface.

4.1.4 Layered Ti-based perovskites. Layered perovskites, due to the anisotropic charge transfer and electronic properties caused by the alternating layers, exhibit intriguing photocatalytic activities. There are four types of layered Ti-based perovskites: RP, AL, {110} and {111} perovskites. $A_2La_2Ti_3O_{10}$ (A = alkali metal) is a series of typical RP Ti-based perovskites presenting high UV water splitting activity. They are composed of octahedral perovskite-layers ($La_2Ti_3O_{10}^{2-}$), between which A^+ ions are located.[219] These perovskites are easily hydrated in water, *i.e.*, the A^+ can be exchanged with the protons in the H_2O molecules. Therefore, they are excellent water splitting photocatalysts.[220] Nevertheless, $A_2La_2Ti_3O_{10}$ photocatalysts usually operate under UV irradiation due to their wide bandgap. To enhance their photoactivities under visible light, transition metal ions and N were selected to dope the $A_2La_2Ti_3O_{10}$.[221–225] Alternatively, water molecules were intercalated between the perovskite layers of $A_2La_2Ti_3O_{10}$ to increase the interlayer space, resulting in better charge separation.[226]

Another well-documented RP Ti-based perovskite is Sr_2TiO_4. Sr_2TiO_4 has the highest level of structure lamination among all

 This journal is © The Royal Society of Chemistry 2021

$Sr_{n+1}Ti_nO_{3n+1}$ ($1 \leq n \leq \infty$), where n denotes the thickness of the perovskite layer ($n \times SrTiO_3$) terminated on both sides by SrO.[227] This special layered structure endows Sr_2TiO_4 with anisotropic charge transportation (the charge can only transfer in-plane rather than along the c axis), in that the CBM and VBM of Sr_2TiO_4 are buried in the TiO_6 octahedron layers.[227] Therefore, the interlayer charge recombination is prohibited, thereby contributing to the photocatalytic activities. A/B and A/X co-doped Sr_2TiO_4 were reported for the visible-light driven hydrogen production.[227–229] Importantly, a type II heterojunction combining La/Cr co-doped STO and La/Cr co-doped Sr_2TiO_4 was prepared to improve the charge transfer and alleviate the electron–hole recombination.[230] The H_2 evolution rate of this heterojunction increased 6.4 times and 3.0 times compared to the individual La/Cr co-doped STO and La/Cr co-doped Sr_2TiO_4, respectively.

AL Ti-based perovskites possess good optical, ferroelectric and optoelectronic properties. Among them, $Bi_4Ti_3O_{12}$ has been widely studied due to its unique structure.[231] $Bi_4Ti_3O_{12}$ consists of the alternate stacking of the $(Bi_2Ti_3O_{10})^{2-}$ triple perovskite slab and a monolayer of $Bi_2O_2^{2+}$. The $(Bi_2Ti_3O_{10})^{2-}$ layer is composed of three TiO_6 octahedral perovskite layers with the Bi^{3+} at the A-site and sandwiched between the $Bi_2O_2^{2+}$ layers along the c axis. The ferroelectricity derived from the perovskite layers and the anisotropic charge transfer behaviours along the *ab*-plane contribute to the charge separation. Simultaneously, the involvement of the Bi 6p orbitals in the CB and the Bi 6s orbitals in the VB reduce the bandgap, and the large number of oxygen vacancies from the $Bi_2O_2^{2+}$ layer extend the wavelengths of absorption.[232] As a result, this compound was considered as a promising photocatalyst for water splitting by Kudo *et al.*[233] The Fe-doped $Bi_4Ti_3O_{12}$ achieved visible-light photodegradation of phenol and bisphenol A due to the emergence of the occupied Fe 3d orbitals in the middle of the bandgap.[234] Increasing exposure of the active {001} facet by tuning the morphology, on the other hand, contributed to the photocatalytic activities through offering more active sites and suppressing recombination rates.[235] Interestingly, an increase of the Cr^{3+} dopants led to particle agglomeration during synthesis, resulting in more exposure of the inactive {010} facet.[236] As a multiferroic material, the band alignment and the charge transport of $Bi_4Ti_3O_{12}$ are also affected by the piezoelectric effect. By introducing ultrasonic waves to the system, the piezoelectric effect was triggered and accelerated the separation of the electrons and holes.[237]

To gain better photocatalytic performance, $Bi_4Ti_3O_{12}$ was coupled with plasmonic metallic particles or narrow bandgap semiconductors such as CuS and $BiVO_4$ to form type II heterojunctions.[238–240] In particular, due to the stable 2D–2D face contact, the formation of heterojunctions between $Bi_4Ti_3O_{12}$ and the other layered compounds with narrow bandgap, including g-C_3N_4 and BiOI, was in high preference.[241,242] The enhancement of the photocatalytic activities of these 2D–2D heterojunctions was attributed to more effective charge transfer between the two components and the establishment of polarization fields.[242]

Considering the large bandgap and the weak polarization of $Bi_4Ti_3O_{12}$, another AL Ti-based perovskite with smaller bandgap, $Bi_5FeTi_3O_{15}$, was investigated. $Bi_5FeTi_3O_{15}$ has a four layer perovskite unit of $(Bi_3FeTi_3O_{13})^{2-}$ (formed by inserting one $BiFeO_3$ unit into the $(Bi_2Ti_3O_{10})^{2-}$ triple perovskite slab) sandwiched by two $(Bi_2O_2)^{2+}$ layers along the *c*-axis.[243] The hybridization of Fe 3d orbitals with Ti 3d orbitals reduces the CBM, and the Fe^{3+} existing in the perovskite slabs helps to enhance the ferroelectricity, which plays an essential role in charge separation.[243] Recently, a Z-scheme system was constructed by a 2D/2D $Bi_5FeTi_3O_{15}$/g-C_3N_4 heterojunction with Ag particles as the solid state electron mediator for photocatalytic pollutant degradation.[244] The high efficiency of the photocatalytic reaction was ascribed to the high-speed Z-scheme path that accelerated the charge transfer in the 2D/2D heterojunction. Other AL Ti-based perovskites, such as $BaLa_4Ti_4O_{15}$,[233] Bi_3TiNbO_9,[245] and $Sr_2Ba_2Nb_2TiO_{12}$,[246] have also been investigated.

For the Ti-based {110} type perovskites, $La_2Ti_2O_7$ is one of the most frequently used in photocatalysis. In $La_2Ti_2O_7$, the perovskite slabs are formed by the corner-shared TiO_6 octahedrons and La ions stack along the [110] direction.[247] Abe *et al.* showed that such a corner-shared perovskite network played pivotal roles in the high performance photocatalysts, however the wide bandgap of this compound hampered its photocatalytic application.[248] The bandgap of $La_2Ti_2O_7$ was reduced by introducing various dopants.[61,249] Type II heterojunctions combining $La_2Ti_2O_7$ with other 2D narrow bandgap semiconductors, forming N-doped $La_2Ti_2O_7$/g-C_3N_4,[250] $La_2Ti_2O_7$/Bi_2WO_6,[251] and $La_2Ti_2O_7$/BiOBr,[252] were synthesised to extend light absorption and improve charge separation. To further enhance the photocatalytic efficiency, Meng *et al.* described a combination of Au@N-doped $La_2Ti_2O_7$/r-GO extending the wavelength of the incident light absorption to 600 nm.[253] In this structure, r-GO served as an electron mediator, extracting electrons from the N-doped $La_2Ti_2O_7$ and facilitating the reduction reaction, and hot electrons were generated by Au particles through SPR then transferred to the CB of $La_2Ti_2O_7$, resulting in synergistic enhancement of the photocatalysis. Zhu *et al.* anchored black phosphorus onto Au@$La_2Ti_2O_7$ as a near infrared (NIR) light sensitizer.[254] Therefore, SPR could be induced by NIR light and this heterojunction exhibited photocatalytic activity for H_2 evolution at wavelengths up to 780 nm. Besides noble metal particles, metal hydroxides were loaded on $La_2Ti_2O_7$ as well. Boppella *et al.* sandwiched the $La_2Ti_2O_7$ nanosheets with a Ni/Fe double hydroxide layer (as hole capturer) and r-GO layer (as electron extractor) to effectively separate electrons and holes.[255] The H_2 evolution rate of this novel heterostructure was 532 μmol g^{-1} h^{-1}, which was a 9-fold increase compared to the pure $La_2Ti_2O_7$.

$La_4Ti_3O_{12}$ and $ALa_4Ti_4O_{15}$ (where A is Ca^{2+}, Sr^{2+} and Ba^{2+}) are the typical {111} type perovskites. The bandgaps of $CaLa_4Ti_4O_{15}$, $SrLa_4Ti_4O_{15}$ and $BaLa_4Ti_4O_{15}$ were 3.78, 3.82 and 3.85 eV, which was reverse in order of bandgap change to that of $ATiO_3$.[85] The positions of La^{3+} and A^{2+} in the crystal structure of $ALa_4Ti_4O_{15}$ affect their bandgap and electronic properties. In $BaLa_4Ti_4O_{15}$, the large radius of Ba^{2+} enlarges the layer distance, and

thus reduces the interaction between layers, resulting in more localized excited energy states. Therefore, $BaLa_4Ti_4O_{15}$ possesses a wider bandgap than $CaLa_4Ti_4O_{15}$ and $SrLa_4Ti_4O_{15}$. On the other hand, the ratio of La^{3+} and Ba^{2+} was 1 : 1 at the interlayer and only La^{3+} exists in the perovskite layer, whereas due to the approximately similar radius of La^{3+} and Ca^{2+}, Ca^{2+} and La^{3+} exist randomly in both the interlayer and perovskite layer.[85] The ordered distribution of the La^{3+} ions and Ba^{2+} ions endows $BaLa_4Ti_4O_{15}$ with stronger anisotropic properties than $CaLa_4Ti_4O_{15}$ and $SrLa_4Ti_4O_{15}$, whereby the active sites of oxidation and reduction are separated. Besides, the anisotropic structure of $BaLa_4Ti_4O_{15}$ enhances its polarization ability. Therefore, $BaLa_4Ti_4O_{15}$ shows strong photocatalytic activities in water splitting, pollutant degradation and CO_2 reduction.[85,256,257] Co-catalysts were loaded on $BaLa_4Ti_4O_{15}$ to further improve the efficiency.[257,258] The highest AQY (16%) was achieved by the $Rh_{2-x}Cr_xO_3$ loaded 1.3 nm $BaLa_4Ti_4O_{15}$, but the cost of Rh-based co-catalyst would be a practical concern.[258] A ternary heterojunction $Au@Cr_2O_3$–$BaLa_4Ti_4O_{15}$ was also prepared, in which the Cr_2O_3 shell was able to prevent the backward reaction of O_2 evolution.[259] The water splitting photoactivity of this novel structure therefore was improved 19 times compared with the $Au@Cr_2O_3$–$BaLa_4Ti_4O_{15}$ sample.

4.2. Ferrites

Ferrite perovskites, primarily $BiFeO_3$ or $LaFeO_3$, have found application in photocatalysis. The doping or formation of heterojunctions have been studied to improve the photocatalytic performance of these ferrites, as will be outlined in the sections below and are summarized in Table S2 (ESI†).

4.2.1 $BiFeO_3$. $BiFeO_3$ is one of the best known Fe-based perovskites due to its relatively narrow bandgap, large remnant polarization and high Curie temperature.[260] As a multiferroic material, $BiFeO_3$ possesses the combination of ferroelectricity, antiferromagnetism and ferroelasticity, and therefore it has been investigated for application in photovoltaic cells, memristive devices and photocatalysis. $BiFeO_3$ is a p-type semiconductor with a bandgap of 2.0–2.8 eV, determined by the separation of the top of the O 2p–Fe 3d hybridized VB located at around +2.3 V *vs.* SHE and the bottom of the CB composed of Fe 3d orbitals with a potential around +0.3 V *vs.* SHE.[261] As a result, the band structure of $BiFeO_3$ strongly depends on the Fe–O bonding interaction. In other words, the band structure of $BiFeO_3$ would be affected by size, morphology and even method of synthesis, which may impact the Fe–O bonds.[262] In the $BiFeO_3$–graphene heterostructures, an enhanced coupling between $BiFeO_3$ and graphene resulted in strong covalent O–C bonds and decreased charge transfer from oxygen to the Fe ion, and therefore the bandgap of $BiFeO_3$ was reduced.[263] In addition to modulation of the Fe–O bonds, other strategies have been attempted to increase light absorption. Mesoporous $BiFeO_3$ hollow spheres were prepared by aerosol-spraying.[264] The multiple light reflections in the hollow sphere caused more pronounced light absorption. Due to the increased light absorption and the large surface area, these mesoporous $BiFeO_3$ hollow spheres showed strong activities in the photodegradation of RhB and 4-chlorophenol.

Doping is an alternative strategy to reduce the bandgap of $BiFeO_3$ and enhance the photoactivity. $BiFeO_3$ nanoparticles doped with Ba, Ca, Mn, Ln or Gd/Sn, Sr/Co, La/Se have shown good photocatalytic activities in the degradation of pollutants (*e.g.*, Congo red (CR), RhB, phenol, *etc.*) due to a decrease in bandgap:[265–273] among them the La/Se co-doped $BiFeO_3$ exhibited a tunable bandgap from 2.06 to 1.94 eV by changing the La^{3+} and Se^{4+} content.[271] Notwithstanding the narrow bandgap and the high photoactivity, $BiFeO_3$ has been utilized more for photocatalytic degradation than water splitting because the CB of $BiFeO_3$ is more positive than the redox potential of H_2/H_2O (Fig. 4). To achieve photocatalytic water splitting, the potential of the CBM must be shifted to a more negative position. Vishwakarma *et al.* investigated the Gd/Co co-doped $BiFeO_3$ prepared by a facile sol–gel method, where the H_2 evolution rate was 74 μmol cm^{-2} h^{-1}.[274] The high photocatalytic activity for H_2 production was ascribed to the distortion of Fe–O octahedrons induced by the doping ions that affected the position of the CBM. Lu *et al.* developed a novel $BiFeO_3$–$SrTiO_3$ solid solution *via* a hydrothermal method. In this solid solution, the orbital hybridization of Ti 3d and Fe 3d gave a more negative CBM, meanwhile the mixture of O 2p orbitals and the spin-polarized band of Fe ensured the bandgap was in the range of visible light.[275] The H_2 evolution rate was recorded as 50 μmol h^{-1}.

Despite the inferior photocatalytic activity compared with the Ti-based perovskites, the superior ferroelectricity of $BiFeO_3$ facilitates the charge separation, and thus $BiFeO_3$ has been extensively integrated with other semiconductors for better photocatalytic performance. One of the most documented $BiFeO_3$-based heterojunctions is the combination of p-type $BiFeO_3$ with n-type TiO_2 as a p–n junction.[276,277] To increase the contact area to improve charge transfer, $BiFeO_3$ particles were deposited on TiO_2 with various nanostructures, such as $BiFeO_3$–TiO_2 nanotubes,[278] nanofibres,[279] and multilayer films.[280] A heterojunction of porous $BiFeO_3$ and TiO_2 with enhanced visible light activities was synthesised by Humayun *et al.*[276] The built-in electric field at the $BiFeO_3/TiO_2$ interface could drive the visible-light generated electrons to the CB of TiO_2, significantly suppressing the recombination and raising the reducing power. The photocatalytic activity of the $BiFeO_3$–TiO_2 heterojunction was further improved by the piezoelectric polarization feature of $BiFeO_3$. Liu *et al.* showed that ultrasonic vibration introduced to the photocatalytic degradation system with the $BiFeO_3$–TiO_2 core–shell structure as catalyst caused piezoelectric polarization that resulted in a steeper bending of the bands at the p–n junction interfaces, whereby the separation of the electrons and holes were significantly enhanced (Fig. 10).[277] In addition to TiO_2, other n-type semiconductors having strong photocatalytic activity, such as $BiVO_4$ and g-C_3N_4, were combined with $BiFeO_3$.[281–284]

To further enhance light absorption, light sensitizers are deposited on $BiFeO_3$. For example, loading Au nanoparticles on $BiFeO_3$ extended the absorbance to 600 nm, enhancing the photocatalytic water oxidation under visible light.[285] As the absorbance of $BiFeO_3$ spectrally overlaps with the upconversion

 This journal is © The Royal Society of Chemistry 2021

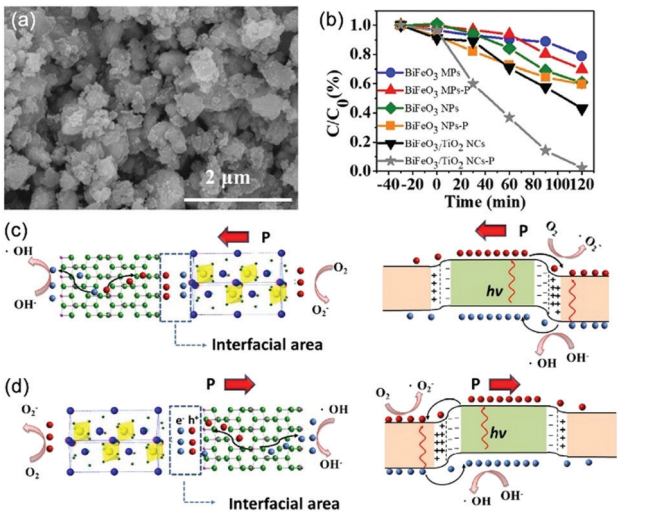


Fig. 10 (a) SEM image of the $BiFeO_3/TiO_2$ core/shell nanocomposites; (b) the piezo-phototronic degradation activity for various structures (MPs: micrometre-sized particles, NPs: nanoparticles, NCs: nanocomposites, P: poling); (c) and (d) the piezo/photo-catalysis process of the $BiFeO_3/TiO_2$ core/shell structures for the different polarization direction. Reproduced with permission.[277] Copyright 2019, Elsevier.

emission of $NaYF_4$:Yb,Er, a $NaYF_4$:Yb,Er@$BiFeO_3$ core@shell structure was fabricated to photodegrade 4-chlorophenol and methylene orange under 980 nm irradiation.[173] The combination of $BiFeO_3$ with upconversion materials would be a promising design for the utilization of infrared radiation in photocatalysis.

4.2.2 Other Fe-based perovskites. There are a number of ferrites that have been prepared as visible light catalysts for water splitting and pollutant degradation: $LaFeO_3$, $PrFeO_3$, $SrFeO_{3-x}$ and $GaFeO_3$.[106,286–289] $LaFeO_3$ is a p-type semiconductor with a bandgap of ~2.3 eV.[290] Due to its low cost, high stability, non-toxicity and narrow bandgap, $LaFeO_3$ is considered as a promising photocatalyst under visible light. However, the activity of $LaFeO_3$ in the reduction half reactions is weak (CBM: ~+0.2 V *vs.* SHE).[291] Several approaches have been developed to modulate the band structure of $LaFeO_3$. Garcia-Muñoz *et al.* found that Ti-doped $LaFeO_3$ showed visible light activity in photocatalytic wet peroxide oxidation and photodegradation simultaneously.[292] The high activity of this catalyst was attributed to the Ti dopants that affected the CBM and provided more electrons for the Fe^{3+} to facilitate the Fe^{3+}/Fe^{2+} reduction. Heterojunctions integrating $LaFeO_3$ with another n-type semiconductor having a more negative CB is an alternative route to enhance the reducing power. Humayun *et al.* prepared Bi-doped porous $LaFeO_3$ coupled with ZnO.[291] Since ZnO is an n-type semiconductor and the CBM is −0.1 V *vs.* SHE, a built-in field will be established at the $LaFeO_3$/ZnO interface, driving the photogenerated electrons from the CB of $LaFeO_3$ to the CB of ZnO, hence the reduction activity was improved. This photocatalyst therefore exhibited good activity for 2,4-DCP degradation and CO_2 conversion. Direct Z-scheme systems were constructed through the combination of $LaFeO_3$ and g-C_3N_4.[293,294] Higher photocatalytic activities compared with either g-C_3N_4 or $LaFeO_3$ for photocatalytic pollutant degradation and water splitting were displayed in these composites. Other ferrites, such as $GaFeO_3$, were also reported to be active in photocatalytic water splitting. Interestingly, the $GaFeO_3$ nanoparticles with a distinctive morphology, truncated hexagonal bipyramid, could be prepared by a facile hydrothermal method. The presence of the defects at the exposed facets might be responsible for the high activity of these $GaFeO_3$ nanoparticles.[295]

4.3. Niobates

The niobate perovskites discussed here include $KNbO_3$, $NaNbO_3$, $AgNbO_3$, $Sr_2Nb_2O_6$, $Sr_2Nb_2O_7$ and layered derivatives. Photocatalytic studies of these niobates, doped forms of these materials and heterojunctions including these niobates are listed in Table S3 (ESI†).

4.3.1 $KNbO_3$. Potassium niobates, $KNbO_3$, are nontoxic and have high stability, variant phases, strong ferroelectricity and corner-shared octahedral units of NbO_6 in the network, therefore have attracted substantial interest in photocatalysis research.[296] In particular, $KNbO_3$ possesses a CBM as negative as −0.8 V *vs.* SHE,[297] which allows $KNbO_3$ to be used as a photocatalyst for water splitting and pollutant degradation, as well as to achieve photocatalytic N_2 fixation (Table S3, ESI†). In general, bulk $KNbO_3$ presents a number of temperature-dependent phases such as monoclinic, orthorhombic, tetragonal and cubic.[298,299] Various phases of $KNbO_3$ nanoparticles can be synthesised by carefully controlling the experimental parameters, with the cubic $KNbO_3$ giving the best photocatalytic performance.[298] According to DFT calculation, the CB in cubic $KNbO_3$ was highly delocalized and involved the orbitals of both O and Nb, resulting in facile electron excitation and transfer as the electrons were capable of moving in all three dimensions. When the crystal symmetry was low, the CB was localized and restricting the electron mobility to one direction, reducing electron activity. Nevertheless, the orthorhombic $KNbO_3$ displayed higher activity than the tetragonal $KNbO_3$, because the facets enclosing the orthorhombic $KNbO_3$ were more active than those exposed in the tetragonal $KNbO_3$. In the case of monoclinic $KNbO_3$, charge separation was impaired due to decreased ferroelectricity compared with the orthorhombic $KNbO_3$, leading to lower photocatalytic activity.[299] Morphology also contributes to the photoactivity of $KNbO_3$. In the 1D $KNbO_3$ nanostructures, the anisotropic nature improved electron transfer along the longitudinal direction, while the holes would drift laterally to the surface.[299,300] Due to high photoactivity and anisotropic nature, most studies used the orthorhombic phase to produce 1D $KNbO_3$ nanostructures. Photocatalytic activity was dependent on the aspect ratio of the 1D orthorhombic $KNbO_3$ nanostructure: the larger the aspect ratio, the more active the $KNbO_3$ nanostructure.[300]

Doping has been considered as one of the most effective ways to reduce the bandgap of $KNbO_3$. The bandgap of the N-doped $KNbO_3$ nanocubes could be reduced to 2.76 eV,[301] and the carbon-doped $KNbO_3$ showed high photocatalytic activity with a hydrogen generation rate of 142 μmol g^{-1} h^{-1} and

211 μmol g^{-1} h^{-1} under visible light and UV light, respectively.[302] Deposition of metal particles on $KNbO_3$ is another way to enhance light absorption and charge separation.[300,303] Xing *et al.* demonstrated the excellent performance of plasmonic Ag-loaded $KNbO_3$ nanorods in photocatalytic N_2 fixation, H_2 production and pollutant degradation.[303] Piggott *et al.* reported a novel Au/$KNbO_3$ photocatalyst with superior activity in nitroarene reduction due to the efficient charge transfer from the CB of $KNbO_3$ to Au.[304] However, replacement of the noble metal co-catalysts with other earth-abundant materials would be required to lower production cost. In addition, heterojunctions were constructed for broadening the wavelengths of absorption and achieving more efficient charge separation. Zhang *et al.* revealed that in the heterojunction of $KNbO_3$/r-GO, the extent of reduction of r-GO influenced the bandgap of $KNbO_3$ due to the number of O atoms present in the graphene layer.[305] Hence $KNbO_3$/r-GO exhibited UV activity in water splitting and visible light activity in pollutant degradation.[306,307] Other heterojunctions, such as $KNbO_3/MoS_2$, $KNbO_3$/g-C_3N_4 and $KNbO_3$/carbon QDs, were also synthesised for photocatalytic water splitting and pollutant degradation.[297,308,309]

4.3.2 $NaNbO_3$. Due to the fast charge transfer caused by the NbO_6 octahedron network, similar to $KNbO_3$, $NaNbO_3$ is expected to have potential for photocatalytic water splitting and pollutant degradation.[310] Compared to $KNbO_3$, however, $NaNbO_3$ showed relatively lower photocatalytic activity because of its larger bandgap and antiferroelectric property.[311] Nevertheless, because of its high stability in redox reactions, $NaNbO_3$ attracted attention in the development and investigation of high efficiency Nb-based photocatalysts in recent years. Similar to $KNbO_3$, cubic $NaNbO_3$ displayed higher activity for H_2 production under UV light than the orthorhombic $NaNbO_3$, which was ascribed to the more delocalized CB and less distorted O–Nb–O bonds that shifted the VB to a more negative level, thus reducing the bandgap.[310] By taking advantage of the difference in bandgap between cubic and orthorhombic $NaNbO_3$, a type II heterojunction of cubic-$NaNbO_3$/orthorhombic-$NaNbO_3$ was established, enhancing the charge separation.[312] Moreover, doping cations (such as Ca or V) or anions (such as N) into $NaNbO_3$ also contributed to the reduction of bandgap.[313–315]

Significant effort has focused on the construction of heterojunctions to improve the photocatalytic activity of $NaNbO_3$. Shi *et al.* reported enhanced photocatalytic CO_2 reduction using the $NaNbO_3$/g-C_3N_4 nanocomposite, which forms a type II heterojunction,[316] and investigations showed the $NaNbO_3$/g-C_3N_4 nanocomposite removed organic pollutants in water under visible light.[317] As both $NaNbO_3$ and g-C_3N_4 are n-type semiconductors, however, the charge transfer between these two components was not efficient. To improve the charge transfer efficiency and acquire higher redox ability, some narrow bandgap p-type semiconductors were considered for the formation of p-n junctions. Sun *et al.* combined the n-type $NaNbO_3$ with p-type BiOI, giving nearly 100% methylene blue degradation after 100 min under visible light.[318] Kumar *et al.* prepared $NaNbO_3/MoS_2$ and $NaNbO_3/BiVO_4$ core–shell structures and compared their photoactivities (Fig. 11).[319] Due to suitable lattice matching and the formation of p–n junctions, $NaNbO_3/MoS_2$ was more compatible for photocatalytic applications, and the H_2 evolution rate was 61 μmol h^{-1}. Regarding the $NaNbO_3/BiVO_4$ core–shell structure, $BiVO_4$ exhibited p-type behaviour in this heterojunction despite being an n-type semiconductor, as the Fermi level of $BiVO_4$ was lower than that of $NaNbO_3$. Therefore, the electron transfer from $BiVO_4$ to $NaNbO_3$ was not as thermodynamically favourable as that in the $NaNbO_3/MoS_2$ structure. An alternative way to overcome the issues of connecting two n-type semiconductors was to form a Z-scheme system.[320,321] A ternary heterojunction was also attempted. Yang *et al.* constructed the Pt/N-doped $NaNbO_3$/N-doped r-GO structure, in which r-GO and Pt served as electron extractors and triggered the reduction reactions.[314]

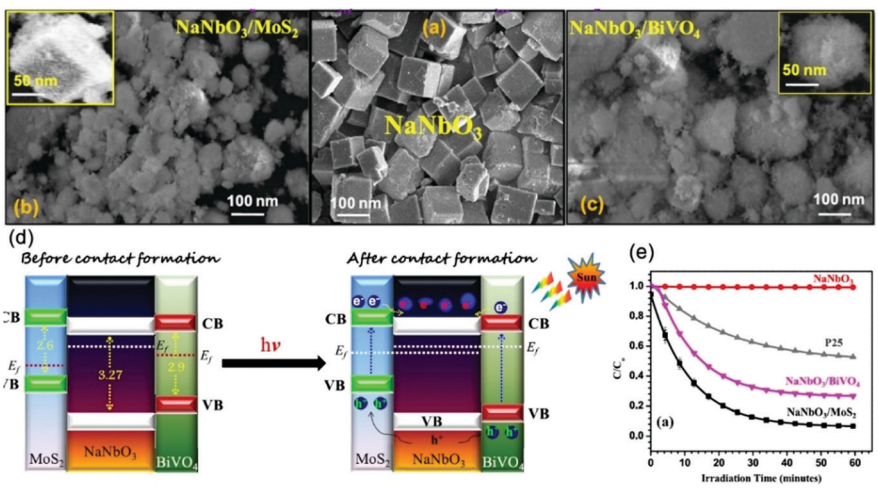


Fig. 11 FESEM images of (a) bare $NaNbO_3$, (b) $NaNbO_3/MoS_2$ and (c) $NaNbO_3/BiVO_4$ composite nanostructures; (d) Schematic band alignment between $NaNbO_3/MoS_2$ and $NaNbO_3/BiVO_4$ nanomaterials (E_f: Fermi level); (e) photocatalytic activity of bare $NaNbO_3$, Degussa (Evonik) P25, $NaNbO_3/BiVO_4$ and $NaNbO_3/MoS_2$ core–shell heterostructures. Reproduced with permission.[319] Copyright 2019, American Chemical Society.

 This journal is © The Royal Society of Chemistry 2021

This ternary heterojunction exhibited 9-fold higher activity than the pristine $NaNbO_3$ and the quantum efficiency reached 5.1%.

4.3.3 Other Nb-based perovskites. Different from the alkaline niobates, $AgNbO_3$ has a smaller bandgap (2.8 eV) and is deemed as a prospective visible-light-sensitive photocatalyst, but fast charge annihilation and relatively low reducing power restrict its application.[322] Kato *et al.* first reported that $AgNO_3$ could be used for water oxidation under visible light,[322] then Ye *et al.* improved its activity by forming solid solutions with other perovskites, such as $NaNbO_3$ or $SrTiO_3$.[91] Later, $AgNbO_3$ nanocubes exposing the high energy (100) facet were hydrothermally prepared, and showed enhanced activity.[323] To further hinder the charge recombination, AgCl, AgBr and g-C_3N_4 were added to $AgNbO_3$.[324–326] Co-catalysts, such as NiO and plasmonic metallic particles, such as Ag were also loaded on $AgNbO_3$ to gain higher activity and more light absorption.[327]

$SrNb_2O_6$ and $Sr_2Nb_2O_7$ have also been reported as promising candidates for photocatalytic water splitting because of the high energy Nb 4d orbitals, which are beneficial for H_2 production and the specific layered structure with the chains of corner-shared distortable NbO_6 octahedrons.[328–330] Ye *et al.* hydrothermally synthesised 1D monoclinic $SrNb_2O_6$ nanorods and orthorhombic $Sr_2Nb_2O_7$ nanoribbons and both showed UV-light driven water splitting.[329] Cho *et al.* prepared single-crystalline $SrNb_2O_6$ nanotubes and demonstrated increased optical absorption,[330] claiming this was due to the longer Nb–O bond in the 1D nanostructure, resulting in a smaller bandgap. The large surface area of the nanotubes was also responsible for the superior photocatalytic evolution of H_2. Pang *et al.* discovered that the anisotropic structure of the $SrNb_2O_6$ nanorods contributed to the charge separation.[331] Quantum confinement in the 1D materials had electrons moving preferentially along the rods and thus reduction reactions primarily occurred at the top planes of the rods, while the holes on the side planes of the rods initiated oxidation reactions. Therefore, the selectivity of water oxidation at the side planes and the CO_2 reduction at the top planes were detected.

Besides 1D nanostructures, layered perovskites, in particular the DJ and RP phases, are a diverse source of nanosheets with molecular thickness. The anisotropic feature of nanosheets is considered to be useful for photocatalytic applications, in that the nanoscale thickness allows for prompt migration of the photogenerated charges to the surface. $KCa_2Nb_3O_{10}$ is a typical DJ perovskite. It consists of $(Ca_2Nb_3O_{10})^-$ perovskite slabs with K^+ embedded in between.[332] To improve the visible-light-driven photocatalytic activity, N-doped $KCa_2Nb_3O_{10}$ nanosheets with a reduced bandgap were fabricated.[333,334] Intercalation of active compounds into the perovskite interlayers contributes to the high photoactivity, because the nanospaces of the interlayers in the layered perovskites give access to the highly active sites. RuO_2 and $Rh(OH)_3$ nanoparticles were first intercalated into the $KCa_2Nb_3O_{10}$ to enhance H_2 evolution rate,[335,336] but the introduction of these rare elements is not commercially preferred. Oshima *et al.* demonstrated a simple solution-based method to decollate the layered nanospaces of $KCa_2Nb_3O_{10}$ with 1 nm Pt nanoclusters by the assistance of tetra(*n*-butyl)ammonium cations.[337] Such nanostructures displayed high stability in photocatalytic water splitting for more than 30 h, and the total H_2 and O_2 evolution was 19.7 μmol h^{-1}. Ongoing investigations to develop active compounds consisting of earth abundant elements for intercalation are required.

$Ba_5Nb_4O_{15}$ is an alternative photocatalyst for water splitting with the {111} type layered perovskite structure, but the wide bandgap (~3.85 eV) endows $Ba_5Nb_4O_{15}$ with merely UV activity.[338] By loading the co-catalyst NiO, $Ba_5Nb_4O_{10}$ split water under UV irradiation with the H_2 evolution rate of 4.8 mmol g^{-1} h^{-1}.[338] Strategies for enhancing visible-light photocatalytic activity include co-doping (the bandgap of the P/Mo co-doped $Ba_5Nb_4O_{15}$ was 2.31 eV) and heterojunction construction (H_2 evolution rate was 2.67 mmol g^{-1} h^{-1}).[339,340]

4.4. Other oxide perovskite photocatalysts

In addition to the previously discussed perovskites, there are a number of perovskite oxides that have shown promising photocatalytic activities. These are discussed below and summarized in Table S4 (ESI†).

4.4.1 Bi_2WO_6. Bi_2WO_6 is the simplest member in the AL perovskite series with an extraordinary layered structure constructed by $(WO_4)^{2-}$ perovskite slabs sandwiched between the $(Bi_2O_2)^{2+}$ rock-salt layers.[341] The bandgap of Bi_2WO_6 is about 2.8 eV, and the CB is constituted of W 6d orbitals while the VB is formed by the hybridization of Bi 6s and O 2p orbitals, which is largely delocalized and thus contributes to the mobility of photogenerated holes.[342] Therefore, the particular layered structure of Bi_2WO_6 benefits the charge separation. The VBM of Bi_2WO_6 is ~+3.2 V *vs.* SHE, indicating a strong oxidation capacity, and thus Bi_2WO_6 is chosen as a model photocatalyst for pollutant degradation and oxygen generation from water splitting, whereas the relatively positive CBM (~+0.5 V *vs.* SHE) limits its application.[233,343,344] There are numerous reports pertaining to the synthesis of Bi_2WO_6-based photocatalysts (Table S4, ESI†), demonstrating that controlling the morphology is a key factor to tune its electronic structure.[341] Various nanostructured Bi_2WO_6 materials, including 1D (nanofibers, nanotubes), 2D (nanosheets, nanoplates) and 3D (flower-like, hollow spheres) structures have been prepared by different methods including hydrothermal, solvothermal, molten salt and sol–gel, with many displaying interesting photocatalytic performances.[345–353] Notably, compared with the 1D and 3D structure, 2D Bi_2WO_6 was deemed to perform better photocatalytically due to geometric factors.[341,353,354] Liu *et al.* showed that photocatalytic CO_2 reduction was largely increased on the surface of the cetyltrimethylammonium bromide modified Bi_2WO_6 nanosheets due to the short diffusion distance and the selective adsorption of CO_2.[353] A Bi_2WO_6 2D array was also built as the photoanode for photoelectrochemical water splitting, on which a much higher photocurrent density and increased photon-to-H_2 conversion efficiency were detected.[355] Intriguingly, the 2D Bi_2WO_6 nanostructure could serve as a support for the intercalation of active compounds. Yi *et al.* synthesised 2D Bi_2WO_6 nanostructures and anchored the hemin on their surface to form hemin-bismuth tungstate nanocomposites *via* a

facile one step hydrothermal method.[354] The enhanced light absorption and the faster electron and oxygen transfer resulting from the 2D structure and the assistance of hemin boosted the photocatalytic performance for tetracycline removal from water under illumination.

To increase the light absorption and improve charge separation, doping is utilized to control the defect levels and modulate the band structure. A series of elements, including Zn, Fe, Ln, F and N, were doped into Bi_2WO_6 for the creation of visible-light-driven photocatalysts.[356–361] Loading plasmonic metal particles on Bi_2WO_6 was also an effective route to boost the photocatalytic performance.[362–364] Wang *et al.* developed an intriguing method to control the oxygen vacancies in Bi_2WO_6 nanosheets through a reduction reaction following the hydrothermal synthesis.[365] By depositing Bi metal particles on the oxygen-vacancy-rich Bi_2WO_6 nanosheets, these nanocomposites exhibited remarkably enhanced activity for selective oxidation of aromatic alcohols to carbonyl compounds in aqueous medium under visible-light irradiation. The synergetic effect of Bi particles and oxygen vacancies was considered to be the major factor for such an improvement, where the oxygen vacancies narrowed the bandgap and improved reactant adsorption while the Bi particles improved light harvesting and provided more active sites. Oxygen vacancies can be introduced by forming heterojunctions. Cao *et al.* reported a novel Bi_2WO_6/amorphous BiOCl heterojunction (Fig. 12a),[366] where abundant WO_{6-x} units were generated due to the rich crystalline-amorphous boundaries. These units facilitate charge separation by capturing electrons hence the heterojunction showed remarkable enhancement in photocatalytic toluene oxidation, with a conversion rate 166 times higher than that of the pristine Bi_2WO_6.

The formation of Bi_2WO_6-based heterojunction has been extensively used to elevate photocatalytic activity for pollutant degradation. A 2D/2D p-$La_2Ti_2O_7$/n-Bi_2WO_6 heterojunction showed excellent photocatalytic performance for RhB degradation due to substantial contact between the 2D components and the formation of a p–n junction that accelerates the electron transfer.[251] Hu *et al.* integrated the ultrathin Bi_2WO_6 nanosheets with black phosphorus and showed that the NO removal ratio was increased 2.6 times that of the pure Bi_2WO_6 nanosheets (Fig. 12b).[367] Zhou *et al.* established a WO_3/Bi_2WO_6 Z-scheme system with Ag particles as light sensitizers.[344] The surface plasmon resonance induced by the Ag particles and the efficient Z-scheme mechanism for charge transfer were considered key to the high photoactivity of this photocatalyst. Other heterojunctions such as $Bi_2Fe_4O_9$/Bi_2WO_6, WO_3/Cu/Bi_2WO_6, $NaBiO_3$/Bi_2WO_6, TiO_2/Bi_2WO_6, MXenes/Bi_2WO_6 have also been constructed for diverse photocatalytic reactions.[343,368–371]

4.4.2 Bi_2MoO_6. Bi_2MoO_6 possesses an AL perovskite layered structure similar to Bi_2WO_6, composed of the $(Bi_2O_2)^{2+}$ layers linking with the corner-shared $(MoO_6)^{2-}$ slabs.[372] According to DFT calculations, the VB of Bi_2MoO_6 is primarily constituted by the O 2p orbitals and its CB consists of mainly the Mo 4d orbitals in the MoO_6 octahedra with contribution from the Bi 6p orbitals in the $(Bi_2O_2)^{2+}$ layers. Therefore, the photo absorption and the charge transfer are sensitive to the composition and the length of the Mo–O and Bi–O bonds. Due to the wider bandgap of Bi_2MoO_6 than that of Bi_2WO_6, the photoactivity of Bi_2MoO_6 generally is not as good as Bi_2WO_6, but since the CBM of Bi_2MoO_6 is −0.32 V *vs.* SHE, H_2 production can be observed even for unmodified Bi_2MoO_6.[373] Many strategies have been developed for improving its photocatalytic activity. Analogous to Bi_2WO_6, morphology control is one of the most usual strategies to tune the electronic structure and optical properties of Bi_2MoO_6, and a variety of Bi_2MoO_6 nanostructures have been synthesised.[374–379] In particular, Xie *et al.* prepared the Bi_2MoO_6 nanosheets with the thickness of a few nanometres *via* a hydrothermal route. Due to the reduction of the diffusion distance of the charge carriers and the exclusion of any grain boundaries and interfaces in the nanosheets, the recombination rate was greatly suppressed.[377] Defect engineering, especially the introduction of oxygen vacancies, has also been investigated. Since the Bi–O bonding interaction is not strong, oxygen vacancies can be readily formed in an environment lacking oxygen.[380] By precise control of the amount of oxygen vacancies, the bandgap of Bi_2MoO_6 can be tailored.[381] These defect states can

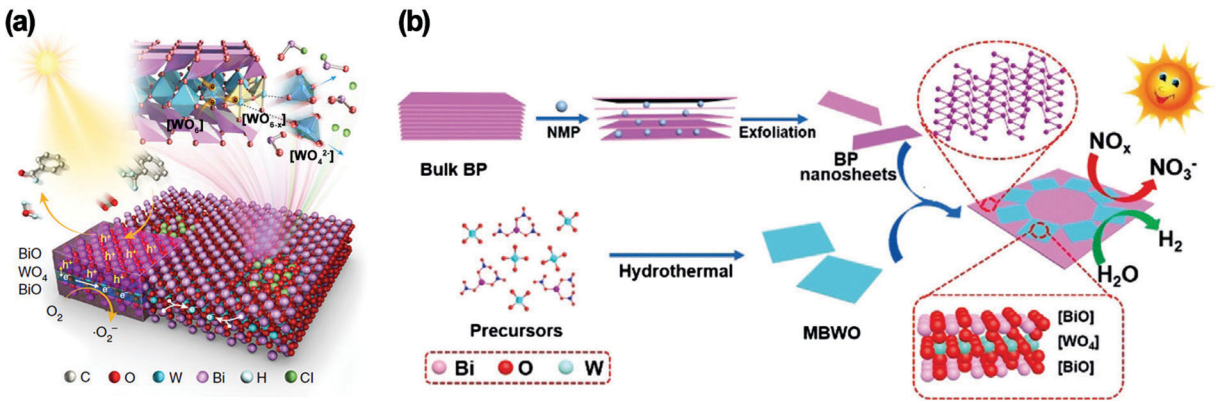


Fig. 12 (a) Schematic illustration of the photocatalytic mechanism of Bi_2WO_6/amorphous BiOCl. Reproduced with permission.[366] Copyright 2018, Nature Publishing Group. (b) Schematic fabrication of the black phosphorus (BP)/monolayer Bi_2WO_6 (MBWO) heterojunction. Reproduced with permission.[367] Copyright 2019, Wiley-VCH Verlag GmbH & Co. KGaA, Weinheim.

 This journal is © The Royal Society of Chemistry 2021

also trap charge carriers, improving the separation of photo-generated electron–hole pairs.[381] More importantly, oxygen vacancies can serve as the electron donors to enhance the adsorption and the activation of the reactant molecules.[382] Fu *et al.* deposited Fe_2O_3 clusters on the Bi_2MoO_6 with rich oxygen vacancies and unveiled a new path of electron transfer from oxygen vacancies to Fe_2O_3 clusters, by which charge separation and the photocatalytic activity were increased (Fig. 13).[383] Jing *et al.* produced Bi_2MoO_6 hierarchical balls with abundant oxygen vacancies, which were then used as the photocatalysts for the selective oxidation of benzyl alcohol under visible light.[382] Doping is another effective strategy for defect engineering. Many foreign elements have been introduced in to Bi_2MoO_6 to generate controllable defects and improvement in photocatalytic efficiency is achieved in those defect-rich samples on account of the extension of light absorption and the acceleration in electron–hole pair separation.[384–386]

Meanwhile, a variety of Bi_2MoO_6-based heterojunctions, such as Bi_2MoO_6/AgX (X = Cl, Br, I),[387,388] Bi_2MoO_6/Ag_2O,[389] Bi_2MoO_6/Ag_3XO_4 (X = P, V),[390,391] Bi_2MoO_6/g-C_3N_4,[392] Bi_2MoO_6/TiO_2,[393] and Bi_2MoO_6/MOFs,[394] were developed and showed strong optical absorption and excellent photocatalytic activity. In addition, a solid-state Z-scheme system of Bi_2MoO_6/CdS with Bi metal particles as electron mediators was formed.[395] In this system, due to the dual role of the Bi particles – electron mediators and the source of SPR – the H_2 evolution rate was enhanced, but substitution of the toxic CdS by other narrow bandgap semiconductors should be considered for sustainable catalyst production. Taking advantage of the stronger redox ability under visible light, more Z-scheme systems were established recently, such as $Ag_3PO_4/Ag/Bi_2MoO_6$ and AgI/Bi_2MoO_6.[396,397] Light sensitizers (Ag, Au, Bi, *etc.*) were also deposited on Bi_2MoO_6 and the photocatalytic performance was found to be elevated in many different reactions.[395,398,399]

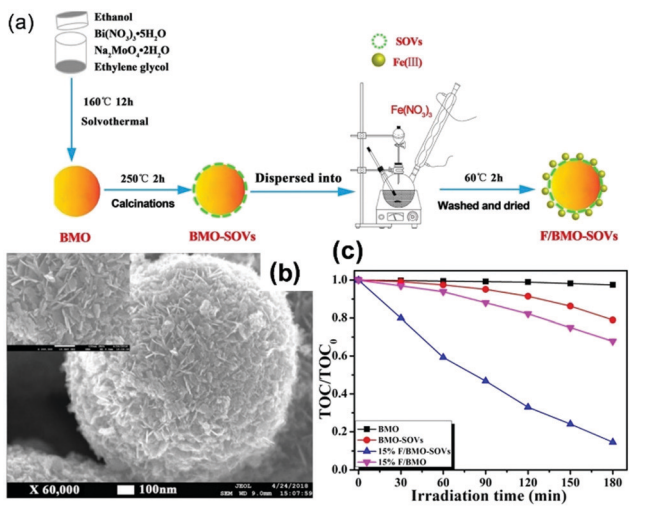


Fig. 13 (a) Schematic illustration of the preparation process of Fe_2O_3/Bi_2MoO_6 with surface oxygen vacancies (F/BMO-SOVs); (b) FESEM images of the F/BMO-SOVs nanocomposites, the inset scale bar is 100 nm; (c) total organic carbon (TOC) removal of phenol by BMO, BMO-SOVs, F/BMO-SOVs and F/BMO under visible light illumination. Reproduced with permission.[383] Copyright 2019, Elsevier.

4.4.3 $ASnO_3$. Alkaline earth stannates, $ASnO_3$ (A = Ca, Sr, Ba), have been extensively investigated due to their wide application in ceramic dielectric bodies, gas-sensitive materials, ferromagnetic materials and anode materials for lithium ion batteries.[400–402] Because the 3D network of the corner-shared SnO_6 octahedra are able to facilitate the electron transfer, and the dipole moment induced by the distortion of the SnO_6 units benefits the charge separation, $ASnO_3$ has already been used as a photocatalyst in various photocatalytic reactions (Table S4, ESI†). Among the $ASnO_3$ materials, $CaSnO_3$ have the highest activity in photocatalytic degradation, which was attributed to the small radius and the largest electronegativity of the Ca^{2+} ions that elongated the Sn–O bonds and distorted the SnO_6 octahedra.[403,404] Moshtaghi *et al.* described a facile and green co-precipitation method for the synthesis of $CaSnO_3$ nanocubes, which showed good activity in azo dye degradation under UV light.[405]

Despite the mild distortion of SnO_6 units, the orthorhombic $SrSnO_3$ nanoparticles prepared by solution-based methods under relatively low temperature exhibit more attractive photocatalytic properties due to their anisotropic nature.[406] Furthermore, the VBM of $SrSnO_3$ is +2.69 V *vs.* SHE and the CBM is −1.37 V *vs.* SHE.[407] Such band edge positions make $SrSnO_3$ a well-suited material for many photocatalytic reactions, especially water splitting, under UV irradiation. Alammar *et al.* synthesised a series of $SrSnO_3$ nanorods and nanoparticles in different ionic liquids by microwave heating.[407] All these $SrSnO_3$ nanocrystals had good UV activity after loading with Rh, and the H_2 evolution rates were in the range of 99 to 110 μmol h^{-1}. Peanut-shaped $SrSnO_3$ nanoparticles were also obtained by co-precipitation and annealing, and the H_2 evolution rate under UV light was 236.5 μmol g^{-1} h^{-1} with NiO_x as co-catalyst.[408] Moreover, active facets play an important role in the photocatalytic performance of $SrSnO_3$ nanorods. The $SrSnO_3$ nanorods that only exposed {001} facets had the best activity and stability (Fig. 14).[409] To increase the light absorption, Zhang *et al.* synthesised N-doped $SrSnO_3$ nanorods by a facile *in situ* heat treatment method. The incorporation of nitrogen extended the light absorption to the visible region because of the formation of the in-gap states resulting from the mixture of the N 2p and O 2p orbitals. This improved the photocatalytic degradation from 20.10% (undoped samples) to 91.29% (N-doped $SrSnO_3$ nanorods).[410]

Compared to $CaSnO_3$ and $SrSnO_3$, $BaSnO_3$ possesses the standard SnO_6 octahedra and the smallest bandgap (~3.1 eV).[411] Due to the position of the CBM (−0.69 V *vs.* SHE), $BaSnO_3$ can serve as a candidate for photocatalytic water splitting. Nevertheless, the wide bandgap and the fast recombination rate lead to poor efficiency. Defect engineering was proposed to introduce oxygen vacancies into the $BaSnO_3$ nanocrystals in a controllable way to reduce the bandgap and produce more active sites. Ion substitution, such as doping Sb and Fe in the B-site, or La in the A-site, is the most common technique to generate oxygen vacancies, but the generated oxygen vacancies will distribute randomly in bulk and on the surface.[412–414]

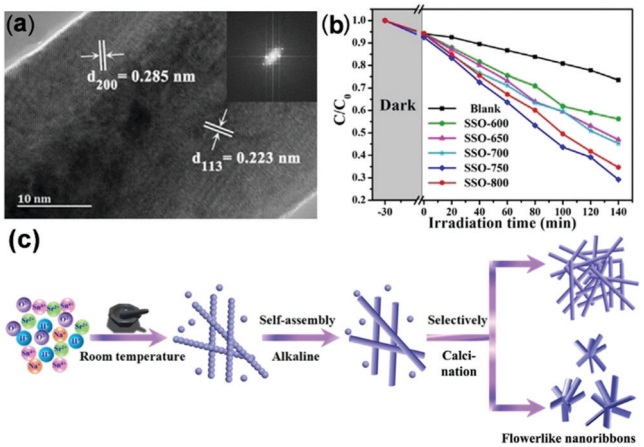


Fig. 14 (a) HRTEM image of $SrSnO_3$; (b) degradation activities of samples synthesised at different temperatures (SSO-calcination temperature); and (c) schematic representation for the synthesis of the $SrSnO_3$ microstructures. Reproduced with permission.[409] Copyright 2019, Wiley-VCH Verlag GmbH & Co. KGaA, Weinheim.

Kim *et al.* developed an effective chemical reduction method by using $NaBH_4$ to introduce oxygen vacancies into $BaSnO_3$ in a controlled way to gain more surface active sites.[415] By optimizing the oxygen vacancy level, the bandgap was reduced to 2.17 eV with excellent photocatalytic activity for the water splitting reaction. The formation of a solid solution is another way to increase the photocatalytic performance. Currently, the microwave-assisted ionic liquid method allows the formation of a homogeneous $SrSnO_3$–$BaSnO_3$ solid solution at low temperature over a short period.[407,416] Although the octahedral tilting distortion increased with Sr content, which contributed to the charge separation, the Ba content in the solid solution was beneficial for the surface area, thus optimized performance was from the $Sr_{0.8}Ba_{0.2}SnO_3$ sample.[416]

4.4.4 $BaZrO_3$. Barium zirconate, $BaZrO_3$, is a typical cubic perovskite oxide with a Zr–O–Zr bond angle of 180°, which is beneficial for the delocalization of the photogenerated carriers, thereby transferring charges to initiate redox reaction.[417] Since the VBM of $BaZrO_3$ (O 2p orbitals) is situated at about +3.0 V *vs.* SHE and the CBM (Zr 4d orbitals) is located at around −1.8 V *vs.* SHE, $BaZrO_3$ is considered as a promising photocatalyst for water splitting.[418] Many efforts have since focused on improving its photocatalytic activity by doping, forming solid solution, constructing heterojunctions and morphology control. Chen *et al.* synthesised the hollow $BaZrO_3$ nanocrystals *via* a facile solvothermal method using ethylenediamine as solvent.[419] The large surface area and the large amount of surface oxygen vacancies of these hollow $BaZrO_3$ nanocrystals gave a H_2 evolution rate of 67.98 μmol g^{-1} h^{-1}, 14.8 times higher than the commercial $BaZrO_3$. The photoactivity of different facets were also compared through morphology control. The polyhedral $BaZrO_3$ dominated with {001} and {110} facets exhibited 9.4 times higher photocatalytic activity than the $BaZrO_3$ nanoparticles enclosed primarily by {110} facets.[420] According to DFT calculations, the CB of the samples exposing {001} facets was about 0.31 V more negative than those with only {110} facets, and thus the high reduction energy stemming from the {001} facets was responsible for the high activity. It is worth noting that the absorption threshold of $BaZrO_3$ is in the UV region of the light spectrum. To enhance the visible-light activity of $BaZrO_3$, attempts have been made to modify its band positions by incorporating dopants (*e.g.*, Bi, Ce, Fe and Sn) and creating oxygen vacancies in the lattice.[418,421–423]

4.4.5 Other oxide perovskites. There are numerous reports on other earth-abundant nontoxic perovskite oxides active for photocatalytic degradation and water splitting, such as $LaCoO_3$, $LaNiO_3$, $LaMnO_3$ and their doped counterparts (Table S4, ESI†).[424–428] Of these perovskites, the AL layered perovskite $Bi_4V_2O_{11}$ has attracted attention due to its particular structure, narrow bandgap and intense ferroelectricity. $Bi_4V_2O_{11}$ can be expressed as $[(Bi_2O_2)(VO_{3.5}\square_{0.5})]_2$ (where □ stands for oxygen vacancy), and in general it is considered to be composed of alternate layers of the $(Bi_2O_2)^{2+}$ rock-salt layers and the $(VO_{3.5}\square_{0.5})$ perovskite slabs.[429] Although the bandgap of $Bi_4V_2O_{11}$ is in the regime of visible light (~2.2 to 2.4 eV), the inefficient charge transfer and the fast recombination due to the existence of many oxygen vacancies hinder it from being used as a sole photocatalyst.[430] Therefore, many studies concentrate on the fabrication of $Bi_4V_2O_{11}$-based heterojunctions. For example, a 1D Bi_2O_3–$Bi_4V_2O_{11}$ type II heterojunction showed enhanced photocatalytic degradation, ascribed to anisotropic charge transport and efficient charge separation induced by the 1D heterostructure.[431] The Z-scheme heterojunction AgI–$Bi_4V_2O_{11}$ showed visible-light photocatalytic activities for degradation of sulfonamide antibiotics.[432] Other heterostructures, such as Bi_2MoO_6–$Bi_4V_2O_{11}$, Bi_2WO_6–$Bi_4V_2O_{11}$, Bi QDs–$Bi_4V_2O_{11}$, $BiVO_4$–$Bi_4V_2O_{11}$ and dye-sensitized TiO_2–$Bi_4V_2O_{11}$ have been reported with improved photocatalytic pollutant degradation.[433–437] More importantly, since oxygen vacancies can trap electrons in the metastable states, these electrons may be able to inject into an antibonding orbital of adsorbed N_2, thereby weakening the N–N triple bond for subsequent activation.[438] Therefore, $Bi_4V_2O_{11}$ may be a potential photocatalyst for nitrogen fixation.[439] Noting that $BiVO_4$, a well-documented photocatalyst with high efficiency in water splitting and pollutant degradation, is an intermediate of the synthesis of $Bi_4V_2O_{11}$ bulk samples when increasing temperature,[440] indicating small quantities of $Bi_4V_2O_{11}$ could be present in the $BiVO_4$ samples as it is thermodynamic stable. Investigations indicate that the existence of $Bi_4V_2O_{11}$ in the $BiVO_4$ nanocrystals had positive effects on the photocatalytic activity,[435,441] and a recent study illustrated that the presence of the $Bi_4V_2O_{11}$ nanoregions in ultrathin $BiVO_4$ produce intensive photovoltaic voltage and current due to the synergy of charge separation in the $Bi_4V_2O_{11}$ regions and the light absorption ability in the $BiVO_4$ region.[442] Such advances are expected to be applied in the field of photocatalytic degradation and water splitting in the future.

4.5. Halide perovskites

Most photocatalysts based on perovskite oxides harvest very little visible light due to their wide bandgap. This is primarily

 This journal is © The Royal Society of Chemistry 2021

attributed to the dominant contribution of O-2p orbitals to the density of states (DOS) around the VBM of perovskite oxides, which basically fix their VBM levels at around +3.0 V *vs.* SHE.[443] The perovskite oxides that do have visible light activity (E_g < 3.0 eV) possess a CBM that is lower than the potential of H_2/H^+, O_2/O_2^- and CO_2/CO. Hence in the last decade researchers have investigated non-oxide perovskites, such as halide perovskites, that demonstrate impressive optoelectronic properties.[150,444,445] The general formula of halide perovskites is ABX_3, in which A is a monovalent cation, such as MA, FA, Cs^+, or Rb^+; B represents divalent metal ions, which can be Pb^{2+} or Sn^{2+}; and X is a halogen ions (Cl^-, Br^- and I^-). Halide perovskites feature low synthesis cost, widely tuneable bandgap, long carrier lifetime and diffusion distances, large absorption coefficient and good charge mobility, making them attractive candidates for application in solar cells, LEDs, lasers and photodetectors.[446–452] In particular, the power conversion efficiency of the halide perovskite solar cells has recently reached 25.2%,[453] indicating that both the light absorption and energy conversion of these compounds are highly efficient. This success has inspired the study of halide perovskites in solar-to-chemical energy conversion and environment remediation.

Halide perovskites embody numerous desirable advantages for photocatalysis, such as narrow bandgap, slow electron–hole recombination and fast charge carrier transport.[454–458] In addition, most of the halide perovskites exhibit excellent reduction ability, that is, their CBM is usually more negative than the potential of H_2/H^+, O_2/O_2^- and CO_2/CO due to the more negative potential of the p-orbitals (*e.g.*, X-3p) compared to O-2p in the perovskite oxides, enabling them to trigger H_2 evolution, superoxide radical generation and CO_2 reduction.[150,444] Nevertheless, several constraints limit the application of halide perovskites in photocatalytic systems. First, the VBM of some halide perovskites is too negative to oxidize the water molecules or produce OH radicals, thereby making these perovskites unsuitable for water oxidation and pollutant degradation.[150,444] Second, the instability of most of the halide perovskites hinders their photocatalytic utility.[150,444,445] Third, most of the commonly used halide perovskites contain lead, hence toxicity remains the primary concern for large-scale applications.[459]

To produce environmentally friendly and stable halide perovskites as photocatalysts, lead-free halide perovskites are developed.[155,460–462] Among them, tin-, bismuth- and antimony-based halide perovskites have shown good resistance to humidity, oxygen and illumination, and outstanding activities in many photocatalytic reactions, and thus they have been extensively used in H_2 generation, CO_2 reduction and pollutant degradation (Table S5, ESI†).

4.5.1 Sn-based halide perovskites. Sn-based halide perovskites are preferred over the Pb-based halides that are widely used in perovskite-based solar cells and photocatalysis due to the low toxicity of Sn^{2+}.[463–465] Reyes-Perez *et al.* prepared $CsSnBr_3$ for the photocatalytic degradation of violet blue in water and showed a good adsorption rate to the dye molecules: the adsorption rate was positively related to the efficiency of photocatalytic degradation.[466] Nevertheless, both +2 and +4 oxidation states for Sn were confirmed in the crystal lattice, and adsorbed oxygen was observed at the crystal surface as well, resulting in low crystallinity at the surficial region, which might affect the photocatalytic performance of the $CsSnBr_3$ particles. Hong *et al.* synthesized a 2D Sn-based halide perovskite by intercalating 1-hexadecylammonium (HDA) cations between the inorganic layers and studied its photocatalytic dehydrogenation activity. The instability of Sn(II), however, impaired the product yields.[159] To enhance the stability, Ju *et al.* used $CH_3NH_2CH_3^+$ (DMA) as the A site ion and synthesised $DMASnI_3$ for photocatalytic water splitting.[467] Interestingly, while the fresh $DMASnI_3$ was yellow rod-like crystals, it turned black when exposed to air because the generated iodide defects reduced the bandgap. Despite the formation of iodide defects, the as-obtained $DMASnI_3$ crystals remained stable even when immersed in water for 16 h. Therefore, these crystals could be applied to photocatalytic water splitting in pure water, rather than in the saturated halo acid solution. The H_2 evolution rate was 0.64 μmol h^{-1} with good recycling stability, but SnI_4 was found after the H_2 evolution due to the formation of oxygen.

The stability and charge separation can be improved by forming a heterojunction. Zhang *et al.* obtained a $MASnI_3$/TiO_2 p–n heterojunction by a wet chemical process, and studied the photoactivity using the degradation of RhB in water under visible light.[468] Compared with the $MASnI_3$ and TiO_2 samples, the $MASnI_3/TiO_2$ heterojunction exhibited the fastest reaction rate. More importantly, no oxidation state +4 Sn was detected after the degradation, indicating that the combination of the two components contributed to the stability of the samples. The enhanced stability of the heterojunction was attributed to the superoxide radicals being generated on the n-type TiO_2 rather than on the p-type $MASnI_3$. That is, aqueous oxygen would only acquire electrons on TiO_2 (which were transferred from photoexcited $MASnI_3$) instead of oxidizing the Sn(II) to Sn(IV) on $MASnI_3$.

Sn-based halide perovskite heterojunctions have also been employed in solar-to-chemical fuel conversion. Wang *et al.* synthesised a Cs_2SnI_6/SnS_2 hybrid by mixing a CsI ethanol solution with SnS_2 nanosheets (Fig. 15a).[469] Here, Cs_2SnI_6 possesses a derivative structure from the rock-salt double perovskite ($A_2BB'X_6$) in which the B′ ions are taken away, and thus all the SnX_6 octahedra in the crystal lattice are isolated.[470] As the oxidation state for Sn in this halide perovskite was +4, this compound was more stable than Sn-based halide perovskites containing +2 Sn. Owing to the outstanding stability of Cs_2SnI_6 and the pronounced charge separation ability attributed to the type II heterojunction (Fig. 15c), the optimized Cs_2SnI_6/SnS_2 structure showed a 5.4-fold enhancement in the methane rate compared with the original SnS_2 nanosheets (Fig. 15b).

4.5.2 Bi-based halide perovskites. Although Sn-based halide perovskites have been studied in photovoltaics and photocatalysis, the instability of the Sn ions is the main obstacle for their practical use. Bi-based halide perovskites, having outstanding stability and superior optoelectronic properties, have gained attention as alternatives in photovoltaic and

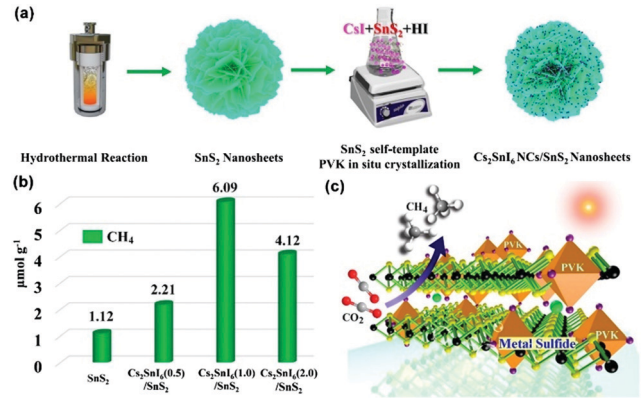


Fig. 15 (a) Schematic illustrating the synthesis procedure for the Cs_2SnI_6/SnS_2 heterojunction (PVK denotes halide perovskites). (b) The methane production rate of different samples. (c) Scheme of photocatalytic CO_2 reduction on the Cs_2SnI_6/SnS_2 heterojunction. Reproduced with permission.[469] Copyright 2019, American Chemical Society.

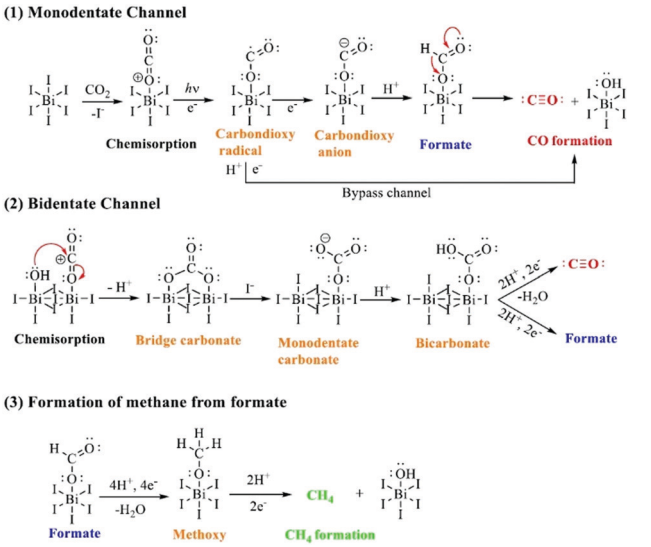


Fig. 16 Plausible mechanisms of photocatalytic CO_2 reduction *via* $Rb_3Bi_2I_9$ and $Cs_3Bi_2I_9$ catalysts. Reproduced with permission.[474] Copyright 2019, American Chemical Society.

photocatalytic applications.[463,464,471] Note that the use of Bi ions does not result in charge neutrality of ABX_3, and therefore structural variants rather than the typical ABX_3-type perovskites are prevalent in the Bi-based halide perovskites. Guo *et al.* synthesised $MA_3Bi_2I_9$ particles *via* the co-precipitation of MAI and BiI_3 in a HI and H_3PO_2 solution.[472] The structure of $MA_3Bi_2I_9$ can be depicted as a defective ABX_3 structure, in which the Bi ions residing at the BiI_6 octahedra along the space diagonal in a perfect ABX_3 crystal lattice are removed.[473] This compound displayed photocatalytic water splitting activity under visible light in a saturated HI solution. Besides water splitting, $MA_3Bi_2I_9$, as well as $Rb_3Bi_2I_9$ and $Cs_3Bi_2I_9$ were used in visible light driven CO_2 reduction.[474] Intriguingly, $Rb_3Bi_2I_9$ had the highest yield of methane production, while $Cs_3Bi_2I_9$ exhibited the highest CO production rate as well as the best photocatalytic activity. Detailed investigations of the reaction mechanism pinpoint that when using $Rb_3Bi_2I_9$ as photocatalyst, monodentate CO_2 adsorption was preferred (Fig. 16(1)) and formate was the most important intermediate for the formation of methane, whereas with respect to $Cs_3Bi_2I_9$, bidentate CO_2 interaction was of higher priority (Fig. 16(2)), and when the reaction went through monodentate adsorption the CO formation occurred directly from the carbondioxy radical (Fig. 16(1), bypass channel) due to its excellent electron mobility, and therefore the yield of CO was high. Based on these studies, halide perovskites can be designed for selective production of various fuel gases. A Z-scheme system was developed to improve the CO_2 reduction efficiency. Liu *et al.* combined $Cs_3Bi_2I_9$ with Bi_2WO_6 to form a direct Z-scheme heterojunction. The efficient charge transfer ability derived from the sharing of the Bi ions at the interfaces, as well as the preserved redox ability by the Z-scheme structure, significantly improved the production of CO.[475] Aside from CO_2 reduction, $Cs_3Bi_2I_9$ is also active in photocatalytic H_2 generation and pollutant degradation.[476–478]

$Cs_3Bi_2Br_9$ possesses good stability and recyclability, and has been widely applied for photocatalytic organic synthesis. Dai *et al.* demonstrated the visible-light activity of $Cs_3Bi_2Br_9$ for the ring-opening reactions of epoxides. The high activity and high selectivity ($\geq$86%) of this photocatalyst were ascribed to the Bi-based Lewis acid sites that could coordinate the O atom in the three-membered heterocyclic ring.[479] To further increase the contact between the catalysts and reactants, $Cs_3Bi_2Br_9$ nanoparticles (2–5 nm) were dispersed into the channels of a mesoporous silica, SBA-15.[480] This composite showed visible-light activity for toluene oxidation, with a conversion rate reaching 32 900 μmol g_{cat}^{-1} h^{-1} and high aldehyde and ketone selectivity (>99%).

The Cs_2AgBiX_6 double perovskite is another promising photocatalyst. Compared to $Cs_3Bi_2X_9$ (X = Br and I), Cs_2AgBiX_6 has a substantial absorption coefficient, longer electron–hole recombination lifetime and better stability under illumination and moisture. This is attributed to the silver incorporation that induces structural transformation from the 2D layered structure to a rock-salt double perovskite structure.[481] As the Ag 4d orbitals raise the VBM, Cs_2AgBiX_6 exhibits a narrower bandgap, higher charge carrier mobility and lower exciton binding energy.[482] Thus, Cs_2AgBiX_6 is widely applied to photocatalysis. Zhou *et al.* obtained $Cs_2AgBiBr_6$ nanoparticles *via* a hot injection route, and these nanoparticles demonstrated fair photocatalytic activity in CO_2 reduction.[69] Wu *et al.* synthesised ~4.6 nm Cs_2AgBiI_6 nanoparticles *via* an anti-solvent recrystallization approach, which exhibited a CO yield of 18.9 μmol g^{-1} in photocatalytic CO_2 reduction with 100% selectivity.[483] Zhang *et al.* developed an ethanol-based photocatalytic system, in which $Cs_2AgBiBr_6$ significantly improved the degradation of RhB under visible light.[484] To further boost the electron mobility and promote the charge separation ability of the photocatalysts, r-GO serving as electron mediator was combined with $Cs_2AgBiBr_6$ nanoparticles.[485,486] On account of the superior conductivity of r-GO, photoelectrons could be rapidly extracted from $Cs_2AgBiBr_6$ and transferred into r-GO, facilitating

 This journal is © The Royal Society of Chemistry 2021

electron–hole separation and contributing to H_2 evolution and CO_2 reduction.

4.5.3 Sb-based halide perovskites. Similar to the Bi-based halide perovskites, Sb-based halide perovskites have good stability and excellent photovoltaic performance.[463,464,487] As an alternative lead-free halide perovskite, Sb-based halide perovskites have also been employed for photocatalytic application recently. Zhang *et al.* reported $A_3Sb_2Br_9$ (A: Cs or MA) nanoparticles synthesised by an anti-solvent recrystallization method.[488] The effects of the A-site cations (Cs_xMA_{3-x}, x = 0–3) on the photocatalytic activity for hydrocarbon oxidation were carefully investigated. They found that the octahedron distortion induced by the A-site cations played critical roles in photocatalytic efficiency, and $Cs_{2.3}MA_{0.7}Sb_2Br_9$ exhibited the best performance for photocatalytic toluene oxidation. $Cs_3Sb_2I_9$ was also synthesised for CO_2 reduction under visible light.[489] The CO yield of 7.1 μmol g^{-1} with 100% selectivity was ascribed to the low electron–hole recombination rate, efficient charge separation and suitable VBM/CBM positions of this perovskite.

By substituting some Sb^{3+} with Bi^{3+} to form $Cs_3Bi_{2x}Sb_{2-2x}I_9$, the photocatalytic activity of perovskite catalysts could be improved further. Chen *et al.* synthesised $Cs_3Bi_{2x}Sb_{2-2x}I_9$ perovskite, and assessed its photocatalytic activity for hydrogen evolution in a HI solution (Fig. 17).[490] Compared to $Cs_3Bi_2I_9$ and $Cs_3Sb_2I_9$, the Sb^{3+} ions effectively reduced the contribution of Bi^{3+} ions on the CB, thereby reducing population of mid-gap states derived from the Bi vacancies and narrowing the bandgap. During the H_2 evolution, the highly reducing species (I^-) in the reaction solution prevented the oxidation of Sb^{3+} to Sb^{5+}. Cs_2CO_3 was added to decrease the concentration of Bi^{3+} and suppress the Bi^{3+}/Bi side reaction by adjusting the solution equilibrium between Cs^+ and $(Bi_2I_9)^{3-}$. After loading with Pt nanoparticles, $Cs_3Bi_{0.6}Sb_{1.4}I_9$ showed a H_2 evolution rate of 92.6 μmol h^{-1}, significantly higher than that of $Cs_3Bi_2I_9$ under the same condition (~4 μmol h^{-1}).

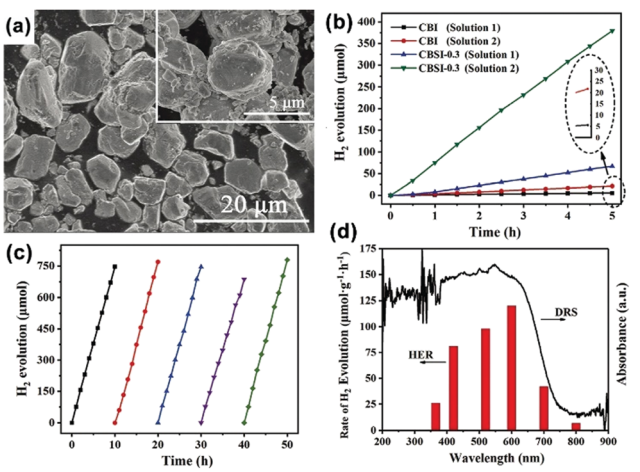


Fig. 17 (a) SEM images of $Cs_3Bi_{2x}Sb_{2-2x}I_9$ (CBSI-x). (b) H_2 evolution rate of $Cs_3Bi_2I_9$ (CBI) and CBSI-0.3 in HI solution (solution 1) and HI solution with Cs_2CO_3 (solution 2). (c) Stability assessment of CBSI-0.3 in Solution 2. (d) H_2 evolution activity (HER) for CBSI-0.3 *versus* wavelength and diffuse reflectance spectrum (DRS) of CBSI-0.3. Reprinted with permission.[490] Copyright 2020, Wiley-VCH Verlag GmbH & Co. KGaA, Weinheim.

4.6. Oxyhalide perovskites

Mixed-anion perovskites, such as perovskite oxynitrides and oxysulfides have been studied as promising photocatalysts with sufficient redox potential, visible-light response, and high photocatalytic stability.[491,492] In these perovskites, the VB is formed *via* the hybridization of non-oxide p-orbitals and O-2p orbitals. Such hybrid VB give these perovskites higher durability against oxidation than non-oxides (*i.e.*, nitrides and sulfides), as well as an elevated VBM that leads to a narrower bandgap than oxides. However, for many mixed-anion compounds, deactivation induced by oxidation is still in competition with the desired photocatalytic reactions. Although some surface modifications, such as co-catalyst loading, have proven effective for suppressing the self-oxidative deactivation to some extent,[493,494] sufficiently high durability at a practical level has not yet been achieved. This unavoidable problem results from the fact that the photogenerated holes are prone to localize at the DOS around the VBM of the non-oxide anions after the energy relaxation, leading to the accumulation of holes on the unstable non-oxide anions, which is followed by self-oxidation (Fig. 18a). In other words, to avoid the self-oxidation, the formation of stable VB structure is necessary (Fig. 18b).

Recently, a series of layered perovskite oxyhalides such as Bi_4MO_8X (M = Nb, Ta, X = Cl, Br) have emerged as promising photocatalysts.[495–497] These compounds fulfil the necessary conditions of photocatalysts, *i.e.*, sufficiently high stability and appropriate band levels for visible-light-induced water splitting, due to their unique VB structures.[495] For example, Bi_4NbO_8Cl belongs to the n = 1 members of the Sillén–Aurivillius perovskite family $[(Bi_2O_2)_2X]^{3+}[A_{n-1}B_nO_{3n+1}]^{3-}$, which is composed of fluorite $[Bi_2O_2]$, perovskite $[NbO_4]$ and halogen [Cl] layers as depicted in Fig. 19a. The electrochemical measurement revealed that the VBM of Bi_4NbO_8Cl is located at a more negative energy level (*ca.* 2.2 V *vs.* SHE) than most oxide perovskites (~3.0 V *vs.*

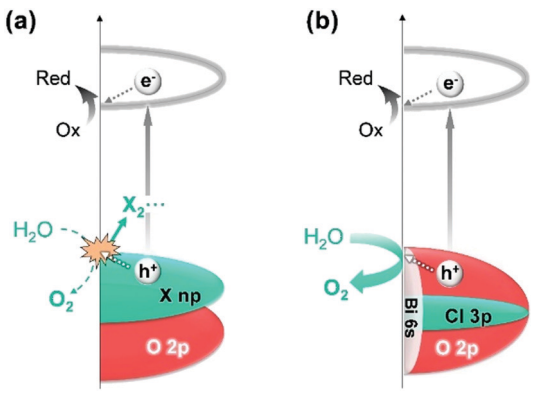


Fig. 18 Schematic VB structures and reaction scheme on (a) conventional mixed-anion compounds (unstable) and (b) Sillén–Aurivillius oxyhalide perovskites such as Bi_4NbO_8Cl (stable). The "Red" and "Ox" denotes H_2/H_2O or reductant/oxidant of redox mediators such as Fe^{2+}/Fe^{3+} and I^-/IO_3^-.

SHE in most cases) or conventional oxychlorides (*e.g.*, BiOCl, ~3.0 V *vs.* SHE). Consequently, Bi_4NbO_8Cl possesses both a narrow bandgap (~2.4 eV) for visible light absorption up to *ca.* 500 nm and a more negative CBM (*ca.* −0.2 V *vs.* SHE) than the water reduction potential.[495] The O_2 evolution activity of Bi_4NbO_8Cl in an aqueous Fe^{3+} (electron acceptor) solution was as high as that of conventional O_2-evolving photocatalysts, such as WO_3, even without any cocatalyst.[495] No change in crystal structure and composition was observed after the photocatalytic reaction, confirming the stability of this material was good. Visible-light-driven Z-scheme water splitting was also demonstrated using the Bi_4NbO_8Cl as an O_2-evolving photocatalyst and the Rh-doped $SrTiO_3$ as a H_2-evolving photocatalyst in the presence of the Fe^{3+}/Fe^{2+} redox mediator (Fig. 19b).[495]

All of the Bi_4MO_8X (M = Nb, Ta, X = Cl, Br) series can function as stable O_2-evolving photocatalysts under visible light without suffering from deactivation by self-oxidation.[495] This distinct feature originates from the unique VB structure (Fig. 18b). Fig. 20a shows the DFT-calculated band structure of Bi_4NbO_8X.[496] As expected from the electronegativities of Br and Cl, the Br-4p orbitals in Bi_4NbO_8Br are located at a higher energy level than the Cl-3p in Bi_4NbO_8Cl. However, the DOS around the VBMs of Bi_4NbO_8X are predominantly composed of O-2p orbitals, in stark contrast to the simple oxyhalides BiOCl and BiOBr, in which Cl-3p and Br-4p orbitals mainly contribute to the DOS near the VBM. These results differ from the conventional understanding that the potentials of the VBM formed by O-2p orbitals are fixed at deeply positive levels of *ca.* +3.0 V *vs.* SHE.[443] However, the DFT calculation on Bi_4NbO_8X (Fig. 20a) indicated that there was an overlap in similar shapes between Bi-6s and O-2p orbitals at a lower energy region from −11 to −7 eV. Additionally, a contribution of Bi-6p orbitals, as well as O-2p and Bi-6s, was seen around the VBM. According to the revised lone pair model proposed by Walsh *et al.*, there is an s–p interaction between $5s^2$ or $6s^2$ electrons of post-transition metals (*e.g.*, Sn, Sb and Bi) and O-2p electrons in oxides such as $BiVO_4$.[498] The bonding and anti-bonding orbitals are formed by the interaction between Bi-6s and O-2p orbitals, and the resultant anti-bonding orbital (of Bi-6s + O-2p) can be concurrently stabilized through the interaction with the unoccupied Bi-6p orbital, leading to an energy level elevation of the original O-2p orbital (Fig. 20b).[496] In addition, Madelung site potential analysis for Bi_4NbO_8Cl indicated that the oxygen sites in Bi_4NbO_8Cl were electrostatically destabilized, which also probably contributed to the elevation of the VBM that mainly consists of O-2p.[499] In other words, the strong hybridization between Bi-6s and O-2p, as well as electrostatic destabilization of oxygen, endows Bi_4NbO_8X with a unique VBM that is composed mainly of O-2p orbitals, but located at more negative potentials compared to conventional oxides and oxyhalides.

These studies on Sillén–Aurivillius oxyhalide perovskite Bi_4NbO_8X provide new strategies for developing stable photocatalysts for visible light-induced water splitting, by manipulating the interaction between s orbitals of post transition metals (*e.g.*, Bi-6s) and O-2p orbitals in the specific crystal structure, *e.g.*, the Sillén–Aurivillius compounds. This strategy has been partially proven by the studies on the oxyhalide perovskites with various layered structures. For example, $Bi_6NbWO_{14}Cl$, which has a different stacking sequence to Bi_4NbO_8Cl, has shown stable O_2 evolution activity under visible light.[500] In addition, it can also be used as an O_2-evolving photocatalyst in a Z-scheme water splitting system.[500] More oxyhalide perovskites in this family with various stacking sequences and perovskite layers (n) were explored. However, the reports on the synthesis of double layered (n = 2) perovskites were limited compared with the single layered ones, probably due to the severe conditions required for their synthesis in the conventional solid state reaction. To solve this problem, a new two-step synthesis method including polymerized complex synthesis was recently developed, in which fine particles of a precursor oxide (*e.g.*, $SrBi_2Ta_2O_9$) were first prepared *via* the polymerized complex method, followed by heating with an oxyhalide (*e.g.*, $SrBiO_2Cl$) to form $Sr_2Bi_3Ta_2O_{11}Cl$.[501] By employing this two-step method, 14 compounds of $A_4A'M_2O_{11}Cl$ (A and A′ = Sr^{2+}, Ba^{2+}, Pb^{2+} and Bi^{3+}; M = Ti^{4+}, Nb^{5+} and Ta^{5+}), including 10 unreported compounds, were successfully synthesised.[502] In stark contrast to the previously discussed Bi_4MO_8X in which the VBM and CBM levels are almost unchanged, both the VBM and CBM of $A_4A'M_2O_{11}Cl$ were variable to some degree with the change of composition. Furthermore, it was noted that the photoconductivity could be controlled by changing the concentration of 6s electron-containing cations and the electrostatic repulsion between the metal cations.

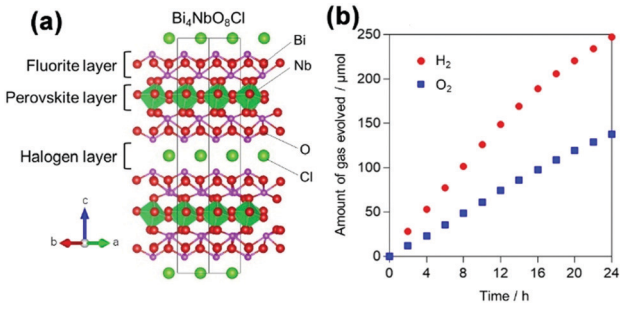


Fig. 19 (a) Crystal structure of Bi_4NbO_8Cl. (b) Visible-light-driven Z-scheme water splitting using Bi_4NbO_8Cl-based and $SrTiO_3$-based photocatalysts, in the presence of Fe^{3+}/Fe^{2+} redox mediator. Reproduced with permission.[495] Copyright 2016, American Chemical Society.

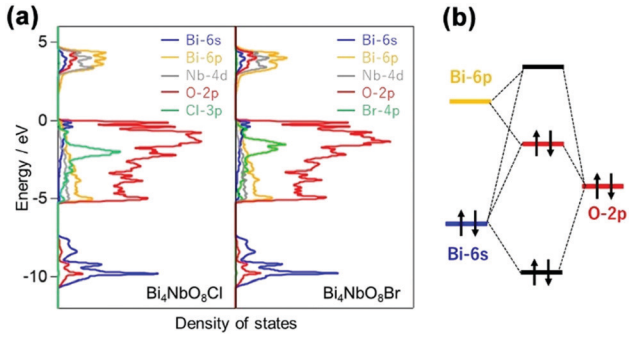


Fig. 20 (a) Density of states (DOS) of Bi_4NbO_8X (X = Cl, Br) (b) Interactions among Bi-6s, Bi-6p and O-2p orbitals based on the revised lone pair model.

This journal is © The Royal Society of Chemistry 2021

These results on double layered perovskite oxyhalides strongly suggest the potential of extending cation substitution for achieving optimized photocatalytic performance for visible light-induced water splitting. Very recently, a triple-layered (n = 3) Sillén–Aurivillius oxyhalide and simple Sillén oxyhalides have also shown functionality as photocatalysts for water oxidation and/or reduction,[122,503] suggesting a broad range of possibilities for tailoring the band structures and resulting photocatalysis performances by manipulating the stacking pattern of the layers in these layered oxyhalide perovskites.

5. Conclusions and perspective

5.1. Summary of perovskite photocatalysts

The conversion of solar energy to chemical energy by the generation of clean fuel from water or carbon dioxide and pollutant degradation will bring both economic and environmental benefit. Given that redox reactions are initiated by the photo-induced electrons and holes generated in nanoparticle photocatalysis, this requires the photocatalysts to have the capacity of light absorption, charge separation and transfer, and sufficient accessible active sites. Perovskites that feature a range of structures and structure-dependent properties are considered promising photocatalysts for various photocatalytic reactions. For perovskite oxides, the distinctive 3D network of BO_6 octahedra facilitates the charge transfer, and the facile deformation of these BO_6 octahedra contributes to charge separation. As the VB of perovskite oxides is usually formed by the O 2p orbitals while the CB is derived from the 3d orbitals of the transition metal ions, most of them exhibit strong oxidizing power and good reducing ability to drive photocatalytic reactions. For a smaller bandgap and the ability to harvest more visible light, perovskite halides have been studied, in which the p-orbitals of the X anions contribute to the more negative VBM, however the stability of these compounds under oxygen, moisture and illumination is a major concern. Alternatively, perovskite oxyhalides are considered as promising photocatalysts with both intrinsically high stability and appropriately positioned band structures for many photocatalytic applications.

5.2. Summary of design strategies

Photocatalytic reactions consist of three primary steps: light absorption; charge separation and transportation to the catalyst surface; and reduction and oxidation of reactants. Based on the principles of photocatalytic reactions, effective strategies have been established to design efficient perovskite photocatalysts.

For catalysts viable in visible-light photocatalytic applications, these materials must possess a bandgap in the range of 1.5–2.5 eV. Since the bandgap of most oxide perovskites is over 3 eV, bandgap engineering achieved by introducing foreign ions into A, B or X-sites can reduce their bandgap and extend the light absorption.[96,177,253] However, doping foreign ions may impair photoactivity by forming recombination centres, and thus the type and amount of dopant must be carefully controlled. An alternative approach combines the perovskite with a narrow bandgap compound (*e.g.*, bismuth oxyhalides, QDs),[194,242] dye molecules,[436] plasmonic metals[303] or upconversion materials,[149] to enhance light absorption.

Efficient photocatalysts should have fast charge transport and low charge recombination rates. Reducing particle sizes to shorten the diffusion length of charge carriers can effectively suppress charge recombination,[216] while enhancing crystallinity eliminates recombination centres,[504] resulting in longer-lived charge carriers. The formation of 1D or 2D nanoparticles can encourage anisotropic charge diffusion, decreasing charge recombination.[331] Charge recombination can also be avoided by spatial separation of the reduction and oxidation reactions. The construction of type II heterojunctions and Z-scheme systems, where reduction and oxidation occur on different components, is beneficial for charge separation.[179,505] Note that in most cases narrow bandgap compounds are preferred, as they can serve as light absorbers as well. Conductive materials, such as r-GO, have been integrated with perovskites as electron extractors to facilitate charge transport.[314]

The activities of the reduction and oxidation reactions are affected by the CB/VB positions and number of accessible active sites. Doping is one of the most frequently used approaches to tune the CB/VB positions, in particular anion dopants with higher electronegativity result in more positive VBM and stronger oxidizing ability.[359] Besides, more active sites are exposed with smaller particles and growth of specific crystal facets.[175,216] Intriguingly, facet engineering also contributes to the selectivity and spatial separation of reduction and oxidation reactions,[174] in that active sites for reduction and oxidation would be on different facets, hence separated. Loading co-catalysts on perovskite photocatalysts is another common approach to enhance activity (noting that noble metals, *e.g.*, Pt, Ru, and Rh, are frequently used co-catalysts. Although small amounts (0.1–1 wt%) are required, this leads to high production cost). To reduce the cost and ensure sustainability, we suggest the use of earth-abundant co-catalysts such as Ni@NiO_x.[190]

As a practical photocatalyst, the as-designed perovskites should exhibit good stability during photocatalytic reactions. This is the major concern for halide perovskite photocatalyst development. Several strategies have been adopted to improve the stability, including forming an all-inorganic chemical structure, doping stable ions, constructing heterojunctions and exploring photocatalytic reactions in non-polar environments or saturated halo acid solutions.

By applying these effective strategies, many excellent perovskite-based photocatalysts have been synthesized, showing superior efficiency and stability. Based on the principles of these design strategies, researchers can select earth-abundant, non-toxic materials as precursors and use simple routes to synthesize the target photocatalysts.

5.3. Perspective

From the point of commercial use, in addition to high efficiency, the photocatalysts must be stable in redox reactions and composed of earth-abundant elements that are low cost and

meet sustainability requirements. Because of the structural simplicity and flexibility of perovskites, a wide variety of compositional elements can be chosen to produce novel perovskites or optimize the photocatalytic performances of the reported perovskites for practical uses. In contrast to the traditional synthesis and characterization approach, which has been extensively used in photocatalyst development but becomes a slow process in investigating the continuously emerging perovskite candidates, theoretical prediction by which models are established on the basis of the profound understanding of the structure–property relation is a powerful tool for the design of improved photocatalysts. By using DFT calculations, Abe *et al.* revealed that in the layered oxyhalides $ABiO_2X$ (A = Pb, Sr, Ba; X = Cl, Br, I), the interaction between O 2p orbitals and outermost s orbitals of A lead to the shift of the VBM, and thus photocatalysts with narrow bandgap and the required VBM could be designed by constructing layered perovskites containing post transition metal cations with variation in stacking sequence and number of perovskite layers.[122,502] Singh *et al.* proposed a data-driven strategy based on first principle calculations that rapidly screened 68 860 candidates to find synthesizable materials for CO_2 photocatalytic reduction.[506] By estimating the thermodynamic stability, bandgap, aqueous stability and band edge of the candidates, 43 novel promising materials, including some perovskites, were identified for further investigation. This data-driven screening strategy undoubtedly paves the way for the fast development of photocatalysts.

Apart from DFT calculations, machine learning techniques can be used to discover relationships, interpret patterns and extract knowledge from multidimensional material databases and the vast amount of published results.[507,508] Currently, supervised and unsupervised natural language processing has been applied for the retrieval of information from scientific literature and the discovery of the underlying development in some regimes.[509,510] Distinct models have been built through machine learning algorithms, which exhibited remarkable agreement between the experimental and predicted values.[511–514] Extracting useful information from the photocatalysis literature and determining how to represent the perovskites by descriptors that involve compositional and structural variables uniquely for the establishment of model, will be challenges for designing perovskite photocatalysts by machine learning.[507] The lack of unified standards for comparison of photocatalytic systems will be a substantial obstacle for using machine learning techniques to optimize photocatalysts. As a result, it is important to establish standardization protocols for perovskite photocatalysis measurement and evaluation.

The perovskite photocatalytic mechanism and the relationship between crystal structure, the behaviours of the photoelectrons at the surface, and the photocatalytic activity should also be investigated. *In situ* technologies, including photoluminescence spectroscopy and surface potential detection, are important to study the photophysics of excited states and the transfer and recombination of the photo-induced charges. These techniques provide information for the surface defects, surface states and the processes of charge separation and recombination. Parameters that are important to the understanding of the photocatalytic mechanism and the further investigation of the correlation between the photocatalytic activity and the ferroelectric, piezoelectric and ferromagnetic properties.[515–517] Earth-abundant nontoxic perovskite photocatalysts should play a significant role in future sustainable energy supply and for environmental pollutant degradation, but will require collective standardization by photocatalysis researchers and further focus on the material design and understanding of the mechanism.

Conflicts of interest

There are no conflicts to declare.

Acknowledgements

Funding from an Australian Research Council Discovery Project, DP180103815, is acknowledged.

References

1 Y. Tachibana, L. Vayssieres and J. R. Durrant, *Nat. Photonics*, 2012, **6**, 511–518.
2 N. S. Lewis, *Science*, 2007, **315**, 798–801.
3 C. Furlan and C. Mortarino, *Renewable Sustainable Energy Rev.*, 2018, **81**, 1879–1886.
4 M. Meinshausen, N. Meinshausen, W. Hare, S. C. B. Raper, K. Frieler, R. Knutti, D. J. Frame and M. R. Allen, *Nature*, 2009, **458**, 1158–1162.
5 W. Wang, M. O. Tade and Z. P. Shao, *Chem. Soc. Rev.*, 2015, **44**, 5371–5408.
6 D. J. Martin, G. G. Liu, S. J. A. Moniz, Y. P. Bi, A. M. Beale, J. H. Ye and J. W. Tang, *Chem. Soc. Rev.*, 2015, **44**, 7808–7828.
7 X. Li, J. G. Yu, M. Jaroniec and X. B. Chen, *Chem. Rev.*, 2019, **119**, 3962–4179.
8 N. Kannan and D. Vakeesan, *Renewable Sustainable Energy Rev.*, 2016, **62**, 1092–1105.
9 G. Zhang, G. Liu, L. Z. Wang and J. T. S. Irvine, *Chem. Soc. Rev.*, 2016, **45**, 5951–5984.
10 S. S. Chen, T. Takata and K. Domen, *Nat. Rev. Mater*, 2017, **2**, 17050.
11 J. W. Fu, J. G. Yu, C. J. Jiang and B. Cheng, *Adv. Energy Mater.*, 2018, **8**, 1701503.
12 J. Low, J. Yu, M. Jaroniec, S. Wageh and A. A. Al-Ghamdi, *Adv. Mater.*, 2017, **29**, 1601694.
13 Y. Goto, T. Hisatomi, Q. Wang, T. Higashi, K. Ishikiriyama, T. Maeda, Y. Sakata, S. Okunaka, H. Tokudome, M. Katayama, S. Akiyama, H. Nishiyama, Y. Inoue, T. Takewaki, T. Setoyama, T. Minegishi, T. Takata, T. Yamada and K. Domen, *Joule*, 2018, **2**, 509–520.
14 T. Hisatomi and K. Domen, *Nat. Catal*, 2019, **2**, 387–399.
15 Q. Wang and K. Domen, *Chem. Rev.*, 2020, **120**, 919–985.

 This journal is © The Royal Society of Chemistry 2021

16 H. Park, H. I. Kim, G. H. Moon and W. Choi, *Energy Environ. Sci.*, 2016, **9**, 411–433.
17 J. M. R. Narayanam and C. R. J. Stephenson, *Chem. Soc. Rev.*, 2011, **40**, 102–113.
18 L. Marzo, S. K. Pagire, O. Reiser and B. König, *Angew. Chem., Int. Ed.*, 2018, **57**, 10034–10072.
19 A. Fujishima and K. Honda, *Nature*, 1972, **238**, 37–38.
20 M. Z. Ge, Q. S. Li, C. Y. Cao, J. Y. Huang, S. H. Li, S. N. Zhang, Z. Chen, K. Q. Zhang, S. S. Al-Deyab and Y. K. Lai, *Adv. Sci.*, 2017, **4**, 1600152.
21 H. Wei, W. A. McMaster, J. Z. Y. Tan, D. Chen and R. A. Caruso, *J. Mater. Chem. A*, 2018, **6**, 7236–7245.
22 S. S. Chen, S. Shen, G. J. Liu, Y. Qi, F. X. Zhang and C. Li, *Angew. Chem., Int. Ed.*, 2015, **54**, 3047–3051.
23 Z. Wang, Y. Inoue, T. Hisatomi, R. Ishikawa, Q. Wang, T. Takata, S. Chen, N. Shibata, Y. Ikuhara and K. Domen, *Nat. Catal*, 2018, **1**, 756–763.
24 Q. Wang, M. Nakabayashi, T. Hisatomi, S. Sun, S. Akiyama, Z. Wang, Z. Pan, X. Xiao, T. Watanabe, T. Yamada, N. Shibata, T. Takata and K. Domen, *Nat. Mater.*, 2019, **18**, 827–832.
25 T. W. Kim and K. S. Choi, *Science*, 2014, **343**, 990–994.
26 Z. G. Yi, J. H. Ye, N. Kikugawa, T. Kako, S. X. Ouyang, H. Stuart-Williams, H. Yang, J. Y. Cao, W. J. Luo, Z. S. Li, Y. Liu and R. L. Withers, *Nat. Mater.*, 2010, **9**, 559–564.
27 P. Wang, B. B. Huang, X. Y. Qin, X. Y. Zhang, Y. Dai, J. Y. Wei and M. H. Whangbo, *Angew. Chem., Int. Ed.*, 2008, **47**, 7931–7933.
28 G. X. Zhao, Y. B. Sun, W. Zhou, X. K. Wang, K. Chang, G. G. Liu, H. M. Liu, T. Kako and J. H. Ye, *Adv. Mater.*, 2017, **29**, 1703258.
29 X. C. Wang, K. Maeda, A. Thomas, K. Takanabe, G. Xin, J. M. Carlsson, K. Domen and M. Antonietti, *Nat. Mater.*, 2009, **8**, 76–80.
30 W. J. Ong, L. L. Tan, Y. H. Ng, S. T. Yong and S. P. Chai, *Chem. Rev.*, 2016, **116**, 7159–7329.
31 J. K. Liu, S. H. Wen, Y. Hou, F. Zuo, G. J. O. Beran and P. Y. Feng, *Angew. Chem., Int. Ed.*, 2013, **52**, 3241–3245.
32 M. Latorre-Sanchez, A. Primo and H. Garcia, *Angew. Chem., Int. Ed.*, 2013, **52**, 11813–11816.
33 M. Z. Rahman, C. W. Kwong, K. Davey and S. Z. Qiao, *Energy Environ. Sci.*, 2016, **9**, 1513–1514.
34 S. Ghosh, N. A. Kouame, L. Ramos, S. Remita, A. Dazzi, A. Deniset-Besseau, P. Beaunier, F. Goubard, P. H. Aubert and H. Remita, *Nat. Mater.*, 2015, **14**, 505–511.
35 R. S. Sprick, J. X. Jiang, B. Bonillo, S. J. Ren, T. Ratvijitvech, P. Guiglion, M. A. Zwijnenburg, D. J. Adams and A. I. Cooper, *J. Am. Chem. Soc.*, 2015, **137**, 3265–3270.
36 L. Wang, Y. Y. Wan, Y. J. Ding, S. K. Wu, Y. Zhang, X. L. Zhang, G. Q. Zhang, Y. J. Xiong, X. J. Wu, J. L. Yang and H. X. Xu, *Adv. Mater.*, 2017, **29**, 1702428.
37 H. L. Wang, L. S. Zhang, Z. G. Chen, J. Q. Hu, S. J. Li, Z. H. Wang, J. S. Liu and X. C. Wang, *Chem. Soc. Rev.*, 2014, **43**, 5234–5244.
38 J. L. White, M. F. Baruch, J. E. Pander, Y. Hu, I. C. Fortmeyer, J. E. Park, T. Zhang, K. Liao, J. Gu, Y. Yan, T. W. Shaw, E. Abelev and A. B. Bocarsly, *Chem. Rev.*, 2015, **115**, 12888–12935.
39 S. J. A. Moniz, S. A. Shevlin, D. J. Martin, Z. X. Guo and J. W. Tang, *Energy Environ. Sci.*, 2015, **8**, 731–759.
40 J. X. Low, C. Jiang, B. Cheng, S. Wageh, A. A. Al-Ghamdi and J. G. Yu, *Small Methods*, 2017, **1**, 1700080.
41 Y. O. Wang, H. Suzuki, J. J. Xie, O. Tomita, D. J. Martin, M. Higashi, D. Kong, R. Abe and J. W. Tang, *Chem. Rev.*, 2018, **118**, 5201–5241.
42 B. A. Pinaud, J. D. Benck, L. C. Seitz, A. J. Forman, Z. B. Chen, T. G. Deutsch, B. D. James, K. N. Baum, G. N. Baum, S. Ardo, H. L. Wang, E. Miller and T. F. Jaramillo, *Energy Environ. Sci.*, 2013, **6**, 1983–2002.
43 M. A. Pena and J. L. G. Fierro, *Chem. Rev.*, 2001, **101**, 1981–2017.
44 Q. Wang, T. Hisatomi, Q. X. Jia, H. Tokudome, M. Zhong, C. Z. Wang, Z. H. Pan, T. Takata, M. Nakabayashi, N. Shibata, Y. B. Li, I. D. Sharp, A. Kudo, T. Yamada and K. Domen, *Nat. Mater.*, 2016, **15**, 611–615.
45 W. J. Yin, B. C. Weng, J. Ge, Q. D. Sun, Z. Z. Li and Y. F. Yan, *Energy Environ. Sci.*, 2019, **12**, 442–462.
46 E. Grabowska, *Appl. Catal., B*, 2016, **186**, 97–126.
47 A. Kumar, A. Kumar and V. Krishnan, *ACS Catal.*, 2020, **10**, 10253–10315.
48 J. R. Ran, J. Zhang, J. G. Yu, M. Jaroniec and S. Z. Qiao, *Chem. Soc. Rev.*, 2014, **43**, 7787–7812.
49 G. B. Haxel, J. B. Hedrick and G. J. Orris, *Rare earth elements – critical resources for high technology*, in Department of the Interior, http://pubs.usgs.gov/fs/2002/fs087-02/.
50 Commodity Statistics and Information, https://www.usgs.gov/centers/nmic/commodity-statistics-and-information.
51 V. M. Goldschmidt, *Ber. Dtsch. Chem. Ges.*, 1927, **60**, 1263–1296.
52 C. Li, K. C. K. Soh and P. Wu, *J. Alloys Compd.*, 2004, **372**, 40–48.
53 C. H. Li, X. G. Lu, W. Z. Ding, L. M. Feng, Y. H. Gao and Z. G. Guo, *Acta. Crystallogr. B: Struct. Sci. Cryst. Eng. Mater.*, 2008, **64**, 702–707.
54 W. Travis, E. N. K. Glover, H. Bronstein, D. O. Scanlon and R. G. Palgrave, *Chem. Sci.*, 2016, **7**, 4548–4556.
55 G. Pilania, P. V. Balachandran, C. Kim and T. Lookman, *Front. Mater*, 2016, **3**, 19.
56 S. Lu, Q. Zhou, L. Ma, Y. Guo and J. Wang, *Small Methods*, 2019, **3**, 1900360.
57 C. J. Bartel, C. Sutton, B. R. Goldsmith, R. H. Ouyang, C. B. Musgrave, L. M. Ghiringhelli and M. Scheffler, *Sci. Adv.*, 2019, **5**, eaav0693.
58 Q. Sun and W.-J. Yin, *J. Am. Chem. Soc.*, 2017, **139**, 14905–14908.
59 D. Neagu, G. Tsekouras, D. N. Miller, H. Menard and J. T. S. Irvine, *Nat. Chem.*, 2013, **5**, 916–923.
60 R. K. Sharma, N. H. Chan and D. M. Smyth, *J. Am. Ceram. Soc.*, 1981, **64**, 448–451.
61 F. K. Meng, Z. L. Hong, J. Arndt, M. Li, M. J. Zhi, F. Yang and N. Q. Wu, *Nano Res.*, 2012, **5**, 213–221.
62 W. Dong, D. Cortie, T. Lu, Q. B. Sun, N. Narayanan, W. B. Hu, L. Jacob, Q. Li, D. H. Yu, H. Chen, A. P. Chen,

X. Y. Wei, G. M. Wang, M. G. Humphrey, T. J. Frankcombe and Y. Liu, *Mater. Horiz.*, 2019, **6**, 1717–1725.
63 P. Xu, S. Chen, H.-J. Xiang, X.-G. Gong and S.-H. Wei, *Chem. Mater.*, 2014, **26**, 6068–6072.
64 B. Liu, V. R. Cooper, H. X. Xu, H. Y. Xiao, Y. W. Zhang and W. J. Weber, *Phys. Chem. Chem. Phys.*, 2014, **16**, 15590–15596.
65 D. Lee, H. Lu, Y. Gu, S. Y. Choi, S. D. Li, S. Ryu, T. R. Paudel, K. Song, E. Mikheev, S. Lee, S. Stemmer, D. A. Tenne, S. H. Oh, E. Y. Tsymbal, X. Wu, L. Q. Chen, A. Gruverman and C. B. Eom, *Science*, 2015, **349**, 1314–1317.
66 M. T. Anderson, K. B. Greenwood, G. A. Taylor and K. R. Poeppelmeier, *Prog. Solid State Chem.*, 1993, **22**, 197–233.
67 G. King and P. M. Woodward, *J. Mater. Chem.*, 2010, **20**, 5785–5796.
68 D. Rubi, J. Nogués, J. S. Muñoz and J. Fontcuberta, *Mater. Sci. Eng., B*, 2006, **126**, 279–282.
69 L. Zhou, Y. F. Xu, B. X. Chen, D. B. Kuang and C. Y. Su, *Small*, 2018, **14**, 1703762.
70 M. T. Anderson and K. R. Poeppelmeier, *Chem. Mater.*, 1991, **3**, 476–482.
71 S. Vasala and M. Karppinen, *Prog. Solid State Chem.*, 2015, **43**, 1–36.
72 A. Maignan, C. Martin, D. Pelloquin, N. Nguyen and B. Raveau, *J. Solid State Chem.*, 1999, **142**, 247–260.
73 A. Grimaud, K. J. May, C. E. Carlton, Y. L. Lee, M. Risch, W. T. Hong, J. G. Zhou and Y. Shao-Horn, *Nat. Commun.*, 2013, **4**, 2439.
74 X. Xu, Y. Zhong and Z. Shao, *Trends Chem.*, 2019, **1**, 410–424.
75 E. J. Cussen and P. D. Battle, *J. Mater. Chem.*, 2003, **13**, 1210–1214.
76 R. E. Schaak and T. E. Mallouk, *Chem. Mater.*, 2002, **14**, 1455–1471.
77 Y. Hu, L. Mao, X. Guan, K. A. Tucker, H. Xie, X. Wu and J. Shi, *Renewable Sustainable Energy Rev.*, 2020, **119**, 109527.
78 J. Qiu, Y. Xia, Y. Chen and W. Huang, *Adv. Sci.*, 2019, **6**, 1800793.
79 H. Tsai, W. Nie, J.-C. Blancon, C. C. Stoumpos, C. M. M. Soe, J. Yoo, J. Crochet, S. Tretiak, J. Even, A. Sadhanala, G. Azzellino, R. Brenes, P. M. Ajayan, V. Bulović, S. D. Stranks, R. H. Friend, M. G. Kanatzidis and A. D. Mohite, *Adv. Mater.*, 2018, **30**, 1704217.
80 H. Tsai, W. Nie, J.-C. Blancon, C. C. Stoumpos, R. Asadpour, B. Harutyunyan, A. J. Neukirch, R. Verduzco, J. J. Crochet, S. Tretiak, L. Pedesseau, J. Even, M. A. Alam, G. Gupta, J. Lou, P. M. Ajayan, M. J. Bedzyk, M. G. Kanatzidis and A. D. Mohite, *Nature*, 2016, **536**, 312–316.
81 K. Shimizu, S. Itoh, T. Hatamachi, T. Kodama, M. Sato and K. Toda, *Chem. Mater.*, 2005, **17**, 5161–5166.
82 X. X. He, Y. G. Wang, K. Li, X. Wang, P. Liu, Y. J. Yang, Q. Liao, T. Y. Zhai, J. N. Yao and H. B. Fu, *ACS Appl. Mater. Interfaces*, 2019, **11**, 15905–15912.
83 Y. Ebina, T. Sasaki, M. Harada and M. Watanabe, *Chem. Mater.*, 2002, **14**, 4390–4395.
84 Y. Miseki, H. Kato and A. Kudo, *Energy Environ. Sci.*, 2009, **2**, 306–314.
85 A. Kudo and Y. Miseki, *Chem. Soc. Rev.*, 2009, **38**, 253–278.
86 T. Cai, W. Shi, S. Hwang, K. Kobbekaduwa, Y. Nagaoka, H. Yang, K. Hills-Kimball, H. Zhu, J. Wang, Z. Wang, Y. Liu, D. Su, J. Gao and O. Chen, *J. Am. Chem. Soc.*, 2020, **142**, 11927–11936.
87 X. B. Chen, S. H. Shen, L. J. Guo and S. S. Mao, *Chem. Rev.*, 2010, **110**, 6503–6570.
88 A. Li, Q. Cao, G. Zhou, B. V. K. J. Schmidt, W. Zhu, X. Yuan, H. Huo, J. Gong and M. Antonietti, *Angew. Chem., Int. Ed.*, 2019, **58**, 14549–14555.
89 J. Yuan, H. Liu, S. Wang and X. Li, *Nanoscale*, 2021, **13**, 10281–10304.
90 R. Konta, T. Ishii, H. Kato and A. Kudo, *J. Phys. Chem. B*, 2004, **108**, 8992–8995.
91 D. F. Wang, T. Kako and J. H. Ye, *J. Am. Chem. Soc.*, 2008, **130**, 2724–2725.
92 J.-P. Correa-Baena, L. Nienhaus, R. C. Kurchin, S. S. Shin, S. Wieghold, N. T. Putri Hartono, M. Layurova, N. D. Klein, J. R. Poindexter, A. Polizzotti, S. Sun, M. G. Bawendi and T. Buonassisi, *Chem. Mater.*, 2018, **30**, 3734–3742.
93 K. Iwashina and A. Kudo, *J. Am. Chem. Soc.*, 2011, **133**, 13272–13275.
94 T. Ishii, H. Kato and A. Kudo, *J. Photochem. Photobiol. A: Chem.*, 2004, **163**, 181–186.
95 R. Niishiro, H. Kato and A. Kudo, *Phys. Chem. Chem. Phys.*, 2005, **7**, 2241–2245.
96 S. X. Ouyang, H. Tong, N. Umezawa, J. Y. Cao, P. Li, Y. P. Bi, Y. J. Zhang and J. H. Ye, *J. Am. Chem. Soc.*, 2012, **134**, 1974–1977.
97 P. Reunchan, S. X. Ouyang, N. Umezawa, H. Xu, Y. J. Zhang and J. H. Ye, *J. Mater. Chem. A*, 2013, **1**, 4221–4227.
98 S. Pasternak and Y. Paz, *ChemPhysChem*, 2013, **14**, 2059–2070.
99 F. F. Li, D. R. Liu, G. M. Gao, B. Xue and Y. S. Jiang, *Appl. Catal., B*, 2015, **166**, 104–111.
100 J. G. Hou, S. Y. Cao, Y. Z. Wu, F. Liang, L. Ye, Z. S. Lin and L. C. Sun, *Nano Energy*, 2016, **30**, 59–68.
101 W. Wang, M. O. Tade and Z. P. Shao, *Prog. Mater. Sci.*, 2018, **92**, 33–63.
102 X. Wang, T. Hisatomi, Z. Wang, J. Song, J. Qu, T. Takata and K. Domen, *Angew. Chem., Int. Ed.*, 2019, **58**, 10666–10670.
103 K. Ogawa, A. Nakada, H. Suzuki, O. Tomita, M. Higashi, A. Saeki, H. Kageyama and R. Abe, *ACS Appl. Mater. Interfaces*, 2019, **11**, 5642–5650.
104 Y. G. Su, B. L. Zhu, K. Guan, S. S. Gao, L. Lv, C. F. Du, L. M. Peng, L. C. Hou and X. J. Wang, *J. Phys. Chem. C*, 2012, **116**, 18508–18517.
105 Y. J. Wang, H. Xu, C. Y. Shao and J. Cao, *Appl. Surf. Sci.*, 2017, **392**, 649–657.
106 S. Thirumalairajan, K. Girija, N. Y. Hebalkar, D. Mangalaraj, C. Viswanathan and N. Ponpandian, *RSC Adv.*, 2013, **3**, 7549–7561.
107 N. Nuraje, X. N. Dang, J. F. Qi, M. A. Allen, Y. Lei and A. M. Belcher, *Adv. Mater.*, 2012, **24**, 2885–2889.
108 Q. Kuang and S. H. Yang, *ACS Appl. Mater. Interfaces*, 2013, **5**, 3683–3690.

 This journal is © The Royal Society of Chemistry 2021

109 O. Kucuk, S. Teber, I. C. Kaya, H. Akyildiz and V. Kalem, *J. Alloys Compd.*, 2018, **765**, 82–91.
110 H. X. Mai, Y. W. Zhang, R. Si, Z. G. Yan, L. D. Sun, L. P. You and C. H. Yan, *J. Am. Chem. Soc.*, 2006, **128**, 6426–6436.
111 J. Shamsi, A. S. Urban, M. Imran, L. De Trizio and L. Manna, *Chem. Rev.*, 2019, **119**, 3296–3348.
112 Z. Wang, C. Li and K. Domen, *Chem. Soc. Rev.*, 2019, **48**, 2109–2125.
113 Q. L. Xu, L. Y. Zhang, J. G. Yu, S. Wageh, A. A. Al-Ghamdi and M. Jaroniec, *Mater. Today*, 2018, **21**, 1042–1063.
114 N. Fajrina and M. Tahir, *Int. J. Hydrogen Energy*, 2019, **44**, 540–577.
115 S. Bai, J. Jiang, Q. Zhang and Y. J. Xiong, *Chem. Soc. Rev.*, 2015, **44**, 2893–2939.
116 W. J. Yin, S. Bai, Y. J. Zhong, Z. Q. Li and Y. Xie, *ChemNanoMat*, 2016, **2**, 732–738.
117 L. M. Sun, Y. Qi, C. J. Jia, Z. Jin and W. L. Fan, *Nanoscale*, 2014, **6**, 2649–2659.
118 J. X. Low, S. W. Cao, J. G. Yu and S. Wageh, *Chem. Commun.*, 2014, **50**, 10768–10777.
119 D. L. Jiang, T. Y. Wang, Q. Xu, D. Li, S. C. Meng and M. Chen, *Appl. Catal., B*, 2017, **201**, 617–628.
120 S. F. Yang, C. G. Niu, D. W. Huang, H. Zhang, C. Lianga and G. M. Zeng, *Environ. Sci.: Nano*, 2017, **4**, 585–595.
121 J. T. Lee, Y. J. Chen, E. C. Su and M. Y. Wey, *Int. J. Hydrogen Energy*, 2019, **44**, 21413–21423.
122 H. Suzuki, H. Kunioku, M. Higashi, O. Tomita, D. Kato, H. Kageyama and R. Abe, *Chem. Mater.*, 2018, **30**, 5862–5869.
123 R. Abe, M. Higashi and K. Domen, *ChemSusChem*, 2011, **4**, 228–237.
124 Y. Miseki, S. Fujiyoshi, T. Gunji and K. Sayama, *J. Phys. Chem. C*, 2017, **121**, 9691–9697.
125 H. Tada, T. Mitsui, T. Kiyonaga, T. Akita and K. Tanaka, *Nat. Mater.*, 2006, **5**, 782–786.
126 Z. Y. Jiang, J. Q. Pan, B. B. Wang and C. R. Li, *Appl. Surf. Sci.*, 2018, **436**, 519–526.
127 W. K. Jo, S. Kumar, S. Eslava and S. Tonda, *Appl. Catal., B*, 2018, **239**, 586–598.
128 J. G. Yu, S. H. Wang, J. X. Low and W. Xiao, *Phys. Chem. Chem. Phys.*, 2013, **15**, 16883–16890.
129 Q. Wang, T. Hisatomi, S. S. K. Ma, Y. B. Li and K. Domen, *Chem. Mater.*, 2014, **26**, 4144–4150.
130 Q. X. Jia, A. Iwase and A. Kudo, *Chem. Sci.*, 2014, **5**, 1513–1519.
131 A. Rauf, M. Ma, S. Kim, M. S. A. S. Shah, C. H. Chung, J. H. Park and P. J. Yoo, *Nanoscale*, 2018, **10**, 3026–3036.
132 M. L. Li, L. X. Zhang, X. Q. Fan, Y. J. Zhou, M. Y. Wu and J. L. Shi, *J. Mater. Chem. A*, 2015, **3**, 5189–5196.
133 W. K. Jo, J. Y. Lee and T. S. Natarajan, *Phys. Chem. Chem. Phys.*, 2016, **18**, 1000–1016.
134 H. Li, Y. Zhou, W. Tu, J. Ye and Z. Zou, *Adv. Funct. Mater.*, 2015, **25**, 998–1013.
135 H. Mai, T. Lu, Q. Sun, J. Langley, N. Cox, F. Kremer, T. Duong, K. Catchpole, H. Chen, Z. Yi, T. J. Frankcombe and Y. Liu, *J. Mater. Chem. A*, 2021, **9**, 13182–13191.
136 X. H. Zhang, T. Y. Peng and S. S. Song, *J. Mater. Chem. A*, 2016, **4**, 2365–2402.
137 S. Linic, P. Christopher and D. B. Ingram, *Nat. Mater.*, 2011, **10**, 911–921.
138 D. Lu, S. X. Ouyang, H. Xu, D. W. Li, X. L. Zhang, Y. X. Li and J. H. Ye, *ACS Appl. Mater. Interfaces*, 2016, **8**, 9506–9513.
139 Q. Zhang, Y. Huang, L. F. Xu, J. J. Cao, W. K. Ho and S. C. Lee, *ACS Appl. Mater. Interfaces*, 2016, **8**, 4165–4174.
140 S. W. Zhang, S. Li, B. P. Zhang, D. F. Yu, Z. T. Zhang and J. F. Li, *RSC Adv.*, 2019, **9**, 5045–5052.
141 G. Jiang, X. Li, M. Lan, T. Shen, X. Lv, F. Dong and S. Zhang, *Appl. Catal., B*, 2017, **205**, 532–540.
142 A. Comin and L. Manna, *Chem. Soc. Rev.*, 2014, **43**, 3957–3975.
143 G. Sreedhar, A. Sivanantham, S. Venkateshwaran, S. K. Panda and M. Eashwar, *J. Mater. Chem. A*, 2015, **3**, 13476–13482.
144 X. F. Liu and J. R. Qiu, *Chem. Soc. Rev.*, 2015, **44**, 8714–8746.
145 J. K. Stolarczyk, S. Bhattacharyya, L. Polavarapu and J. Feldmann, *ACS Catal.*, 2018, **8**, 3602–3635.
146 X. Y. Huang, S. Y. Han, W. Huang and X. G. Liu, *Chem. Soc. Rev.*, 2013, **42**, 173–201.
147 H. X. Mai, Y. W. Zhang, L. D. Sun and C. H. Yan, *J. Phys. Chem. C*, 2007, **111**, 13721–13729.
148 H. X. Mai, T. Lu, Q. Li, Q. B. Sun, K. Vu, H. Chen, G. M. Wang, M. G. Humphrey, F. Kremer, L. Li, R. L. Withers and Y. Liu, *ACS Appl. Mater. Interfaces*, 2018, **10**, 29786–29794.
149 J. M. Zhang, Y. Huang, L. Jin, F. Rosei, F. Vetrone and J. P. Claverie, *ACS Appl. Mater. Interfaces*, 2017, **9**, 8142–8150.
150 H. Huang, B. Pradhan, J. Hofkens, M. B. J. Roeffaers and J. A. Steele, *ACS Energy Lett.*, 2020, **5**, 1107–1123.
151 R. Wang, M. Mujahid, Y. Duan, Z.-K. Wang, J. Xue and Y. Yang, *Adv. Funct. Mater.*, 2019, **29**, 1808843.
152 J. Huang, S. Tan, P. D. Lund and H. Zhou, *Energy Environ. Sci.*, 2017, **10**, 2284–2311.
153 J. S. Manser, M. I. Saidaminov, J. A. Christians, O. M. Bakr and P. V. Kamat, *Acc. Chem. Res.*, 2016, **49**, 330–338.
154 N. Aristidou, C. Eames, I. Sanchez-Molina, X. Bu, J. Kosco, M. S. Islam and S. A. Haque, *Nat. Commun.*, 2017, **8**, 15218.
155 F. Hao, C. C. Stoumpos, D. H. Cao, R. P. H. Chang and M. G. Kanatzidis, *Nat. Photonics*, 2014, **8**, 489–494.
156 J.-W. Lee, D.-H. Kim, H.-S. Kim, S.-W. Seo, S. M. Cho and N.-G. Park, *Adv. Energy Mater.*, 2015, **5**, 1501310.
157 Y.-F. Xu, M.-Z. Yang, B.-X. Chen, X.-D. Wang, H.-Y. Chen, D.-B. Kuang and C.-Y. Su, *J. Am. Chem. Soc.*, 2017, **139**, 5660–5663.
158 X. Zhu, Y. Lin, J. San Martin, Y. Sun, D. Zhu and Y. Yan, *Nat. Commun.*, 2019, **10**, 2843.
159 Z. Hong, W. K. Chong, A. Y. R. Ng, M. Li, R. Ganguly, T. C. Sum and H. S. Soo, *Angew. Chem., Int. Ed.*, 2019, **58**, 3456–3460.
160 J. Luo, W. Zhang, H. Yang, Q. Fan, F. Xiong, S. Liu, D.-S. Li and B. Liu, *EcoMat*, 2021, **3**, e12079.
161 E. T. McClure, M. R. Ball, W. Windl and P. M. Woodward, *Chem. Mater.*, 2016, **28**, 1348–1354.

162 K. Ogawa, H. Suzuki, C. Zhong, R. Sakamoto, O. Tomita, A. Saeki, H. Kageyama and R. Abe, *J. Am. Chem. Soc.*, 2021, **143**, 8446–8453.

163 M. Ou, W. G. Tu, S. M. Yin, W. N. Xing, S. Y. Wu, H. J. Wang, S. P. Wan, Q. Zhong and R. Xu, *Angew. Chem., Int. Ed.*, 2018, **57**, 13570–13574.

164 H. Liu, Y. Tan, M. Cao, H. Hu, L. Wu, X. Yu, L. Wang, B. Sun and Q. Zhang, *ACS Nano*, 2019, **13**, 5366–5374.

165 A. Pan, X. Ma, S. Huang, Y. Wu, M. Jia, Y. Shi, Y. Liu, P. Wangyang, L. He and Y. Liu, *J. Phys. Chem. Lett.*, 2019, 6590–6597.

166 H. Huang, J. Zhao, Y. Du, C. Zhou, M. Zhang, Z. Wang, Y. Weng, J. Long, J. Hofkens, J. A. Steele and M. B. J. Roeffaers, *ACS Nano*, 2020, **14**, 16689–16697.

167 Z.-J. Li, E. Hofman, J. Li, A. H. Davis, C.-H. Tung, L.-Z. Wu and W. Zheng, *Adv. Funct. Mater.*, 2018, **28**, 1704288.

168 L.-Y. Wu, Y.-F. Mu, X.-X. Guo, W. Zhang, Z.-M. Zhang, M. Zhang and T.-B. Lu, *Angew. Chem., Int. Ed.*, 2019, **58**, 9491–9495.

169 Z.-C. Kong, J.-F. Liao, Y.-J. Dong, Y.-F. Xu, H.-Y. Chen, D.-B. Kuang and C.-Y. Su, *ACS Energy Lett.*, 2018, **3**, 2656–2662.

170 I. Poli, U. Hintermair, M. Regue, S. Kumar, E. V. Sackville, J. Baker, T. M. Watson, S. Eslava and P. J. Cameron, *Nat. Commun.*, 2019, **10**, 2097.

171 F. T. Wagner and G. A. Somorjai, *Nature*, 1980, **285**, 559–560.

172 T. K. Townsend, N. D. Browning and F. E. Osterloh, *ACS Nano*, 2012, **6**, 7420–7426.

173 K. Yu, C. X. Zhang, Y. Chang, Y. J. Feng, Z. Q. Yang, T. Yang, L. L. Lou and S. X. Liu, *Appl. Catal., B*, 2017, **200**, 514–520.

174 B. Wang, S. H. Shen and L. J. Guo, *Appl. Catal., B*, 2015, **166**, 320–326.

175 L. C. Mu, Y. Zhao, A. L. Li, S. Y. Wang, Z. L. Wang, J. X. Yang, Y. Wang, T. F. Liu, R. T. Chen, J. Zhu, F. T. Fan, R. G. Li and C. Li, *Energy Environ. Sci.*, 2016, **9**, 2463–2469.

176 U. Sulaeman, S. Yin and T. Sato, *Appl. Catal., B*, 2011, **105**, 206–210.

177 H. Lyu, T. Hisatomi, Y. Goto, M. Yoshida, T. Higashi, M. Katayama, T. Takata, T. Minegishi, H. Nishiyama, T. Yamada, Y. Sakata, K. Asakura and K. Domen, *Chem. Sci.*, 2019, **10**, 3196–3201.

178 P. Li, C. B. Liu, G. L. Wu, Y. Heng, S. Lin, A. Ren, K. H. Lv, L. S. Xiao and W. D. Shi, *RSC Adv.*, 2014, **4**, 47615–47624.

179 Y. Lin, S. H. Wu, X. Li, X. Wu, C. P. Yang, G. M. Zeng, Y. R. Peng, Q. Zhou and L. Lu, *Appl. Catal., B*, 2018, **227**, 557–570.

180 X. Q. Ma, X. L. Cui, Z. Q. Zhao, M. A. Melo, E. J. Roberts and F. E. Osterloh, *J. Mater. Chem. A*, 2018, **6**, 5774–5781.

181 H. Kato and A. Kudo, *J. Phys. Chem. B*, 2002, **106**, 5029–5034.

182 A. Z. Jia, X. Zhang, F. Li and Y. J. Wang, *New J. Chem.*, 2019, **43**, 7409–7418.

183 T. Takata, J. Jiang, Y. Sakata, M. Nakabayashi, N. Shibata, V. Nandal, K. Seki, T. Hisatomi and K. Domen, *Nature*, 2020, **581**, 411–414.

184 M. Miyauchi, M. Takashio and H. Tobimatsu, *Langmuir*, 2004, **20**, 232–236.

185 H. Yu, S. C. Yan, Z. S. Li, T. Yu and Z. G. Zou, *Int. J. Hydrogen Energy*, 2012, **37**, 12120–12127.

186 K. Xie, N. Umezawa, N. Zhang, P. Reunchan, Y. J. Zhang and J. H. Ye, *Energy Environ. Sci.*, 2011, **4**, 4211–4219.

187 H. Q. Tan, Z. Zhao, W. B. Zhu, E. N. Coker, B. S. Li, M. Zheng, W. X. Yu, H. Y. Fan and Z. C. Sun, *ACS Appl. Mater. Interfaces*, 2014, **6**, 19184–19190.

188 S. Nishioka, J. Hyodo, J. J. M. Vequizo, S. Yamashita, H. Kumagai, K. Kimoto, A. Yamakata, Y. Yamazaki and K. Maeda, *ACS Catal.*, 2018, **8**, 7190–7200.

189 K. Domen, A. Kudo, T. Onishi, N. Kosugi and H. Kuroda, *J. Phys. Chem.*, 1986, **90**, 292–295.

190 K. Han, T. Kreuger, B. T. Mei and G. D. Mul, *ACS Catal.*, 2017, **7**, 1610–1614.

191 K. Han, D. M. Haiber, J. Knöppel, C. Lievens, S. Cherevko, P. Crozier, G. Mul and B. Mei, *ACS Catal.*, 2021, **11**, 11049–11058.

192 J. J. Guo, S. X. Ouyang, P. Li, Y. J. Zhang, T. Kako and J. H. Ye, *Appl. Catal., B*, 2013, **134**, 286–292.

193 Y. Z. Wei, J. Y. Wang, R. B. Yu, J. W. Wan and D. Wang, *Angew. Chem., Int. Ed.*, 2019, **58**, 1422–1426.

194 H. Ren, L. Ge, Q. Guo, L. Li, G. Hu and J. Li, *RSC Adv.*, 2018, **8**, 20157–20165.

195 W. Chen, H. Liu, X. Li, S. Liu, L. Gao, L. Mao, Z. Fan, W. Shangguan, W. Fang and Y. Liu, *Appl. Catal., B*, 2016, **192**, 145–151.

196 Y. Q. Zhong, K. Ueno, Y. Mori, X. Shi, T. Oshikiri, K. Murakoshi, H. Inoue and H. Misawa, *Angew. Chem., Int. Ed.*, 2014, **53**, 10350–10354.

197 Q. Kang, T. Wang, P. Li, L. Q. Liu, K. Chang, M. Li and J. H. Ye, *Angew. Chem., Int. Ed.*, 2015, **54**, 841–845.

198 X. F. Yang, J. X. Fu, C. J. Jin, J. A. Chen, C. L. Liang, M. M. Wu and W. Z. Zhou, *J. Am. Chem. Soc.*, 2010, **132**, 14279–14287.

199 J. D. Zhuang, Q. F. Tian, S. Lin, W. B. Yang, L. H. Chen and P. Liu, *Appl. Catal., B*, 2014, **156**, 108–115.

200 J. P. Zou, L. Z. Zhang, S. L. Luo, L. H. Leng, X. B. Luo, M. J. Zhang, Y. Luo and G. C. Guo, *Int. J. Hydrogen Energy*, 2012, **37**, 17068–17077.

201 S. N. Lim, S. A. Song, Y.-C. Jeong, H. W. Kang, S. B. Park and K. Y. Kim, *J. Electron. Mater.*, 2017, **46**, 6096–6103.

202 R. N. Wang, S. Ni, G. Liu and X. X. Xu, *Appl. Catal., B*, 2018, **225**, 139–147.

203 M. Chen, Q. Xiong, Z. Liu, K. Qiu and X. Xiao, *Ceram. Int.*, 2020, **46**, 12111–12119.

204 Y. Wang, C. G. Niu, L. Wang, Y. Wang, X. G. Zhang and G. M. Zeng, *RSC Adv.*, 2016, **6**, 47873–47882.

205 S. Wang, Y. Gao, S. Miao, T. Liu, L. Mu, R. Li, F. Fan and C. Li, *J. Am. Chem. Soc.*, 2017, **139**, 11771–11778.

206 R. E. Cohen, *Nature*, 1992, **358**, 136–138.

207 J. E. Spanier, V. M. Fridkin, A. M. Rappe, A. R. Akbashev, A. Polemi, Y. B. Qi, Z. Q. Gu, S. M. Young, C. J. Hawley, D. Imbrenda, G. Xiao, A. L. Bennett-Jackson and C. L. Johnson, *Nat. Photonics*, 2016, **10**, 611–616.

 This journal is © The Royal Society of Chemistry 2021

208 C. Srilakshmi, R. Saraf, V. Prashanth, G. M. Rao and C. Shivakumara, *Inorg. Chem.*, 2016, **55**, 4795–4805.

209 P. Senthilkumar, D. A. Jency, T. Kavinkumar, D. Dhayanithi, S. Dhanuskodi, M. Umadevi, S. Manivannan, N. V. Giridharan, V. Thiagarajan, M. Sriramkumar and K. Jothivenkatachalam, *ACS Sustainable Chem. Eng.*, 2019, **7**, 12032–12043.

210 I. C. Amaechi, A. Hadj Youssef, G. Kolhatkar, D. Rawach, C. Gomez-Yañez, J. P. Claverie, S. Sun and A. Ruediger, *Catal. Today*, 2021, **360**, 90–98.

211 X. Zhang, X. Wang, J. Chai, S. Xue, R. Wang, L. Jiang, J. Wang, Z. Zhang and D. D. Dionysiou, *Appl. Catal., B*, 2020, **272**, 119017.

212 L. Pan, S. Sun, Y. Chen, P. Wang, J. Wang, X. Zhang, J.-J. Zou and Z. L. Wang, *Adv. Energy Mater.*, 2020, **10**, 2000214.

213 X. Yu, S. Wang, X. Zhang, A. Qi, X. Qiao, Z. Liu, M. Wu, L. Li and Z. L. Wang, *Nano Energy*, 2018, **46**, 29–38.

214 E. Lin, Z. Kang, J. Wu, R. Huang, N. Qin and D. Bao, *Appl. Catal., B*, 2021, **285**, 119823.

215 S. Xu, L. Guo, Q. Sun and Z. L. Wang, *Adv. Funct. Mater.*, 2019, **29**, 1808737.

216 R. S. Hu, C. Li, X. Wang, Y. Sun, H. X. Jia, H. Q. Su and Y. L. Zhang, *Catal. Commun.*, 2012, **29**, 35–39.

217 R. Hailili, Z. Q. Wang, Y. X. Li, Y. H. Wang, V. K. Sharma, X. Q. Gong and C. Y. Wang, *Appl. Catal., B*, 2018, **221**, 422–432.

218 R. Hailili, Z. Q. Wang, X. Q. Gong and C. Y. Wang, *Appl. Catal., B*, 2019, **254**, 86–97.

219 J. Gopalakrishnan and V. Bhat, *Inorg. Chem.*, 1987, **26**, 4299–4301.

220 T. Takata, Y. Furumi, K. Shinohara, A. Tanaka, M. Hara, J. N. Kondo and K. Domen, *Chem. Mater.*, 1997, **9**, 1063–1064.

221 V. Kumar and S. U. Govind, *J. Hazard. Mater.*, 2011, **189**, 502–508.

222 L. Liu, W. Q. Cui, Y. H. Liang and F. L. Qiu, *Acta Chim. Sin.*, 2010, **68**, 211–216.

223 Y. H. Yang, Q. Y. Chen, Z. L. Yin and J. Li, *J. Alloys Compd.*, 2009, **488**, 364–369.

224 B. Wang, C. S. Li, D. Hirabayashi and K. Suzuki, *Int. J. Hydrogen Energy*, 2010, **35**, 3306–3312.

225 T. Oshima, T. Ichibha, K. Oqmhula, K. Hibino, H. Mogi, S. Yamashita, K. Fujii, Y. Miseki, K. Hongo, D. Lu, R. Maezono, K. Sayama, M. Yashima, K. Kimoto, H. Kato, M. Kakihana, H. Kageyama and K. Maeda, *Angew. Chem., Int. Ed.*, 2020, **59**, 9736–9743.

226 I. A. Rodionov, E. V. Mechtaeva, A. A. Burovikhina, O. I. Silyukov, M. A. Toikka and I. A. Zvereva, *Monatsh. Chem.*, 2018, **149**, 475–482.

227 H. Zhang, S. Ni, Y. L. Mi and X. X. Xu, *J. Catal.*, 2018, **359**, 112–121.

228 X. Q. Sun and X. X. Xu, *Appl. Catal., B*, 2017, **210**, 149–159.

229 X. Sun, Y. Mi, F. Jiao and X. Xu, *ACS Catal.*, 2018, **8**, 3209–3221.

230 Y. S. Jia, S. Shen, D. G. Wang, X. Wang, J. Y. Shi, F. X. Zhang, H. X. Han and C. Li, *J. Mater. Chem. A*, 2013, **1**, 7905–7912.

231 B. H. Park, B. S. Kang, S. D. Bu, T. W. Noh, J. Lee and W. Jo, *Nature*, 1999, **401**, 682–684.

232 W. Wei, Y. Dai and B. B. Huang, *J. Phys. Chem. C*, 2009, **113**, 5658–5663.

233 A. Kudo and S. Hijii, *Chem. Lett.*, 1999, 1103–1104.

234 Y. Liu, G. Zhu, J. Gao, M. Hojamberdiev, R. Zhu, X. Wei, Q. Guo and P. Liu, *Appl. Catal., B*, 2017, **200**, 72–82.

235 Z. W. Chen, H. Jiang, W. L. Jin and C. K. Shi, *Appl. Catal., B*, 2016, **180**, 698–706.

236 Z. W. Chen, X. Y. Jiang, C. B. Zhu and C. K. Shi, *Appl. Catal., B*, 2016, **199**, 241–251.

237 S. C. Tu, H. W. Huang, T. R. Zhang and Y. H. Zhanga, *Appl. Catal., B*, 2017, **219**, 550–562.

238 N. Li, J. J. Wu, H. B. Fang, X. H. Zhang, Y. Z. Zheng and X. Tao, *Appl. Surf. Sci.*, 2018, **448**, 41–49.

239 K. Das, D. Majhi, Y. P. Bhoi and B. G. Mishra, *Chem. Eng. J.*, 2019, **362**, 588–599.

240 X. Wang, Y. Wang, M. Gao, J. Shen, X. Pu, Z. Zhang, H. Lin and X. Wang, *Appl. Catal., B*, 2020, **270**, 118876.

241 Y. Guo, J. H. Li, Z. Q. Gao, X. Zhu, Y. Liu, Z. B. Wei, W. Zhao and C. Sun, *Appl. Catal., B*, 2016, **192**, 57–71.

242 A. Al-Keisy, L. Ren, X. Xu, W. C. Hao, S. X. Dou and Y. Du, *J. Phys. Chem. C*, 2019, **123**, 517–525.

243 R. Hailili, Z.-Q. Wang, M. Xu, Y. Wang, X.-Q. Gong, T. Xu and C. Wang, *J. Mater. Chem. A*, 2017, **5**, 21275–21290.

244 K. Wang, J. Li and G. Zhang, *ACS Appl. Mater. Interfaces*, 2019, **11**, 27686–27696.

245 L. Jiang, S. Ni, G. Liu and X. X. Xu, *Appl. Catal., B*, 2017, **217**, 342–352.

246 H. J. Yu, J. Y. Li, Y. H. Zhang, S. Q. Yang, K. L. Han, F. Dong, T. Y. Ma and H. W. Huang, *Angew. Chem., Int. Ed.*, 2019, **58**, 3880–3884.

247 D. W. Hwang, J. S. Lee, W. Li and S. H. Oh, *J. Phys. Chem. B*, 2003, **107**, 4963–4970.

248 R. Abe, M. Higashi, K. Sayama, Y. Abe and H. Sugihara, *J. Phys. Chem. B*, 2006, **110**, 2219–2226.

249 Z. Ma, Y. Li, Y. Lv, R. Sa, Q. Li and K. Wu, *ACS Appl. Mater. Interfaces*, 2018, **10**, 39327–39335.

250 X. Y. Cai, J. Y. Zhang, M. Fujitsuka and T. Majima, *Appl. Catal., B*, 2017, **202**, 191–198.

251 J. L. Li, Y. X. Zhao, M. Y. Xia, H. An, H. C. Bai, J. J. Wei, B. L. Yang and G. D. Yang, *Appl. Catal., B*, 2020, **261**, 118244.

252 Y. H. Ao, K. D. Wang, P. F. Wang, C. Wang and J. Hou, *Appl. Catal., B*, 2016, **194**, 157–168.

253 F. K. Meng, S. K. Cushing, J. T. Li, S. M. Hao and N. Q. Wu, *ACS Catal.*, 2015, **5**, 1949–1955.

254 M. S. Zhu, X. Y. Cai, M. Fujitsuka, J. Y. Zhang and T. Majima, *Angew. Chem., Int. Ed.*, 2017, **56**, 2064–2068.

255 R. Boppella, C. H. Choi, J. Moon and D. H. Kim, *Appl. Catal., B*, 2018, **239**, 178–186.

256 M. Oka, Y. Miseki, K. Saito and A. Kudo, *Appl. Catal., B*, 2015, **179**, 407–411.

257 K. Iizuka, T. Wato, Y. Miseki, K. Saito and A. Kudo, *J. Am. Chem. Soc.*, 2011, **133**, 20863–20868.

258 W. Kurashige, Y. Mori, S. Ozaki, M. Kawachi, S. Hossain, T. Kawawaki, C. J. Shearer, A. Iwase, G. F. Metha,

S. Yamazoe, A. Kudo and Y. Negishi, *Angew. Chem., Int. Ed.*, 2020, **59**, 7076–7082.
259 W. Kurashige, R. Kumazawa, D. Ishii, R. Hayashi, Y. Niihori, S. Hossain, L. V. Nair, T. Takayama, A. Iwase, S. Yamazoe, T. Tsukuda, A. Kudo and Y. Negishi, *J. Phys. Chem. C*, 2018, **122**, 13669–13681.
260 G. Catalan and J. F. Scott, *Adv. Mater.*, 2009, **21**, 2463–2485.
261 L. Qiao, S. Zhang, H. Y. Xiao, D. J. Singh, K. H. L. Zhang, Z. J. Liu, X. T. Zu and S. Li, *J. Mater. Chem. C*, 2018, **6**, 1239–1247.
262 S. Li, Y. H. Lin, B. P. Zhang, Y. Wang and C. W. Nan, *J. Phys. Chem. C*, 2010, **114**, 2903–2908.
263 Z. X. Li, Y. Shen, Y. H. Guan, Y. H. Hu, Y. H. Lin and C. W. Nan, *J. Mater. Chem. A*, 2014, **2**, 1967–1973.
264 Y. N. Huo, M. Miao, Y. Zhang, J. A. Zhu and H. X. Li, *Chem. Commun.*, 2011, **47**, 2089–2091.
265 Y. N. Feng, H. C. Wang, Y. Shen, Y. H. Lin and C. W. Nan, *Int. J. Appl. Ceram. Technol.*, 2014, **11**, 676–680.
266 Y. N. Feng, H. C. Wang, Y. D. Luo, Y. Shen and Y. H. Lin, *J. Appl. Phys.*, 2013, **113**, 146101.
267 C. Ponraj, G. Vinitha and J. Daniel, *Int. J. Green Energy*, 2019, **17**, 71–83.
268 W. W. Meng, R. S. Hu, J. Yang, Y. F. Du, J. J. Li and H. Y. Wang, *Chinese J. Catal.*, 2016, **37**, 1283–1292.
269 S. Irfan, S. Rizwan, Y. Shen, L. L. Li, A. Asfandiyar, S. Butt and C. W. Nan, *Sci. Rep.*, 2017, **7**, 42493.
270 A. Puhan, B. Bhushan, S. Satpathy, S. S. Meena, A. K. Nayak and D. Rout, *Appl. Surf. Sci.*, 2019, **493**, 593–604.
271 S. Irfan, L. L. Li, A. S. Saleemi and C. W. Nan, *J. Mater. Chem. A*, 2017, **5**, 11143–11151.
272 M. Umar, N. Mahmood, S. U. Awan, S. Fatima, A. Mahmood and S. Rizwan, *RSC Adv.*, 2019, **9**, 17148–17156.
273 Y. X. Yang, L. Kang and H. Li, *Ceram. Int.*, 2019, **45**, 8017–8022.
274 A. K. Vishwakarma, P. Tripathi, A. Srivastava, A. S. K. Sinha and O. N. Srivastava, *Int. J. Hydrogen Energy*, 2017, **42**, 22677–22686.
275 L. W. Lu, M. L. Lv, D. Wang, G. Liu and X. X. Xu, *Appl. Catal., B*, 2017, **200**, 412–419.
276 M. Humayun, A. Zada, Z. J. Li, M. Z. Xie, X. L. Zhang, Y. Qu, F. Raziq and L. Q. Jing, *Appl. Catal., B*, 2016, **180**, 219–226.
277 Y. L. Liu and J. M. Wu, *Nano Energy*, 2019, **56**, 74–81.
278 A. S. Zhu, Q. D. Zhao, X. Y. Li and Y. Shi, *ACS Appl. Mater. Interfaces*, 2014, **6**, 671–679.
279 Y. C. Yang, Y. Liu, J. H. Wei, C. X. Pan, R. Xiong and J. Shi, *RSC Adv.*, 2014, **4**, 31941–31947.
280 Y. L. Zhang, A. M. Schultz, P. A. Salvador and G. S. Rohrer, *J. Mater. Chem.*, 2011, **21**, 4168–4174.
281 T. Fan, C. C. Chen and Z. H. Tang, *RSC Adv.*, 2016, **6**, 9994–10000.
282 X. F. Wang, W. W. Mao, J. Zhang, Y. M. Han, C. Y. Quan, Q. X. Zhang, T. Yang, J. P. Yang, X. A. Li and W. Huang, *J. Colloid Interface Sci.*, 2015, **448**, 17–23.
283 X. Z. Deng, C. Song, Y. L. Tong, G. L. Yuan, F. Gao, D. Q. Liu and S. T. Zhang, *Phys. Chem. Chem. Phys.*, 2018, **20**, 3648–3657.
284 H. Sepahvand and S. Sharifnia, *Int. J. Hydrogen Energy*, 2019, **44**, 23658–23668.
285 S. Li, J. M. Zhang, M. G. Kibria, Z. T. Mi, M. Chaker, D. L. Ma, R. Nechache and F. Rosei, *Chem. Commun.*, 2013, **49**, 5856–5858.
286 F. Deganello, M. L. Tummino, C. Calabrese, M. L. Testa, P. Avetta, D. Fabbri, A. B. Prevot, E. Montoneri and G. Magnacca, *New J. Chem.*, 2015, **39**, 877–885.
287 S. Thirumalairajan, K. Girija, V. R. Mastelaro and N. Ponpandian, *New J. Chem.*, 2014, **38**, 5480–5490.
288 L. Li, M. Zhang, P. Tian, W. Gu and X. Wang, *Ceram. Int.*, 2014, **40**, 13813–13817.
289 M. Ghaffari, P. Y. Tan, M. E. Oruc, O. K. Tan, M. S. Tse and M. Shannon, *Catal. Today*, 2011, **161**, 70–77.
290 S. Afzal, X. Quan and J. L. Zhang, *Appl. Catal., B*, 2017, **206**, 692–703.
291 M. Humayun, N. Sun, F. Raziq, X. L. Zhang, R. Yan, Z. J. Li, Y. Qu and L. Q. Jing, *Appl. Catal., B*, 2018, **231**, 23–33.
292 P. Garcia-Munoz, F. Fresno, C. Lefevre, D. Robert and N. Keller, *Appl. Catal., B*, 2020, **262**, 118310.
293 K. Xu and J. Feng, *RSC Adv.*, 2017, **7**, 45369–45376.
294 Y. Wu, H. Wang, W. Tu, Y. Liu, Y. Z. Tan, X. Z. Yuan and J. W. Chew, *J. Hazard. Mater.*, 2018, **347**, 412–422.
295 M. Mishra, I. Mukherjee, A. K. Mall, A. Mitra, S. Dash, S. Chatterjee, S. Mukherjee and A. Roy, *J. Mater. Chem. A*, 2018, **6**, 13467.
296 J. W. Liu, G. Chen, Z. H. Li and Z. G. Zhang, *Int. J. Hydrogen Energy*, 2007, **32**, 2269–2272.
297 H. F. Shi, C. L. Zhang, C. P. Zhou and G. Q. Chen, *RSC Adv.*, 2015, **5**, 93615–93622.
298 T. T. Zhang, K. Zhao, J. G. Yu, J. Jin, Y. Qi, H. Q. Li, X. J. Hou and G. Liu, *Nanoscale*, 2013, **5**, 8375–8383.
299 T. T. Zhang, W. Y. Lei, P. Liu, J. A. Rodriguez, J. G. Yu, Y. Qi, G. Liu and M. H. Liu, *Chem. Sci.*, 2015, **6**, 4118–4123.
300 J. Y. Lan, X. M. Zhou, G. Liu, J. G. Yu, J. C. Zhang, L. J. Zhi and G. J. Nie, *Nanoscale*, 2011, **3**, 5161–5167.
301 R. W. Wang, Y. F. Zhu, Y. F. Qiu, C. F. Leung, J. He, G. J. Liu and T. C. Lau, *Chem. Eng. J.*, 2013, **226**, 123–130.
302 J. X. Yu, Z. G. Chen, L. Zeng, Y. Y. Ma, Z. Feng, Y. Wu, H. J. Lin, L. H. Zhao and Y. M. He, *Sol. Energy Mater. Sol. Cells*, 2018, **179**, 45–56.
303 P. X. Xing, S. J. Wu, Y. J. Chen, P. F. Chen, X. Hu, H. J. Lin, L. H. Zhao and Y. M. He, *ACS Sustainable Chem. Eng.*, 2019, **7**, 12408–12418.
304 E. K. Piggott, T. O. Hope, B. W. Crabbe, P.-M. Jalbert, G. Orlova and G. L. Hallett-Tapley, *Catal. Sci. Technol.*, 2017, **7**, 5758–5765.
305 P. Zhang, Y. Q. Shen, W. J. Wu, J. Li and Z. X. Zhou, *Appl. Surf. Sci.*, 2018, **434**, 932–939.
306 X. Q. Li, T. Y. Zhang, S. W. Gu, S. Z. Kang, G. D. Li and J. Mu, *Sep. Purif. Technol.*, 2013, **108**, 139–142.
307 Z. Hong, X. Q. Li, S. Z. Kang, L. X. Qin, G. D. Li and J. Mu, *Int. J. Hydrogen Energy*, 2015, **40**, 14297–14304.
308 S. F. Jia, Y. P. Su, B. P. Zhang, Z. C. Zhao, S. Li, Y. F. Zhang, P. C. Li, M. Y. Xu and R. Ren, *Nanoscale*, 2019, **11**, 7690–7700.

 This journal is © The Royal Society of Chemistry 2021

309 Z. Qu, J. Wang, J. Tang, X. Shu, X. Liu, Z. Zhang and J. Wang, *Mol. Catal.*, 2018, **445**, 1–11.
310 P. Li, S. X. Ouyang, G. C. Xi, T. Kako and J. H. Ye, *J. Phys. Chem. C*, 2012, **116**, 7621–7628.
311 Y. Huan, X. H. Wang, W. C. Hao and L. T. Li, *RSC Adv.*, 2015, **5**, 72410–72415.
312 P. Li, H. Xu, L. Q. Liu, T. Kako, N. Umezawa, H. Abe and J. H. Ye, *J. Mater. Chem. A*, 2014, **2**, 5606–5609.
313 A. S. Vig, N. Rani, A. Gupta and O. P. Pandey, *Sol. Energy*, 2019, **185**, 469–479.
314 F. L. Yang, Q. Zhang, L. Zhang, M. T. Cao, Q. Q. Liu and W. L. Dai, *Appl. Catal., B*, 2019, **257**, 117901.
315 F. Opoku, K. K. Govender, C. G. C. E. van Sittert and P. P. Govender, *Carbon*, 2018, **136**, 187–195.
316 H. F. Shi, G. Q. Chen, C. L. Zhang and Z. G. Zou, *ACS Catal.*, 2014, **4**, 3637–3643.
317 C. J. Song, M. S. Fan, B. Hu, T. J. Chen, L. P. Wang and W. D. Shi, *CrystEngComm*, 2015, **17**, 4575–4583.
318 M. Sun, Q. Yan, Y. Shao, C. Q. Wang, T. Yan, P. G. Ji and B. Du, *Appl. Surf. Sci.*, 2017, **416**, 288–295.
319 S. Kumar, T. Malik, D. Sharma and A. K. Ganguli, *ACS Appl. Nano Mater.*, 2019, **2**, 2651–2662.
320 S. F. Chen, L. Ji, W. M. Tang and X. L. Fu, *Dalton Trans.*, 2013, **42**, 10759–10768.
321 S. Li, Z. Liu, Z. Qu, C. Piao, J. Liu, D. Xu, X. Li, J. Wang and Y. Song, *J. Photochem. Photobiol. A: Chem.*, 2020, **389**, 112246.
322 H. Kato, H. Kobayashi and A. Kudo, *J. Phys. Chem. B*, 2002, **106**, 12441–12447.
323 B. Gao, D. Hu, C. Xiao, D. Li, B. Lin, Y. Chen and Y. Zheng, *J. Phys. Chem. Solids*, 2019, **135**, 109083.
324 L. F. Yang, J. B. Liu, H. B. Chang and S. S. Tang, *RSC Adv.*, 2015, **5**, 59970–59975.
325 C. Wang, J. Yan, X. Y. Wu, Y. H. Song, G. B. Cai, H. Xu, J. X. Zhu and H. M. Li, *Appl. Surf. Sci.*, 2013, **273**, 159–166.
326 P. F. Chen, P. X. Xing, Z. Q. Chen, X. Hu, H. J. Lin, L. H. Zhao and Y. M. He, *J. Colloid Interface Sci.*, 2019, **534**, 163–171.
327 Z. Z. Yu, B. W. Zhan, B. H. Ge, Y. T. Zhu, Y. Dai, G. J. Zhou, F. P. Yu, P. Wang, B. B. Huang and J. Zhan, *Appl. Surf. Sci.*, 2019, **488**, 485–493.
328 A. Kudo, H. Kato and S. Nakagawa, *J. Phys. Chem. B*, 2000, **104**, 571–575.
329 D. Chen and J. H. Ye, *Chem. Mater.*, 2009, **21**, 2327–2333.
330 I. S. Cho, S. Lee, J. H. Noh, D. W. Kim, D. K. Lee, H. S. Jung, D. W. Kim and K. S. Hong, *J. Mater. Chem.*, 2010, **20**, 3979–3983.
331 R. Pang, K. Teramura, H. Asakura, S. Hosokawa and T. Tanaka, *Appl. Catal., B*, 2017, **218**, 770–778.
332 H. Fukuoka, T. Isami and S. Yamanaka, *J. Solid State Chem.*, 2000, **151**, 40–45.
333 S. Ida, Y. Okamoto, S. Koga, H. Hagiwara and T. Ishihara, *RSC Adv.*, 2013, **3**, 11521–11524.
334 Y. N. Zhou, T. Wen, Y. Z. Guo, B. C. Yang and Y. G. Wang, *RSC Adv.*, 2016, **6**, 64930–64936.
335 Y. Ebina, N. Sakai and T. Sasaki, *J. Phys. Chem. B*, 2005, **109**, 17212–17216.
336 H. Hata, Y. Kobayashi, V. Bojan, W. J. Youngblood and T. E. Mallouk, *Nano Lett.*, 2008, **8**, 794–799.
337 T. Oshima, D. L. Lu, O. Ishitani and K. Maeda, *Angew. Chem., Int. Ed.*, 2015, **54**, 2698–2702.
338 Y. Miseki, H. Kato and A. Kudo, *Chem. Lett.*, 2006, 1052–1053.
339 S. J. Li, W. B. Cao, C. D. Wang and H. Qiu, *J. Alloys Compd.*, 2015, **644**, 757–762.
340 K. Wang, Y. Li, J. Li and G. Zhang, *Appl. Catal., B*, 2020, **263**, 117730.
341 N. Zhang, R. Ciriminna, M. Pagliaro and Y. J. Xu, *Chem. Soc. Rev.*, 2014, **43**, 5276–5287.
342 T. Saison, P. Gras, N. Chemin, C. Chaneac, O. Durupthy, V. Brezova, C. Colbeau-Justin and J. P. Jolivet, *J. Phys. Chem. C*, 2013, **117**, 22656–22666.
343 B. S. Li, C. Lai, G. M. Zeng, L. Qin, H. Yi, D. L. Huang, C. Y. Zhou, X. G. Liu, M. Cheng, P. Xu, C. Zhang, F. L. Huang and S. Y. Liu, *ACS Appl. Mater. Interfaces*, 2018, **10**, 18824–18836.
344 H. R. Zhou, Z. P. Wen, J. Liu, J. Ke, X. G. Duan and S. B. Wang, *Appl. Catal., B*, 2019, **242**, 76–84.
345 S. J. Liu, Y. F. Hou, S. L. Zheng, Y. Zhang and Y. Wang, *CrystEngComm*, 2013, **15**, 4124–4130.
346 G. J. Dong, Y. J. Zhang and Y. P. Bi, *J. Mater. Chem. A*, 2017, **5**, 20594–20597.
347 A. P. Jakhade, M. V. Biware and R. C. Chikate, *ACS Omega*, 2017, **2**, 7219–7229.
348 Y. H. Zhang, N. Zhang, Z. R. Tang and Y. J. Xu, *Chem. Sci.*, 2013, **4**, 1820–1824.
349 Y. H. Zhang and Y. J. Xu, *RSC Adv.*, 2014, **4**, 2904–2910.
350 H. Lv, Y. M. Liu, J. Guang, Z. W. Ding and J. J. Wang, *RSC Adv.*, 2016, **6**, 80226–80233.
351 M. Zargazi and M. H. Entezari, *Appl. Catal., B*, 2019, **242**, 507–517.
352 H. W. Huang, C. Zhou, X. C. Jiao, H. F. Yuan, J. W. Zhao, C. Q. He, J. Hofkens, M. B. J. Roeffaers, J. L. Long and J. A. Steele, *ACS Catal.*, 2020, **10**, 1439–1443.
353 Y. Liu, D. Shen, Q. Zhang, Y. Lin and F. Peng, *Appl. Catal., B*, 2021, **283**, 119630.
354 H. Yi, M. Yan, D. L. Huang, G. M. Zeng, C. Lai, M. F. Li, X. Q. Huo, L. Qin, S. Y. Liu, X. G. Liu, B. S. Li, H. Wang, M. C. Shen, Y. K. Fu and X. Y. Guo, *Appl. Catal., B*, 2019, **250**, 52–62.
355 L. W. Zhang and D. Bahnemann, *ChemSusChem*, 2013, **6**, 283–290.
356 F. Z. Ren, J. H. Zhang and Y. X. Wang, *RSC Adv.*, 2015, **5**, 29058–29065.
357 H. Tian, Y. F. Wang, Y. Liu, X. G. Xi, J. C. Zhao and B. X. Jiao, *Chinese J. Struc. Chem.*, 2017, **36**, 751–760.
358 M. Wang, Z. Y. Qiao, M. H. Fang, Z. H. Huang, Y. G. Liu, X. W. Wu, C. Tang, H. Tang and H. K. Zhu, *RSC Adv.*, 2015, **5**, 94887–94894.
359 H. W. Huang, K. Liu, K. Chen, Y. L. Zhang, Y. H. Zhang and S. C. Wang, *J. Phys. Chem. C*, 2014, **118**, 14379–14387.
360 F. Z. Wang, W. J. Li, S. N. Gu, H. D. Li, X. Wu and X. T. Liu, *Chem. – Eur. J.*, 2016, **22**, 12859–12867.

361 T. Hu, H. Li, N. Du and W. Hou, *ChemCatChem*, 2018, **10**, 3040–3048.
362 J. Yang, X. H. Wang, Y. M. Chen, J. Dai and S. H. Sun, *RSC Adv.*, 2015, **5**, 9771–9782.
363 D. Sun, Y. Le, C. J. Jiang and B. Cheng, *Appl. Surf. Sci.*, 2018, **441**, 429–437.
364 Q. S. Wu, Y. Cui, L. M. Yang, G. Y. Zhang and D. Z. Gao, *Sep. Purif. Technol.*, 2015, **142**, 168–175.
365 J. G. Wang, H. Liang, C. Zhang, B. Jin and Y. Men, *Appl. Catal., B*, 2019, **256**, 117874.
366 X. Cao, Z. Chen, R. Lin, W.-C. Cheong, S. Liu, J. Zhang, Q. Peng, C. Chen, T. Han, X. Tong, Y. Wang, R. Shen, W. Zhu, D. Wang and Y. Li, *Nat. Catal.*, 2018, **1**, 704–710.
367 J. D. Hu, D. Y. Chen, Z. Mo, N. J. Li, Q. F. Xu, H. Li, J. H. He, H. Xu and J. M. Lu, *Angew. Chem., Int. Ed.*, 2019, **58**, 2073–2077.
368 Y. W. Teh, Y. W. Goh, X. Y. Kong, B. J. Ng, S. T. Yong and S. P. Chai, *ChemCatChem*, 2019, **11**, 6431–6438.
369 X. Y. Gu, Q. Wang, D. P. Zhang, X. X. Geng, Z. X. Zha, Y. Li, J. Yang and S. H. Cui, *J. Nanosci. Nanotechnol.*, 2020, **20**, 3105–3116.
370 L. Yuan, B. Weng, J. C. Colmenares, Y. G. Sun and Y. J. Xu, *Small*, 2017, **13**, 1702253.
371 S. W. Cao, B. J. Shen, T. Tong, J. W. Fu and J. G. Yu, *Adv. Funct. Mater.*, 2018, **28**, 1800136.
372 H. B. Yu, L. B. Jiang, H. Wang, B. B. Huang, X. Z. Yuan, J. H. Huang, J. Zhang and G. M. Zeng, *Small*, 2019, **15**, 1901008.
373 Y. Shimodaira, H. Kato, H. Kobayashi and A. Kudo, *J. Phys. Chem. B*, 2006, **110**, 17790–17797.
374 D. M. Chen, Q. Hao, Z. H. Wang, H. Ding and Y. F. Zhu, *CrystEngComm*, 2016, **18**, 1976–1986.
375 K. Q. Jing, J. H. Xiong, N. Qin, Y. J. Song, L. Y. Li, Y. Yu, S. J. Liang and L. Wu, *Chem. Commun.*, 2017, **53**, 8604–8607.
376 Y. L. Jia, Y. Ma, J. Z. Tang and W. B. Shi, *Dalton Trans.*, 2018, **47**, 5542–5547.
377 Y. Y. Xie, X. T. Shang, D. Liu, H. B. Zhao, Y. Y. Gu, Z. Z. Zhang and X. X. Wang, *Appl. Catal., B*, 2019, **259**, 118087.
378 S. G. Li, L. Q. Bai, N. Ji, S. X. Yu, S. Lin, N. Tian and H. W. Huang, *J. Mater. Chem. A*, 2020, **8**, 9268–9277.
379 G. Yang, Y.-A. Zhu, Y. Liang, J. Yang, K. Wang, Z. Zeng, R. Xu and X. Xie, *Appl. Surf. Sci.*, 2021, **539**, 148038.
380 X. L. Yang, S. Y. Wang, N. Yang, W. Zhou, P. Wang, K. Jiang, S. Li, H. Song, X. Ding, H. Chen and J. H. Ye, *Appl. Catal., B*, 2019, **259**, 118088.
381 X. Xu, X. Ding, X. L. Yang, P. Wang, S. Li, Z. X. Lu and H. Chen, *J. Hazard. Mater.*, 2019, **364**, 691–699.
382 K. Q. Jing, W. Ma, Y. H. Ren, J. H. Xiong, B. B. Guo, Y. J. Song, S. J. Liang and L. Wu, *Appl. Catal., B*, 2019, **243**, 10–18.
383 F. Fu, H. D. Shen, X. Sun, W. W. Xue, A. Shoneye, J. N. Ma, L. Luo, D. J. Wang, J. G. Wang and J. W. Tang, *Appl. Catal., B*, 2019, **247**, 150–162.
384 Z. Dai, F. Qin, H. P. Zhao, J. Ding, Y. L. Liu and R. Chen, *ACS Catal.*, 2016, **6**, 3180–3192.
385 X. B. Zhang, L. Zhang, J. S. Hu and X. H. Huang, *RSC Adv.*, 2016, **6**, 32349–32357.
386 D. P. Dutta, A. Ballal, S. Chopade and A. Kumar, *J. Photochem. Photobiol. A: Chem.*, 2017, **346**, 105–112.
387 X. X. Li, S. M. Fang, L. Ge, C. C. Han, P. Qiu and W. L. Liu, *Appl. Catal., B*, 2015, **176**, 62–69.
388 R. X. Yang, F. Dong, X. You, M. Liu, S. Zhong, L. S. Zhang and B. J. Liu, *Mater. Lett.*, 2019, **252**, 272–276.
389 J. L. Zhang, H. Liu and Z. Ma, *J. Mol. Catal. A: Chem.*, 2016, **424**, 37–44.
390 X. Du, J. N. Wan, J. Jia, C. Pan, X. Hu, J. N. Fan and E. N. Liu, *Mater. Des.*, 2017, **119**, 113–123.
391 S. Jonjana, A. Phuruangrat, S. Thongtem, O. Wiranwetchayan and T. Thongtem, *Mater. Lett.*, 2016, **180**, 93–96.
392 F. Ding, P. Chen, F. Liu, L. Chen, J.-K. Guo, S. Shen, Q. Zhang, L.-H. Meng, C.-T. Au and S.-F. Yin, *Appl. Surf. Sci.*, 2019, **490**, 102–108.
393 L.-N. Song, F. Ding, Y.-K. Yang, D. Ding, L. Chen, C.-T. Au and S.-F. Yin, *ACS Sustainable Chem. Eng.*, 2018, **6**, 17044–17050.
394 J. Yang, X. J. Niu, S. R. An, W. Y. Chen, J. Wang and W. Liu, *RSC Adv.*, 2017, **7**, 2943–2952.
395 J. L. Lv, J. F. Zhang, J. Liu, Z. Li, K. Dai and C. H. Liang, *ACS Sustainable Chem. Eng.*, 2018, **6**, 696–706.
396 X. Lin, J. Hou, S. S. Jiang, Z. Lin, M. Wang and G. B. Che, *RSC Adv.*, 2015, **5**, 104815–104821.
397 J. L. Liang, F. Y. Liu, J. Deng, M. Li and M. P. Tong, *Water Res.*, 2017, **123**, 632–641.
398 J. S. Cai, J. Y. Huang and Y. K. Lai, *J. Mater. Chem. A*, 2017, **5**, 16412–16421.
399 D. J. Wang, H. D. Shen, L. Guo, C. Wang, F. Fu and Y. C. Liang, *Appl. Surf. Sci.*, 2018, **436**, 536–547.
400 C. P. Udawatte, M. Kakihana and M. Yoshimura, *Solid State Ionics*, 2000, **128**, 217–226.
401 O. I. Prokopalo, *Ferroelectrics*, 1976, **14**, 683–685.
402 T. Ishihara, H. Fujita, H. Nishiguchi and Y. Takita, *Sens. Actuators, B*, 2000, **65**, 319–324.
403 W. J. Wang, S. J. Liang, K. N. Ding, J. H. Bi, J. C. Yu, P. K. Wong and L. Wu, *J. Mater. Sci.*, 2014, **49**, 1893–1902.
404 H. B. Sales, V. Bouquet, S. Deputier, S. Ollivier, F. Gouttefangeas, M. Guilloux-Viry, V. Dorcet, I. T. Weber, A. G. de Souza and I. M. G. dos Santos, *Solid State Sci.*, 2014, **28**, 67–73.
405 S. Moshtaghi, S. Gholamrezaei and M. S. Niasari, *J. Mol. Struct.*, 2017, **1134**, 511–519.
406 D. Chen and J. H. Ye, *Chem. Mater.*, 2007, **19**, 4585–4591.
407 T. Alammar, I. Hamm, V. Grasmik, M. Wark and A. V. Mudring, *Inorg. Chem.*, 2017, **56**, 6920–6932.
408 C. W. Lee, D. W. Kim, I. S. Cho, S. Park, S. S. Shin, S. W. Seo and K. S. Hong, *Int. J. Hydrogen Energy*, 2012, **37**, 10557–10563.
409 X. H. Zhang, J. D. Hu, Y. L. Cao, J. Xie, W. Jia, S. Q. Wang and D. Z. Jia, *Chem. – Eur. J.*, 2018, **24**, 14111–14118.
410 X. H. Zhang, A. J. Liu, Y. L. Cao, J. Xie, W. Jia and D. Z. Jia, *New J. Chem.*, 2019, **43**, 10965–10972.
411 W. F. Zhang, J. W. Tang and J. H. Ye, *J. Mater. Res.*, 2007, **22**, 1859–1871.

 This journal is © The Royal Society of Chemistry 2021

412 H. Mizoguchi, P. Chen, P. Boolchand, V. Ksenofontov, C. Felser, P. W. Barnes and P. M. Woodward, *Chem. Mater.*, 2013, **25**, 3858–3866.
413 K. F. Moura, L. Chantelle, D. Rosendo, E. Longo and I. M. G. dos Santos, *Mater. Res-Ibero-Am. J.*, 2017, **20**, 317–324.
414 B. Hadjarab, A. Bouguelia, A. Benchettara and A. Trari, *J. Alloys Compd.*, 2008, **461**, 360–366.
415 M. Kim, B. Lee, H. Ju, J. Y. Kim, J. Kim and S. W. Leek, *Adv. Mater.*, 2019, **31**, 1903316.
416 T. Alammar, I. I. Slowing, J. Anderegg and A. V. Mudring, *ChemSusChem*, 2017, **10**, 3387–3401.
417 Y. P. Yuan, X. L. Zhang, L. F. Liu, X. J. Jiang, J. Lv, Z. S. Li and Z. G. Zou, *Int. J. Hydrogen Energy*, 2008, **33**, 5941–5946.
418 Y. P. Yuan, Z. Y. Zhao, J. Zheng, M. Yang, L. G. Qiu, Z. S. Li and Z. G. Zou, *J. Mater. Chem.*, 2010, **20**, 6772–6779.
419 T. Chen, J. Meng, Q. Y. Lin, X. Wei, J. X. Li and Z. Zhang, *J. Alloys Compd.*, 2019, **780**, 498–503.
420 J. Meng, Z. Y. Lan, Q. Y. Lin, T. Chen, X. Chen, X. Wei, Y. H. Lu, J. X. Li and Z. Zhang, *J. Mater. Sci.*, 2019, **54**, 1967–1976.
421 J. Meng, X. Q. Fu, K. Du, X. Chen, Q. Y. Lin, X. Wei, J. X. Li and Z. Zhang, *Int. J. Hydrogen Energy*, 2018, **43**, 9224–9232.
422 A. S. Patra, M. S. Chauhan, S. Keene, G. Gogoi, K. A. Reddy, S. Ardo, D. L. V. K. Prasad and M. Qureshi, *J. Phys. Chem. C*, 2019, **123**, 233–249.
423 R. Borja-Urby, L. A. Diaz-Torres, I. Garcia-Martinez, D. Bahena-Uribe, G. Casillas, A. Ponce and M. Jose-Yacaman, *Catal. Today*, 2015, **250**, 95–101.
424 M. H. Wu, M. P. Luo, M. X. Guo and L. S. Jia, *ACS Sustainable Chem. Eng.*, 2017, **5**, 11558–11565.
425 J. L. Xu, C. F. Sun, Z. Y. Wang, Y. D. Hou, Z. X. Ding and S. B. Wang, *Chem. – Eur. J.*, 2018, **24**, 18512–18517.
426 C. Chen, J. L. Zhou, J. F. Geng, R. Y. Bao, Z. H. Wang, J. X. Xia and H. Li, *Appl. Surf. Sci.*, 2020, **503**, 144287.
427 J. Luo, J. Chen, R. Guo, Y. Qiu, W. Li, X. Zhou, X. Ning and L. Zhan, *Sep. Purif. Technol.*, 2019, **211**, 882–894.
428 T. K. Dhiman and S. Singh, *Phys. Status Solidi A*, 2019, **216**, 1900012.
429 M. Touboul, J. Lokaj, L. Tessier, V. Kettman and V. Vrabel, *Acta Crystallogr. Sect. C: Cryst. Struct. Commun.*, 1992, **48**, 1176–1179.
430 C. D. Lv, G. Chen, J. X. Sun, Y. S. Zhou, S. Fan and C. M. Zhang, *Appl. Catal., B*, 2015, **179**, 54–60.
431 Y. Peng, K. K. Wang, T. Liu, J. Xu and B. Xu, *Appl. Catal., B*, 2017, **203**, 946–954.
432 X.-J. Wen, L. Qian, X.-X. Lv, J. Sun, J. Guo, Z.-H. Fei and C.-G. Niu, *J. Hazard. Mater.*, 2020, **385**, 121508.
433 C. N. Ri, S. G. Kim, K. S. Ju, H. S. Ryo, C. H. Mun and U. H. Kim, *RSC Adv.*, 2018, **8**, 5433–5440.
434 C. N. Ri, K. Song-Gol, J. Ju-Yong, S. N. Pak, S. C. Ri and J. H. Ri, *New J. Chem.*, 2018, **42**, 647–653.
435 W. S. dos Santos, M. Rodriguez, A. S. Afonso, J. P. Mesquita, L. L. Nascimento, A. O. T. Patrocinio, A. C. Silva, L. C. A. Oliveira, J. D. Fabris and M. C. Pereira, *Sci. Rep.*, 2016, **6**, 31406.
436 M. J. Liang, Z. Y. Yang, Y. Mei, H. R. Zhou and S. J. Yang, *Nano*, 2018, **13**, 1850028.
437 X. Zhao, Z. Duan and L. Chen, *Ind. Eng. Chem. Res.*, 2019, **58**, 10402–10409.
438 M. Cheng, C. Xiao and Y. Xie, *J. Mater. Chem. A*, 2019, **7**, 19616–19633.
439 C. D. Lv, G. Chen, J. X. Sun and Y. S. Zhou, *Inorg. Chem.*, 2016, **55**, 4782–4789.
440 K. Shantha and K. B. R. Varma, *Mater. Sci. Eng., B*, 1999, **60**, 66–75.
441 E. Alarcon-Llado, L. Chen, M. Hettick, N. Mashouf, Y. J. Lin, A. Javey and J. W. Ager, *Phys. Chem. Chem. Phys.*, 2014, **16**, 1651–1657.
442 H. Mai, T. Lu, Q. Sun, R. G. Elliman, F. Kremer, T. Duong, K. Catchpole, Q. Li, Z. Yi, T. J. Frankcombe and Y. Liu, *Mater. Horiz.*, 2020, **7**, 898–904.
443 D. E. Scaife, *Sol. Energy*, 1980, **25**, 41–54.
444 J. Chen, C. Dong, H. Idriss, O. F. Mohammed and O. M. Bakr, *Adv. Energy Mater.*, 2020, **10**, 1902433.
445 S. Klejna, T. Mazur, E. Wlaźlak, P. Zawal, H. S. Soo and K. Szaciłowski, *Coord. Chem. Rev.*, 2020, **415**, 213316.
446 A. Kojima, K. Teshima, Y. Shirai and T. Miyasaka, *J. Am. Chem. Soc.*, 2009, **131**, 6050–6051.
447 L. Dou, Y. Yang, J. You, Z. Hong, W.-H. Chang, G. Li and Y. Yang, *Nat. Commun.*, 2014, **5**, 5404.
448 D. Shi, V. Adinolfi, R. Comin, M. Yuan, E. Alarousu, A. Buin, Y. Chen, S. Hoogland, A. Rothenberger, K. Katsiev, Y. Losovyj, X. Zhang, P. A. Dowben, O. F. Mohammed, E. H. Sargent and O. M. Bakr, *Science*, 2015, **347**, 519–522.
449 H. Zhu, Y. Fu, F. Meng, X. Wu, Z. Gong, Q. Ding, M. V. Gustafsson, M. T. Trinh, S. Jin and X. Y. Zhu, *Nat. Mater.*, 2015, **14**, 636–642.
450 Y. Fu, H. Zhu, C. C. Stoumpos, Q. Ding, J. Wang, M. G. Kanatzidis, X. Zhu and S. Jin, *ACS Nano*, 2016, **10**, 7963–7972.
451 Y. Cao, N. Wang, H. Tian, J. Guo, Y. Wei, H. Chen, Y. Miao, W. Zou, K. Pan, Y. He, H. Cao, Y. Ke, M. Xu, Y. Wang, M. Yang, K. Du, Z. Fu, D. Kong, D. Dai, Y. Jin, G. Li, H. Li, Q. Peng, J. Wang and W. Huang, *Nature*, 2018, **562**, 249–253.
452 J. Luo, X. Wang, S. Li, J. Liu, Y. Guo, G. Niu, L. Yao, Y. Fu, L. Gao, Q. Dong, C. Zhao, M. Leng, F. Ma, W. Liang, L. Wang, S. Jin, J. Han, L. Zhang, J. Etheridge, J. Wang, Y. Yan, E. H. Sargent and J. Tang, *Nature*, 2018, **563**, 541–545.
453 F. Zhang and K. Zhu, *Adv. Energy Mater.*, 2020, **10**, 1902579.
454 C. Wehrenfennig, G. E. Eperon, M. B. Johnston, H. J. Snaith and L. M. Herz, *Adv. Mater.*, 2014, **26**, 1584–1589.
455 T. M. Brenner, D. A. Egger, L. Kronik, G. Hodes and D. Cahen, *Nat. Rev. Mater.*, 2016, **1**, 15007.
456 L. M. Herz, *Annu. Rev. Phys. Chem.*, 2016, **67**, 65–89.
457 S. Makuta, M. Liu, M. Endo, H. Nishimura, A. Wakamiya and Y. Tachibana, *Chem. Commun.*, 2016, **52**, 673–676.
458 M. Liu, M. Endo, A. Shimazaki, A. Wakamiya and Y. Tachibana, *ACS Appl. Energy Mater.*, 2018, **1**, 3722–3732.
459 Y. Fu, H. Zhu, J. Chen, M. P. Hautzinger, X. Y. Zhu and S. Jin, *Nat. Rev. Mater.*, 2019, **4**, 169–188.
460 N. K. Noel, S. D. Stranks, A. Abate, C. Wehrenfennig, S. Guarnera, A.-A. Haghighirad, A. Sadhanala, G. E. Eperon,

S. K. Pathak, M. B. Johnston, A. Petrozza, L. M. Herz and H. J. Snaith, *Energy Environ. Sci.*, 2014, **7**, 3061–3068.
461 M. Leng, Z. Chen, Y. Yang, Z. Li, K. Zeng, K. Li, G. Niu, Y. He, Q. Zhou and J. Tang, *Angew. Chem., Int. Ed.*, 2016, **55**, 15012–15016.
462 L. Zhou, J.-F. Liao, Z.-G. Huang, J.-H. Wei, X.-D. Wang, W.-G. Li, H.-Y. Chen, D.-B. Kuang and C.-Y. Su, *Angew. Chem., Int. Ed.*, 2019, **58**, 5277–5281.
463 A. K. Jena, A. Kulkarni and T. Miyasaka, *Chem. Rev.*, 2019, **119**, 3036–3103.
464 Z. Xiao, Z. Song and Y. Yan, *Adv. Mater.*, 2019, **31**, 1803792.
465 S. T. Umedov, D. B. Khadka, M. Yanagida, A. Grigorieva and Y. Shirai, *Sol. Energy Mater. Sol. Cells*, 2021, **230**, 111180.
466 F. Reyes-Pérez, J. J. Gallardo, T. Aguilar, R. Alcántara, C. Fernández-Lorenzo and J. Navas, *ChemistrySelect*, 2018, **3**, 10226–10235.
467 D. X. Ju, X. P. Zheng, J. L. Liu, Y. Chen, J. Zhang, B. Q. Cao, H. Xiao, O. F. Mohammed, O. M. Bakr and X. T. Tao, *Angew. Chem., Int. Ed.*, 2018, **57**, 14868–14872.
468 W. Zhang, Q. Zhao, X. Wang, X. Yan, J. Xu and Z. Zeng, *Catal. Sci. Technol.*, 2017, **7**, 2753–2762.
469 X.-D. Wang, Y.-H. Huang, J.-F. Liao, Y. Jiang, L. Zhou, X.-Y. Zhang, H.-Y. Chen and D.-B. Kuang, *J. Am. Chem. Soc.*, 2019, **141**, 13434–13441.
470 Y. Cai, W. Xie, H. Ding, Y. Chen, K. Thirumal, L. H. Wong, N. Mathews, S. G. Mhaisalkar, M. Sherburne and M. Asta, *Chem. Mater.*, 2017, **29**, 7740–7749.
471 D. B. Khadka, Y. Shirai, M. Yanagida and K. Miyano, *J. Mater. Chem. C*, 2019, **7**, 8335–8343.
472 Y. Guo, G. Liu, Z. Li, Y. Lou, J. Chen and Y. Zhao, *ACS Sustainable Chem. Eng.*, 2019, **7**, 15080–15085.
473 J.-H. Chang, T. Doert and M. Ruck, *Z. Anorg. Allg. Chem.*, 2016, **642**, 736–748.
474 S. S. Bhosale, A. K. Kharade, E. Jokar, A. Fathi, S.-M. Chang and E. W.-G. Diau, *J. Am. Chem. Soc.*, 2019, **141**, 20434–20442.
475 Z.-L. Liu, R.-R. Liu, Y.-F. Mu, Y.-X. Feng, G.-X. Dong, M. Zhang and T.-B. Lu, *Sol. RRL*, 2021, **5**, 2000691.
476 B.-M. Bresolin, C. Günnemann, D. W. Bahnemann and M. Sillanpää, *Nanomaterials*, 2020, **10**, 763.
477 B.-M. Bresolin, P. Sgarbossa, D. W. Bahnemann and M. Sillanpää, *Sep. Purif. Technol.*, 2020, **251**, 117320.
478 B.-M. Bresolin, N. O. Balayeva, L. I. Granone, R. Dillert, D. W. Bahnemann and M. Sillanpää, *Sol. Energy Mater. Sol. Cells*, 2020, **204**, 110214.
479 Y. Dai and H. Tüysüz, *ChemSusChem*, 2019, **12**, 2587–2592.
480 Y. Dai, C. Poidevin, C. Ochoa-Hernández, A. A. Auer and H. Tüysüz, *Angew. Chem., Int. Ed.*, 2020, **59**, 5788–5796.
481 M. Shi, G. Li, W. Tian, S. Jin, X. Tao, Y. Jiang, E. A. Pidko, R. Li and C. Li, *Adv. Mater.*, 2020, **32**, 2002137.
482 A. H. Slavney, T. Hu, A. M. Lindenberg and H. I. Karunadasa, *J. Am. Chem. Soc.*, 2016, **138**, 2138–2141.
483 D. Wu, X. Zhao, Y. Huang, J. Lai, H. Li, J. Yang, C. Tian, P. He, Q. Huang and X. Tang, *Chem. Mater.*, 2021, **33**, 4971–4976.
484 Z. Zhang, Y. Liang, H. Huang, X. Liu, Q. Li, L. Chen and D. Xu, *Angew. Chem., Int. Ed.*, 2019, **58**, 7263–7267.
485 T. Wang, D. Yue, X. Li and Y. Zhao, *Appl. Catal., B*, 2020, **268**, 118399.
486 S. Kumar, I. Hassan, M. Regue, S. Gonzalez-Carrero, E. Rattner, M. A. Isaacs and S. Eslava, *J. Mater. Chem. A*, 2021, **9**, 12179–12187.
487 K. M. Boopathi, P. Karuppuswamy, A. Singh, C. Hanmandlu, L. Lin, S. A. Abbas, C. C. Chang, P. C. Wang, G. Li and C. W. Chu, *J. Mater. Chem. A*, 2017, **5**, 20843–20850.
488 Z. Zhang, Y. Yang, Y. Wang, L. Yang, Q. Li, L. Chen and D. Xu, *Angew. Chem., Int. Ed.*, 2020, **59**, 2005495.
489 Y. Hai, W. Huang, Z. Li, D. Wu, Q. Huang and X. Tang, *ACS Appl. Energy Mater.*, 2021, **4**, 5913–5917.
490 G. Chen, P. Wang, Y. Wu, Q. Zhang, Q. Wu, Z. Wang, Z. Zheng, Y. Liu, Y. Dai and B. Huang, *Adv. Mater.*, 2020, **32**, 2001344.
491 C. Pan, T. Takata, M. Nakabayashi, T. Matsumoto, N. Shibata, Y. Ikuhara and K. Domen, *Angew. Chem., Int. Ed.*, 2015, **54**, 2955–2959.
492 I. E. Castelli, D. D. Landis, K. S. Thygesen, S. Dahl, I. Chorkendorff, T. F. Jaramillo and K. W. Jacobsen, *Energy Environ. Sci.*, 2012, **5**, 9034–9043.
493 R. Abe, M. Higashi and K. Domen, *J. Am. Chem. Soc.*, 2010, **132**, 11828–11829.
494 M. Higashi, K. Domen and R. Abe, *J. Am. Chem. Soc.*, 2012, **134**, 6968–6971.
495 H. Fujito, H. Kunioku, D. Kato, H. Suzuki, M. Higashi, H. Kageyama and R. Abe, *J. Am. Chem. Soc.*, 2016, **138**, 2082–2085.
496 H. Kunioku, M. Higashi, O. Tomita, M. Yabuuchi, D. Kato, H. Fujito, H. Kageyama and R. Abe, *J. Mater. Chem. A*, 2018, **6**, 3100–3107.
497 H. Kunioku, A. Nakada, M. Higashi, O. Tomita, H. Kageyama and R. Abe, *Sustainable Energy Fuels*, 2018, **2**, 1474–1480.
498 A. Walsh, D. J. Payne, R. G. Egdell and G. W. Watson, *Chem. Soc. Rev.*, 2011, **40**, 4455–4463.
499 D. Kato, K. Hongo, R. Maezono, M. Higashi, H. Kunioku, M. Yabuuchi, H. Suzuki, H. Okajima, C. Zhong, K. Nakano, R. Abe and H. Kageyama, *J. Am. Chem. Soc.*, 2017, **139**, 18725–18731.
500 H. Kunioku, M. Higashi, C. Tassel, D. Kato, O. Tomita, H. Kageyama and R. Abe, *Chem. Lett.*, 2017, 583–586.
501 A. Nakada, A. Saeki, M. Higashi, H. Kageyama and R. Abe, *J. Mater. Chem. A*, 2018, **6**, 10909–10917.
502 A. Nakada, M. Higashi, T. Kimura, H. Suzuki, D. Kato, H. Okajima, T. Yamamoto, A. Saeki, H. Kageyama and R. Abe, *Chem. Mater.*, 2019, **31**, 3419–3429.
503 D. Ozaki, H. Suzuki, A. Nakada, M. Higashi, O. Tomita, H. Kageyama and R. Abe, *Chem. Lett.*, 2020, 978–981.
504 T. N. Ye, M. Xu, W. Fu, Y. Y. Cai, X. Wei, K. X. Wang, Y. N. Zhao, X. H. Li and J. S. Chen, *Chem. Commun.*, 2014, **50**, 3021–3023.
505 T. Kanagaraj and S. Thiripuranthagan, *Appl. Catal., B*, 2017, **207**, 218–232.

 This journal is © The Royal Society of Chemistry 2021

506 A. K. Singh, J. H. Montoya, J. M. Gregoire and K. A. Persson, *Nat. Commun.*, 2019, **10**, 443.
507 H. Masood, C. Y. Toe, W. Y. Teoh, V. Sethu and R. Amal, *ACS Catal.*, 2019, **9**, 11774–11787.
508 T. Toyao, Z. Maeno, S. Takakusagi, T. Kamachi, I. Takigawa and K.-I. Shimizu, *ACS Catal.*, 2020, **10**, 2260–2297.
509 M. Krallinger, O. Rabal, A. Lourenco, J. Oyarzabal and A. Valencia, *Chem. Rev.*, 2017, **117**, 7673–7761.
510 V. Tshitoyan, J. Dagdelen, L. Weston, A. Dunn, Z. Q. Rong, O. Kononova, K. A. Persson, G. Ceder and A. Jain, *Nature*, 2019, **571**, 95–98.
511 K. T. Butler, D. W. Davies, H. Cartwright, O. Isayev and A. Walsh, *Nature*, 2018, **559**, 547–555.
512 Y. Bai, L. Wilbraham, B. J. Slater, M. A. Zwijnenburg, R. S. Sprick and A. I. Cooper, *J. Am. Chem. Soc.*, 2019, **141**, 9063–9071.
513 E. Can and R. Yildirim, *Appl. Catal., B*, 2019, **242**, 267–283.
514 H. Mai, T. C. Le, T. Hisatomi, D. Chen, K. Domen, D. A. Winkler and R. A. Caruso, *iScience*, 2021, **24**, 103068.
515 D. M. Herlihy, M. M. Waegele, X. H. Chen, C. D. Pemmaraju, D. Prendergast and T. Cuk, *Nat. Chem.*, 2016, **8**, 556.
516 K. A. Lehuta and K. R. Kittilstved, *Dalton Trans.*, 2016, **45**, 10034–10041.
517 H. X. Mai, T. Lu, Q. Li, Z. F. Liu, Y. X. Li, F. Kremer, L. Li, R. L. Withers, H. D. Wen and Y. Liu, *ACS Appl. Mater. Interfaces*, 2018, **10**, 12781–12789.

This journal is © The Royal Society of Chemistry 2021